Università degli Studi di Napoli " Federico II"
Facoltà di Scienza Matematiche Fisiche e Naturali

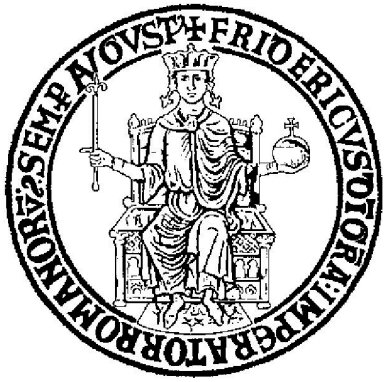

SEARCH FOR $\nu_\mu \rightarrow \nu_\tau$ OSCILLATIONS IN THE OPERA EXPERIMENT

ANTONIA DI CRESCENZO

Ph.D. in Physics
Dottorato di Ricerca in Fisica Fondamentale ed Applicata
XXV Ciclo

Tutors:
Prof. Paolo Strolin
Prof. Giovanni De Lellis

Coordinator:
Prof. Raffaele Velotta

ABSTRACT

The OPERA neutrino experiment in the underground Gran Sasso Laboratory (LNGS) was designed to perform the first detection of neutrino oscillations in the $\nu_\mu \rightarrow \nu_\tau$ channel in appearance mode. The ν_τ signature is provided by the direct observation of the τ lepton produced in ν_τ interaction and decaying with a flight length of few hundred microns. The detection of both the τ production and decay vertices is achieved thanks to the micrometric accuracy of nuclear emulsions . The apparatus is hybrid: it consists of a 1.25 kton emulsion/lead target complemented by electronic detectors. The detector is placed in the high energy long-baseline CERN to LNGS neutrino beam (CNGS), 730 km away from the neutrino source.

Three candidates have been observed in the current analysed statistics, satisfying the kinematical selection criteria. Their topology and kinematics has been fully studied and described here in detail.

The efficiency of the ν_τ event selection has been evaluated for the different τ decay channels. The background yield has been evaluated and the kinematical selection optimized in order to have a better discrimination.

The statistical significance of the $\nu_\mu \rightarrow \nu_\tau$ observation is 3.5σ.

CONTENTS

INTRODUCTION

Neutrino oscillations were first introduced in 1957 by B. Pontecorvo. This phenomenon occurs if neutrinos have non-degenerate masses and if mass and flavor eigenstates do not coincide. In the last 30 years some unexpected experimental observations of the solar and atmospheric neutrinos were interpreted as hints in favour of neutrino oscillation. There is now a clear evidence of neutrino oscillations: experimental proofs come from systematic studies of solar and atmospheric neutrinos and also from studies on neutrinos produced by accelerators and reactors.
Despite the neutrino $\nu_\mu \rightarrow \nu_\tau$ oscillations in the atmospheric sector are well established, the direct evidence of the ν_τ appearance is still missing. It requires a detector capable of identifying the short-lived τ lepton produced in ν_τ Charged Current interactions.
The OPERA (Oscillation Project with Emulsion-tRacking Apparatus) detector in Gran Sasso National Laboratory (LNGS) is designed to accomplish this task, aiming at the detection of ν_τ in an almost pure ν_μ beam (CNGS, Cern Neutrino beam to Gran Sasso) produced at CERN SPS, 730 km far from the detector. The experiment has taken data for five years, from 2008 to 2012, collecting more than 15000 neutrino interactions.
The OPERA detector uses nuclear emulsions as a high resolution tracking device to search for neutrino interactions. The target has a modular structure. It is made of a sequence of walls of elementary units, called *bricks*, and planes of electronic detectors. Each brick is made of a sandwich of lead plates and emulsion films according to the so called Emulsion Cloud Chamber technique (ECC). The usage of lead allows to get a high mass in a relatively compact detector (1.25 kton with 150000 bricks), thus increasing the neutrino interaction probability. The emulsions, with a micrometric spatial resolution, are used for a high precision reconstruction of tracks of particles produced in neutrino interactions.

Significant part of the work was devoted to the event analysis, including a trough study of the three ν_τ candidates. Their topology was defined from the emulsion data and the kinematical analysis was performed in order to asses τ hypothesis.
In this thesis a full revision of the efficiencies was performed for the different τ decay channels. All the steps of the analysis chain of a neu-

trino event in the OPERA detector have been simulated and the corresponding efficiencies evaluated: from the electron detector trigger to the event location inside the brick and the search for τ decays. The kinematical selection has also been studied and optimized, aiming to a better discrimination of signal and background.
A detailed analysis of all the background sources was performed. It mainly consists of three components: the decay of charmed hadrons, the hadrons interaction without visible signs of the nucleus recoil in emulsion and the muon scattering. To enhance the sensitivity to the τ detection, more background reduction criteria were studied and precise measurements in emulsions were performed.
Combining the efficiencies and the background evaluation, the number of expected events with the current statistics was estimated. The background expectation, together with the observed candidates, allowed to calculate the significance of the $\nu_\mu \to \nu_\tau$ observation.

Chapter 1 contains a short summary of neutrino oscillations and a review of recent experimental results. An overview of the OPERA experiment is also given.
In Chapter 2 the location procedure of a neutrino interaction in the OPERA detector is described, together with the simulation chain used to evaluate the detection efficiencies. The kinematical selection applied to the different decay channels is also presented.
Chapter 3 describes the analysis of the observed ν_τ candidates. The description of their decay topologies and the kinematical analysis is reported.
In Chapter 4 signal and background expectations are reported and the significance of the observation is presented.

1 NEUTRINO OSCILLATIONS AND THE OPERA EXPERIMENT

1.1 INTRODUCTION

The study of neutrinos began in 1930 when Wolfgang Pauli postulated the existence of a neutral particle with a very small mass in order to explain the continuous electron energy spectrum found in β decays [1]. Since then, the field has been driven by vast theoretical literature and exciting experimental results. The neutrino has been the target of experimental studies for approximately 60 years and new results are still being released and future experiments are in their early design phases. Current and future experiments have taken neutrino physics beyond the discovery stage and into the era of precision measurements.

Neutrinos are electrically-neutral spin-1/2 leptons which only undergo weak interactions. In the standard model (SM) of particle physics, neutrinos are massless and come in three flavors, electron (ν_e), muon (ν_μ) and tau (ν_τ), analogous to the charged leptons. They are also experimentally known to exist only as left-handed neutrinos or right-handed antineutrinos [2].

Though existing copiously throughout the universe, they are experimentally very difficult to detect as they can pass through tremendous amounts of matter without interacting. Soon after their initial theoretical proposal by Pauli in 1930, Fermi generated a point-like theory for neutrino interactions [3]. The currently verified unified electroweak theory which describes neutrino interactions would have not been fully developed until the 1960s [4, 5, 6] and the weak interaction mediating bosons, the $W^{\pm}$ and Z^0 were eventually discovered in 1983 [7]. The large masses of these vector bosons (M_W = 80.6 GeV/c^2, M_Z = 91.2 GeV/c^2) result in a weak interaction range of only about 10^{-18} m. The neutrino itself was first definitively detected in 1956 by Cowan and Reines using the inverse β decay reaction $\overline{\nu} + p \rightarrow e^+ + n$ taking place in a liquid scintillator surrounded by photomultiplier tubes

[8]. The source of the electron antineutrinos in this experiment was a nearby nuclear reactor facility.
Since then neutrinos have been detected from natural sources such as the Sun [9], cosmic rays and the Earth's atmosphere [10], the core of the Earth [11], man-made accelerator beamlines [12] and a Supernova event in 1987 [13]. In addition to electron flavor neutrinos, muon [14] and tau flavor neutrinos [15] have also been detected, and experiments studying weak boson decays (in particular, the Z^0 boson which mediates NC weak interactions) currently limit the number of light species which participate in weak interactions to these three [16].

1.2 NEUTRINO OSCILLATIONS AND THEIR FORMALISM

Neutrinos are massless in the Standard Model (SM). Experimentally, all direct measurements of the neutrino mass have produced so far only upper limits. The absolute mass of the electron neutrino can be measured by observing β decays. The best limit on electron neutrino mass, obtained by measuring the end-point of the electron spectrum in Tritium decay, is [17]

$$m_{\nu_e} < 2.3\ eV\ (95\%\text{C.L.}) \tag{1}$$

The mass of the muon neutrino can be determined from momentum analysis of pion decay $\pi^+ \to \mu^+\nu_\mu$. The mass of tau neutrino is derived by fitting the visible energy vs invariant mass in tau decays $\tau^- \to 3\pi^- + 2\pi^+ + \nu_\tau(+\pi^0)$. The upper limit on the mass of ν_μ [18] and ν_τ [19] are

$$m_{\nu_\mu} < 0.17\ MeV\ (90\%\text{C.L.}) \tag{2}$$
$$m_{\nu_\tau} < 18.2\ MeV\ (95\%\text{C.L.}) \tag{3}$$

Massive neutrinos play an important role in the evolution of the universe and consequently constraints on absolute neutrino masses can be derived from cosmology. The latest analysis [20] of WMAP and SDSS data yields the limit on the sum of neutrino masses:

$$\sum m_\nu < 0.44\ eV\ (95\%\text{C.L.}). \tag{4}$$

However, compelling evidences for massive neutrinos have been found via flavor transformations (*oscillations*) in neutrinos produced from the Sun [21], hadronic decays in the atmosphere [22], accelerator beamlines [23] and nuclear reactors [24, 25, 26].

Neutrinos being massive means that there exists a spectrum of neutrino mass eigenstates ν_i, each with mass $m_i(i = 1,2,3)$. The flavor eigenstates $\nu_\alpha(\alpha = e, \mu, \tau)$ do not necessarily coincide with the mass eigenstates and can be possibly expressed as a superposition of them

$$|\,\nu_\alpha\rangle = \sum_{i=1}^{3} U_{\alpha i}\,|\,\nu_i\rangle. \tag{5}$$

The transformation can be fully written out in terms of a unitary matrix transforming the two sets of eigenstates into each other. It has the general form

$$\begin{pmatrix} \nu_e \\ \nu_\mu \\ \nu_\tau \end{pmatrix} = \begin{pmatrix} U_{e1} & U_{e2} & U_{e3} \\ U_{\mu 1} & U_{\mu 2} & U_{\mu 3} \\ U_{\tau 1} & U_{\tau 2} & U_{\tau 3} \end{pmatrix} \begin{pmatrix} \nu_1 \\ \nu_2 \\ \nu_3 \end{pmatrix} \tag{6}$$

It then takes the form

$$\begin{pmatrix} \nu_e \\ \nu_\mu \\ \nu_\tau \end{pmatrix} = \begin{pmatrix} 1 & 0 & 0 \\ 0 & \cos\theta_{23} & \sin\theta_{23} \\ 0 & -\sin\theta_{23} & \cos\theta_{23} \end{pmatrix} \tag{7}$$

$$\times \begin{pmatrix} \cos\theta_{13} & 0 & \sin\theta_{13}e^{-i\delta} \\ 0 & 1 & 0 \\ -\sin\theta_{13}e^{-i\delta} & 0 & \cos\theta_{13} \end{pmatrix}$$

$$\times \begin{pmatrix} \cos\theta_{12} & \sin\theta_{12} & 0 \\ -\sin\theta_{12} & \cos\theta_{12} & 0 \\ 0 & 0 & 1 \end{pmatrix} \begin{pmatrix} \nu_1 \\ \nu_2 \\ \nu_3 \end{pmatrix} \tag{8}$$

where the so-called mixing angles θ_{12}, θ_{13}, θ_{23} and the CP-violating phase δ are the four parameters of the matrix which can be experimentally constrained. The separation of the sub-matrices roughly represent different areas of experimental research in neutrino oscillations. In particular, atmospheric and long baseline accelerator experiments have measured θ_{23}, reactor and accelerator experiments have recently measured θ_{13}, and solar experiments have measured θ_{12}. There has been no measurement of δ yet.

The experiments involve transformations of one neutrino flavor, ν_α, into another, ν_β, after propagation along a baseline L. It is useful to express this mathematically via the oscillation probability $P(\nu_\alpha \to \nu_\beta)$. If $\alpha = \beta$ the oscillation probability becomes a survival probability.

The massive neutrino states ν_i are eigenstates of the free Hamiltonian and the time evolution is simply

$$|\,\nu_i(t)\rangle = e^{-iE_i t}\,|\,\nu_i\rangle. \tag{9}$$

From Equation (5), the time evolution of the flavor state ν_α is then

$$|\,\nu_\alpha(t)\rangle = \sum_i U^*_{\alpha i} e^{-iE_i t}\,|\,\nu_i\rangle. \tag{10}$$

The amplitude of finding the neutrino at the time t in a flavor state ν_β is

$$\begin{aligned} A_{\nu_\alpha\to\nu_\beta}(t) = \langle\nu_\beta\,|\,\nu_\alpha(t)\rangle &= \sum_i U^*_{\alpha i} e^{-iE_i t}\langle\nu_\beta\,|\,\nu_i\rangle \\ &= \sum_i\sum_j U^*_{\alpha i} U_{\beta j} e^{-iE_i t}\langle\nu_j\,|\,\nu_i\rangle \\ &= \sum_i U^*_{\alpha i} U_{\beta i} e^{-iE_i t}. \end{aligned} \tag{11}$$

The transition probability is given by

$$\begin{aligned} P_{\nu_\alpha\to\nu_\beta}(t) &= |\,A_{\nu_\alpha\to\nu_\beta}(t)\,|^2 \\ &= \sum_i\sum_j U^*_{\alpha i} U_{\beta i} U_{\alpha j} U^*_{\beta j} e^{-i(E_i-E_j)t}. \end{aligned} \tag{12}$$

For relativistic neutrinos,

$$E_i = \sqrt{p^2 + m_i^2} \simeq p + m_i^2/2p \simeq p + m_i^2/2E. \tag{13}$$

Thus, the transition probability can be approximated by

$$P_{\nu_\alpha\to\nu_\beta}(t) = \sum_i\sum_j U^*_{\alpha i} U_{\beta i} U_{\alpha j} U^*_{\beta j} e^{-i\frac{\Delta m^2_{ij}}{2E}t}, \tag{14}$$

where $\Delta m^2_{ij} = m^2_i - m^2_j$. In neutrino oscillation experiments, the measured quantity is usually the distance L travelled by neutrinos instead of the time t. For relativistic neutrinos, $t \simeq L$ (in units where $\hbar = c = 1$) and one finds

$$\begin{aligned} P_{\nu_\alpha\to\nu_\beta}(t) &= \sum_i\sum_j U^*_{\alpha i} U_{\beta i} U_{\alpha j} U^*_{\beta j} e^{-i\frac{\Delta m^2_{ij}}{2E}L} \\ &= \delta_{\alpha\beta} - 4\sum_{i>j} \mathrm{Re}(U^*_{\alpha i} U_{\beta i} U_{\alpha j} U^*_{\beta j}) \sin^2\left(\frac{\Delta m^2_{ij}}{2E}L\right) \\ &\quad + 2\,\mathrm{Im}(U^*_{\alpha i} U_{\beta i} U_{\alpha j} U^*_{\beta j}) \sin\left(\frac{\Delta m^2_{ij}}{2E}L\right). \end{aligned} \tag{15}$$

To simplify the discussion, we shall consider a special case of two flavor oscillation $\nu_\mu \to \nu_\tau$. The two-neutrino description is an adequate approximation in treating data from a number of neutrino oscillation experiments, e.g. when the L/E value is such that one Δm^2

value dominates. In this case, there is only one squared-mass difference $\Delta m^2 = m_2^2 - m_1^2$ and the mixing matrix U takes the form

$$U = \begin{pmatrix} \cos\theta & \sin\theta \\ -\sin\theta & \cos\theta \end{pmatrix} \tag{16}$$

From Equation(15), it follows that the transition probability of $\nu_\mu \to \nu_\tau$ is simply

$$\begin{aligned} P_{\nu_\mu \to \nu_\tau} &= \sin^2 2\theta \ \sin^2\left(\frac{\Delta m^2 L}{4E}\right) \\ &= \sin^2 2\theta \ \sin^2\left(1.27\frac{\Delta m^2(eV^2)L(m)}{E(MeV)}\right) \end{aligned} \tag{17}$$

It is clear from Equation (17) that the neutrino oscillation can take place only if both the mass splitting Δm^2 and the mixing angle θ are nonzero. Indeed, it is the observation of neutrino oscillations that leads to the conclusion that neutrinos are massive and they mix, i.e. mass eigenstates are not identical to flavor eigenstates.

1.3 NEUTRINO OSCILLATION EXPERIMENTS

The experimental observations of neutrino oscillations can be divided in two groups, according to the measured parameters:

- experiments on solar and nuclear reactor neutrinos, measuring Δm^2_{12} and θ_{12}
- experiments on atmospheric and accelerator neutrinos, measuring Δm^2_{23} and θ_{23}
- experiments measuring θ_{13}.

1.3.1 Solar and reactor neutrino experiments

The first hint for flavor change came with the observation of an anomaly in the solar electron neutrino flux. In 1970, the Homestake [28] experiment observed a deficit of electron neutrinos from predictions made by the standard solar model (SSM). This anomaly was later confirmed by the SAGE [29] and GALLEX [30] experiments.
In 2002 the Sudbury Neutrino Observatory was the first experiment to show direct evidence for neutrino flavor transformation [31]. Using the charged current (CC) reaction $\nu_e + d \to p + p + e^-$, they confirmed the electron neutrino solar flux deficit for ^8B neutrinos. Simultaneously, using the neutral current (NC) reaction $\nu_x + d \to p + n + \nu_x$

which is equally sensitive to all active neutrino flavors (ν_e, ν_μ, ν_τ), they showed conservation of the total ^{8}B solar neutrino flux in agreement with the SSM prediction, thus showing that some electron neutrinos had changed to one of the other two flavors.
The results from SNO's CC, NC and elastic scattering (ES) measurements together with the Super-Kamiokande data are shown in Figures 1 and 2. In combination with the reactor ($\overline{\nu}_e$) data from KamLAND, the so-called large mixing angle (LMA) solution is preferred with a confidence level of more than 5σ [32, 33].

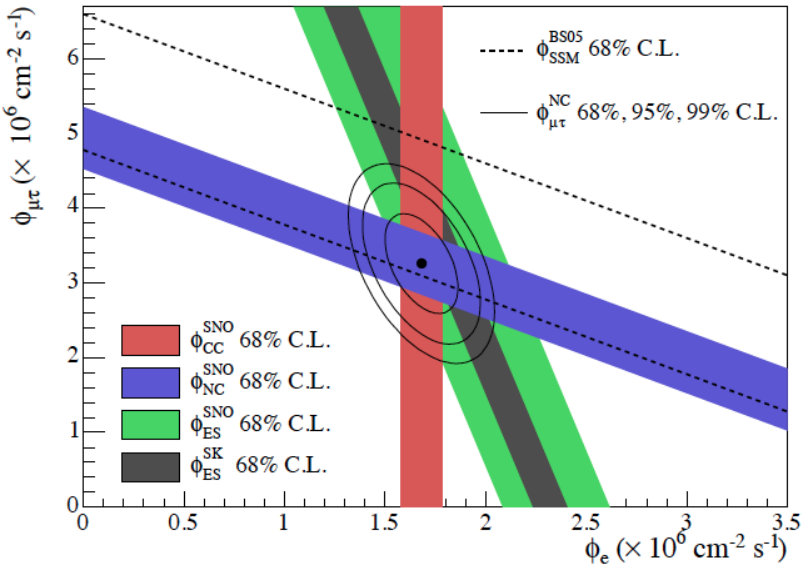

Figure 1: Combined results from SNO and Super-Kamiokande ^{8}B neutrino flux measurements for the different interaction channels (coloured bands) and the expectation from the standard solar model (SSM) for the total flux (dashed contour lines), shown as the flux of ν_μ and ν_τ vs. the flux of ν_e. The allowed region from all measurements (solid lines) clearly indicates a non-zero flux of ν_μ and ν_τ and therefore provides a strong evidence for neutrino oscillations. [32, 33]

The KamLAND reactor experiment demonstrated that this flavor change was the consequence of neutrino oscillation by observing distortion of reactor $\overline{\nu}_e$ energy spectrum [34] as a function of the distance from the reactor. Figure 3 plots the ratio between the background-subtracted $\overline{\nu}_e$ candidate events, including the subtraction of geoneutrinos, and the expectation in absence of oscillations [35].

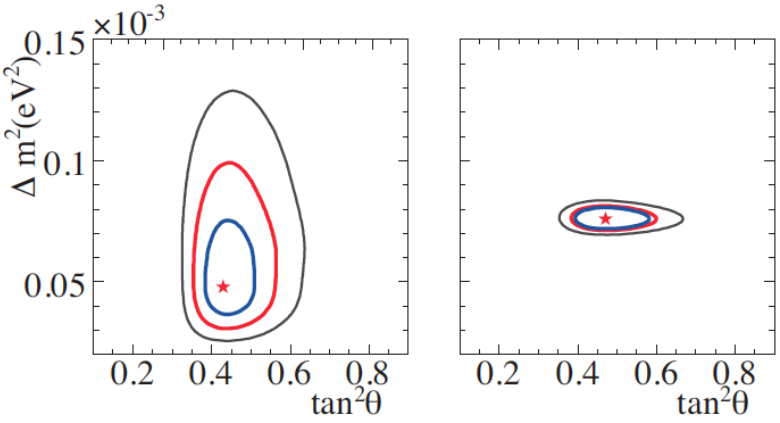

Figure 2: Allowed parameter region from global solar data without (left) and with (right) KamLAND, at 68%, 95%, and 99% CL as well as the best fit (star). [35]

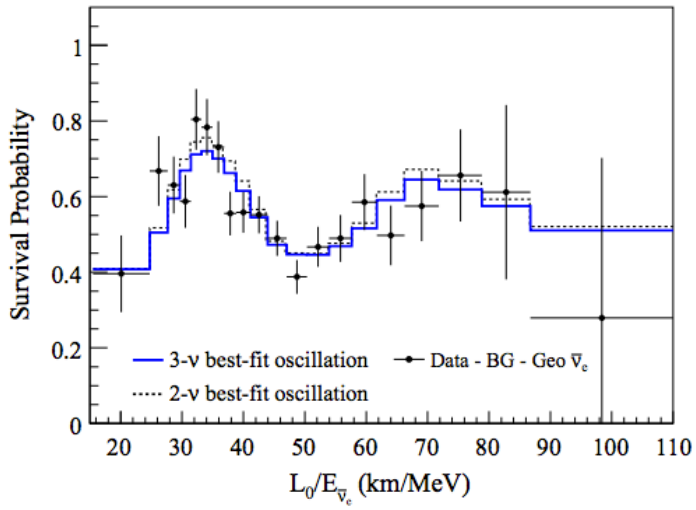

Figure 3: Ratio of the background and geoneutrino-subtracted $\overline{\nu}_e$ spectrum to the expectation for no-oscillation as a function of L_0/E. L_0 is the effective baseline taken as a flux-weighted average (L_0 = 180 km) [35]. This shows the evidence for oscillations.

1.3.2 Atmospheric and accelerator neutrino experiments

Similarly, atmospheric neutrinos, produced as decay products in hadronic showers resulting from collisions of cosmic rays with nuclei in the upper atmosphere, were studied by the Super-Kamiokande water Cherenkov detector [36], MACRO [37] and SOUDAN2 [38]. Super-Kamiokande was the first to report the evidence for oscillations through a zenith angle dependent deficit of muon neutrinos (Figure 4). Long baseline terrestrial neutrino experiments K2K [39] and MINOS [40] observed ν_μ disappearance consistent with the Super-K results. Figure 5 presents 68% and 90% contours for the MINOS oscillation fit and 90% contours for the Super-K experiment.

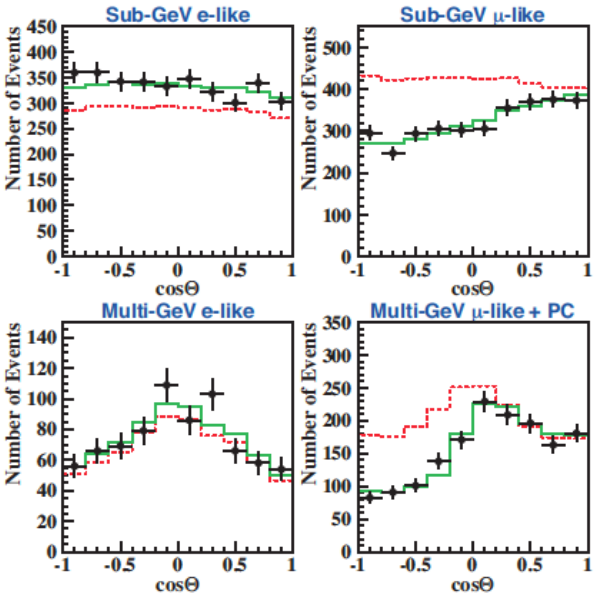

Figure 4: Zenith angle distribution of fully contained 1-ring e-like and μ-like events with visible energy below or above 1.33 GeV, corresponding to the Sub-GeV and Multi-GeV samples in the Super-Kamiokande detector. Multi-GeV μ-like events distribution partially include also contained events. The dashed curves show non-oscillated expected flux and solid curves show the best fit for $\nu_\mu \to \nu_\tau$ oscillation.

1.3.3 Search for θ_{13}

For a long period, an upper limit for the value of θ_{13} was only available. Until recently the best upper limit had been measured by the

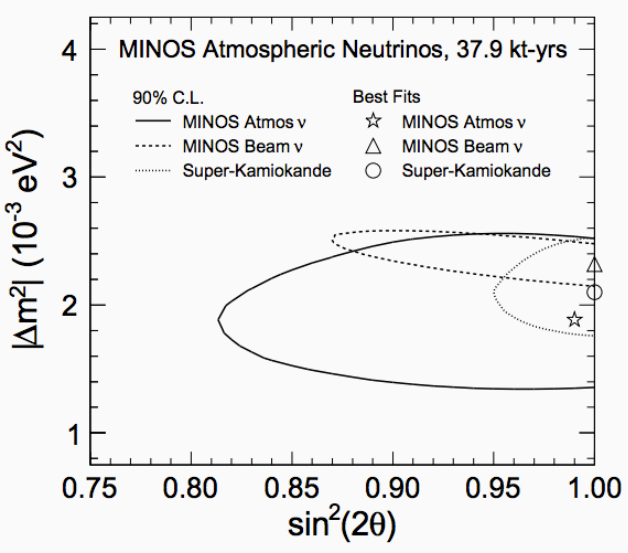

Figure 5: Allowed region of the (θ_{23}-Δm^2_{23}) parameter space as published by the MINOS collaboration in 2011. Results from Super-Kamiokande are also included. [49]

CHOOZ experiment [41], in which $\overline{\nu}_e$ produced at a nuclear power plant were measured at a detector situated at roughly 1km far from the nuclear reactors.

The new generation of experiments built to measure θ_{13} are usually divided in two categories. The first one intends to measure disappearance of $\overline{\nu}_e$ from the $\overline{\nu}_e$ produced in reactors, such as Double-CHOOZ [42], RENO [43] and Daya Bay [44]. The second one intends to measure the appearance of ν_e from a ν_μ beam produced in an accelerator complex, such as T2K [45] and Nova [46].

In 2011, T2K was the first experiment to directly measure a non-zero value of θ_{13}[48]. The precision on this value has then strengthened by subsequent results from MINOS [50] and Double-CHOOZ [51], culminating in the recent announcement of a 5.2 σ and 4.9 σ by Daya Bay [52] and RENO [53] respectively. Thanks to these experiments the value of θ_{13} is now known at the same level of precision as the other mixing angles.

The latest results from the different experiments are shown in Figure 6.

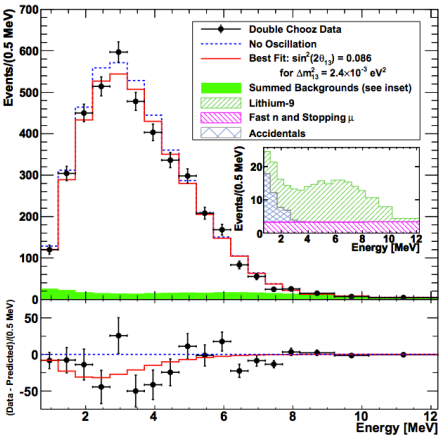

(a) Double-CHOOZ [51]

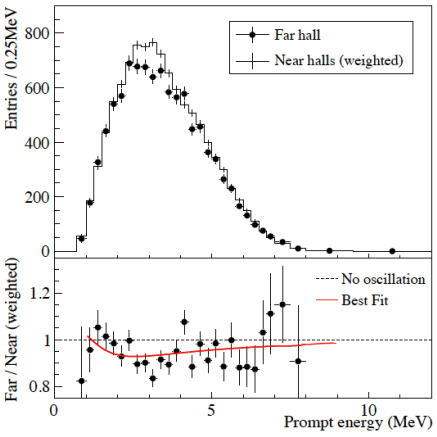

(b) Daya Bay [52]

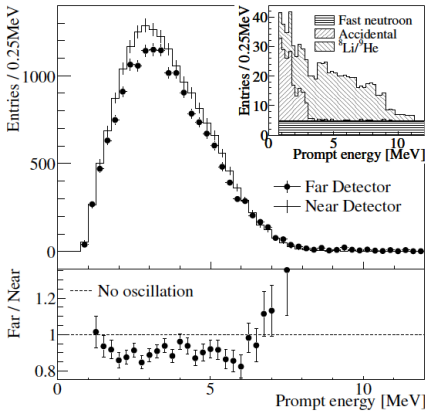

(c) RENO [53]

Figure 6: Results from three experiments measuring θ_{13}.Top: measured prompt energy spectrum of the far detector compared with the no-oscillation prediction from the measurements of the two near detectors. Spectra were background subtracted in (a) and (b), while include background for (c). Bottom: the ratio of the measured spectrum of far detector to the no-oscillation prediction.

1.3.4 Summary of neutrino oscillation parameters

Neutrino oscillation experiments are measuring the squared mass differences (Δm^2_{12} and Δm^2_{23}) instead of the absolute mass, therefore the mass ordering is not yet known. Figure 7 shows the conceptual diagram for the two orderings. With $m_3 \gg m_2 > m_1$, it is defined as normal hierarchy, while with $m_3 \ll m_1 < m_2$, it is defined as inverted hierarchy.

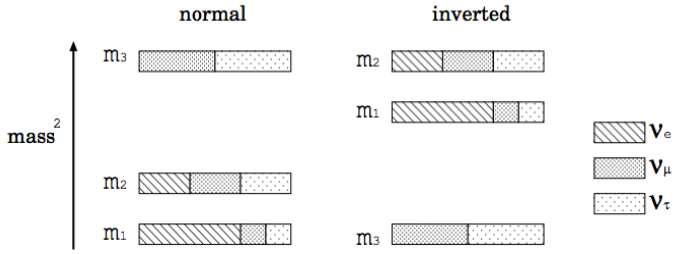

Figure 7: Three-neutrino mass-squared spectrum, for the two mass hierarchies.

The global best fit results of neutrino oscillation parameters are summarized in Table 1, for normal hierarchy (NH) and inverted hierarchy (IH).

Parameter	**Hierarchy**	**Best fit**	**1σ range**
Δm^2_{12} ($\times 10^{-5}$ eV^2)	NH or IH	7.54	7.32 - 7.80
$\sin^2\theta_{12}(10^{-1})$	NH or IH	3.06	2.91 - 3.25
$\lvert\Delta m^2_{13}\rvert$ ($\times 10^{-3}$ eV^2)	NH	2.43	2.33 - 2.49
$\lvert\Delta m^2_{13}\rvert$ ($\times 10^{-3}$ eV^2)	IH	2.42	2.31 - 2.49
$\sin^2\theta_{13}(10^{-2})$	NH	2.41	2.16 - 2.66
$\sin^2\theta_{13}(10^{-2})$	IH	2.44	2.19 - 2.67
$\sin^2\theta_{23}(10^{-1})$	NH	3.86	3.65 - 4.10
$\sin^2\theta_{23}(10^{-2})$	IH	3.92	3.70 - 4.31

Table 1: Summary of global best fit of neutrino oscillation parameters, taken from [54]

1.4 THE OPERA EXPERIMENT

As discussed in the previous section, the disappearance of atmospheric ν_μ is now well established. The direct and unambiguous detection of its oscillation in a different neutrino flavor is, however, still an important missing tile in the oscillation scenario.
The OPERA (Oscillation Project with Emulsion-tRacking Apparatus) experiment [55, 56] at Gran Sasso Laboratory (LNGS) was designed to accomplish this task. Its aim is to perform the first direct detection of neutrino oscillations in appearance mode through the study of $\nu_\mu \rightarrow \nu_\tau$ oscillations.
The direct appearance search is based on the detection of τ leptons produced in the charged current interactions (CC) of ν_τ. The neutrino beam is an almost pure ν_μ beam produced by the protons accelerated in the CERN SPS and injected in the CNGS beam line, 730 km away from the detector location. The OPERA experiment [57, 58] is installed in Hall C of the underground Gran Sasso Laboratory (LNGS), aligned with the CNGS baseline, under 1400 meters of rock.
The detector concept is based on the Emulsion Cloud Chamber (ECC) technique, combined with real-time detection techniques (electronic detectors): OPERA is a hybrid apparatus with a modular structure. The ECC basic unit in OPERA is a brick made of 56 lead plates (absorbers), providing the necessary mass, interleaved with 57 nuclear emulsion films, providing the necessary spatial and angular resolution. The electronic detectors are used to trigger the neutrino interactions, to locate the brick in which the interaction took place, to identify muons and measure their momentum and charge. The analysis of the emulsion is performed in the OPERA emulsion scanning laboratories all over the world by automatic scanning systems developed to measure the large amount of emulsions involved in the analysis.

1.4.1 The CNGS beam

The CNGS neutrino beam [59] was designed and optimized for the study of $\nu_\mu \rightarrow \nu_\tau$ oscillations in appearance mode. It is produced by a 400 GeV/c proton beam extracted from the CERN SPS accelerator; during a nominal CNGS cycle there are two SPS extractions (10.5 μs each, separated by 50 ms) of $\sim 2.0 \times 10^{13}$ protons. Each CNGS cycle in the SPS is 6 s long.
The proton beam is transported through the transfer line TT41 to the CNGS target T40. The target consists of a series of thin graphite rods. Secondary pions and kaons of positive charge produced in the target are focused into a parallel beam by a system of two magnetic lenses,

called horn and reflector (Fig. 8).

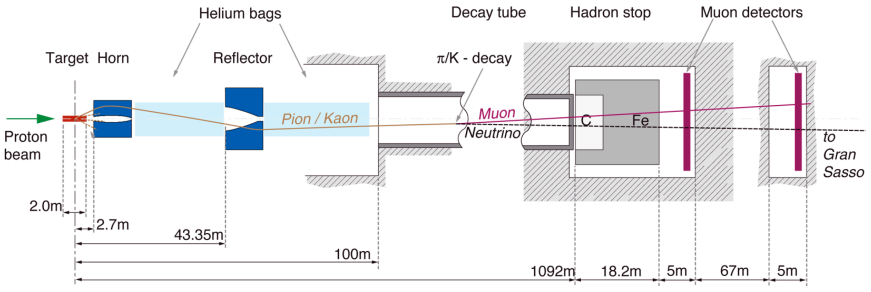

Figure 8: Main components of the CNGS beam line.

A 1000 m long decay-pipe allows most of the pions and kaons to decay into muon-neutrinos and muons. The remaining hadrons (protons, pions, kaons, ...) are absorbed in a hadron stopper (a 18 m long block of graphite and iron). The muons are monitored by two sets of detectors downstream of the stopper; they measure the muon intensity, the beam profile and its centre, and they allow the fine tuning of the beam (steering of the proton beam on target, horn and reflector alignment, etc.). Further downstream, the muons are absorbed in the rock, while neutrinos continue to travel towards Gran Sasso.
The average neutrino energy at LNGS is ~17 GeV (Fig. 9); the average L/E_ν ratio is 43 km GeV^{-1}.

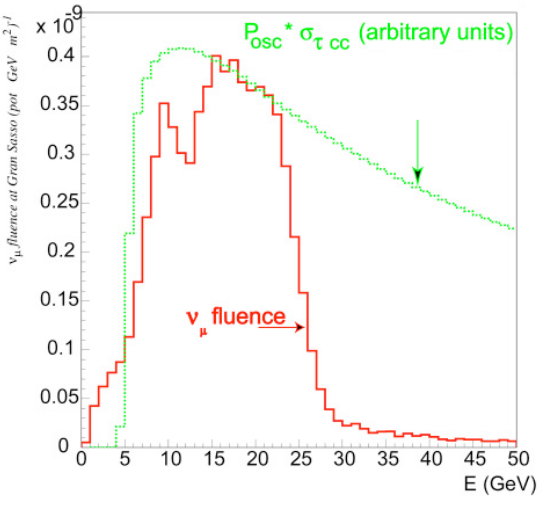

Figure 9: CNGS ν_μ energy spectrum and oscillation probability multiplied by the ν_τ cross section.

The $\overline{\nu}_\mu$ contamination is ~4% (2% as interaction rate, given the $\overline{\nu}_\mu$ cross

section), the ν_e and $\overline{\nu}_e$ contamination is lower than 1%, while the number of prompt ν_τ from D_s production and decay are negligible.
The integrated protons on target collected in all the OPERA run are reported in Table 2.

run	**p.o.t** $\times$ $\mathbf{10^{19}}$
2008	1.74
2009	3.53
2010	4.09
2011	4.75
2012	3.86
Total	17.97

Table 2: Integrated protons on target in the OPERA runs, from 2008 to 2012.

1.4.2 Detector performances

The detector is composed of two identical parts, called supermodules (SM1 and SM2), each consisting of a target section followed by a magnetic spectrometer. In the target, bricks are arranged in 31 vertical planar structures (*walls*), transverse to the beam direction, interleaved with Target Tracker (TT) walls. Each TT wall consists of a double layered plane of long scintillator strips. The TTs trigger the data acquisition and locate the brick in which the interaction occurred. The target section is followed by a magnetic spectrometer, a large dipolar iron magnet instrumented with Resistive Plate Chambers (RPC). The magnetic field intensity is 1.55 T, directed along the vertical axis, transverse to the neutrino beam axis. The RPC planes are inserted between the iron slabs. They provide the tracking inside the magnet and the range measurement for stopping muons. The deflection of charged particles in the magnet is measured by six stations of vertical drift tubes, the Precision Trackers (PT). In order to remove ambiguities in the reconstruction of particle trajectories, each spectrometer is instrumented with additional RPCs with two crossed strip planes tilted with respect to the horizontal and vertical planes, called XPC. Two glass RPC layers (VETO) are placed in front of the detector, acting as a veto for charged particles originating from the upstream material (mainly muons from interactions in the rock or in the Borexino experiment).
The OPERA detector, shown in Fig. 10, has a length of 20 m (z coordi-

nate), is 10 m high (y coordinate) and 10 m wide (x coordinate), for a total weight of about 3 kton.

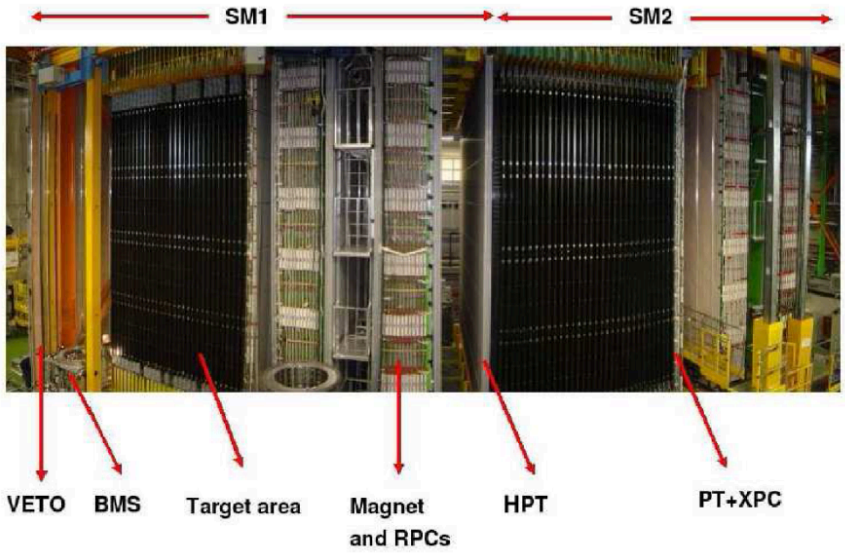

Figure 10: View of the OPERA detector. The upper red horizontal lines indicate the position of the two identical supermodules (SM1 and SM2). Arrows show the position of the target area (ECC brick walls interleaved with planes of plastic scintillators), the VETO planes, the drift tubes (PT) surrounded by the XPC, the magnets and the RPC installed between the magnet iron slabs. The Brick Manipulator System (BMS) is also visible.

Target Tracker

Each brick wall is followed by a Target Tracker (TT) wall [65]. The TT provides real-time detection of the outgoing charged particles, providing the time stamp of neutrino interactions.
Its main task is to locate the brick in which the neutrino interaction took place. It also provides a rough calorimetric measurement of the hadronic shower energy. A TT wall consists of two scintillator planes, one providing the vertical and the other one providing the horizontal coordinates. Each plane is composed by 256 plastic scintillator strips 6.86 m long, thus covering the 6.7 $\times$6.7 m^2 surface defined by the brick wall, with a cross section of 2.63$\times$1.06 cm^2. Along the strip, a 1 mm diameter Wavelength Shifting fiber (WLS) is read on both sides by a multi-anode photomultiplier (PMT), giving a position resolution of $\sim$1 cm (Fig. 11). The strips are grouped in four modules, each module is read out with a 64-channel Hamamatsu PMT; 16 PMTs per TT wall are used.

A signal is measured at each end of the scintillator strips in terms of ADC counts and then converted into energy deposit (in MeV) (see [66] for details). Figure 12 shows the reconstructed energy in the TT for events where a muon track was reconstructed in the electronic detectors.

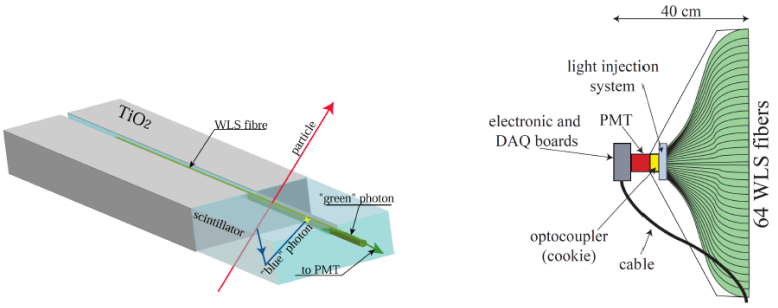

Figure 11: Schematic view of a scintillator strip with the WLS fiber (left) and of a strip module end-cap with the front-end electronics and DAQ board (right).

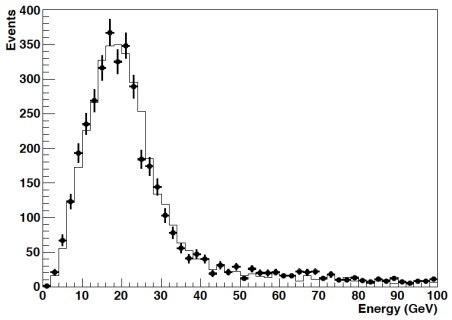

Figure 12: Energy deposit in the TT for events with at least one reconstructed muon. Dots with error bars correspond to data and solid lines to MC.

Spectrometer

Muon spectrometers [67] are conceived to perform muon identification and charge measurement which are needed for the study of the muonic τ-decay channel and for the suppression of the background from the decay of charmed particles, featuring the same topology.
Each muon spectrometer (Fig. 13) consists of a dipolar magnet made of two iron arms for a total weight of 990 ton. The measured magnetic field intensity is 1.55 T. The two arms are interleaved with vertical, 8 m

long drift-tube planes (PT) for the precise measurement of the muon-track bending. Planes of Resistive Plates Chambers (RPCs) are inserted between the iron plates of the arms, providing a coarse tracking inside the magnet, range measurement of the stopping particles and a calorimetric analysis of hadrons.

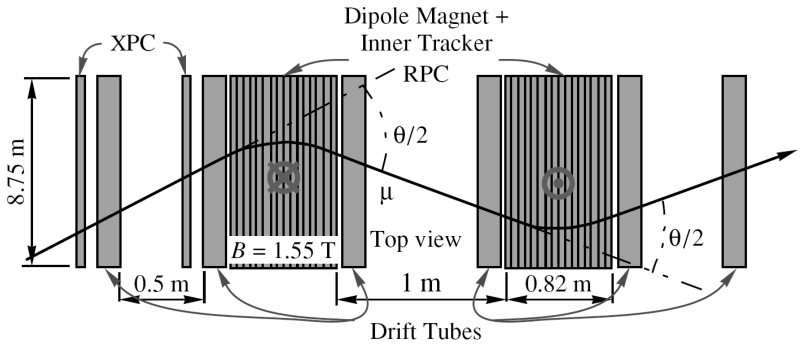

Figure 13: Top view of one muon spectrometer (x-z plane), showing the PT and the dipole magnet instrumented with RPC layers (2×11). The drift tube stations are grouped in 3 pairs per magnet arm.

In order to measure the muon momenta and determine their charge with high accuracy, the Precision Tracker (PT) is made of thin walled aluminum tubes with 38 mm outer diameter and 8 m length [68]. Each of the ~10000 tubes has a central sense wire of 45 μm diameter. They can provide a spatial resolution better than 300 μm. Each spectrometer is equipped with six fourfold layers of tubes.

RPCs [69] identify penetrating muons and measure their charge and momentum in an independent way with respect to the PT. They consist of electrode plates made of 2 mm thick plastic laminate of high resistivity painted with graphite. Induced pulses are collected on two pickup strip planes made of copper strips glued on plastic foils placed on each side of the detector. The number of individual RPCs is 924 for a total detector area of 3080 m^2. The total number of digital channels is about 25000, one for each of the 2.6 cm (vertical) and 3.5 cm (horizontal) wide strips.

In order to solve ambiguities in the track spatial-reconstruction each of the two drift-tube planes of the PT upstream of the dipole magnet is complemented by an RPC plane with two 42.6° crossed strip-layers called XPCs. RPCs and XPCs give a precise timing signal to the PTs.

Figure 14 shows the momentum times charge distribution for data and MC.

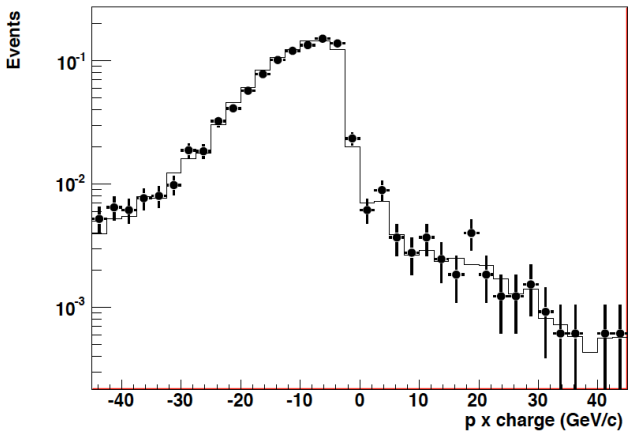

Figure 14: Muon momentum × charge comparison between data (black dots with error bars) and MC (solid line).

Veto

Before reaching the OPERA target, CNGS neutrinos may interact in the rock, in the mechanical structures and in the Borexino detector, producing secondary particles able to induce false triggers. In order to reject these events, a VETO system is placed upstream of the detector. The VETO is made of two planes of glass Resistive Plate Chambers (GRPC) of 9.6×9.2 m^2, each one with 32 GRPC units. Each plane is equipped with horizontal and vertical copper strips with a pitch of 2.5 cm.

Target

The target has a modular structure and it is based on the ECC technique, fulfilling the requirements of high granularity and micrometric resolution, necessary to distinguish the τ decay vertex from the primary ν_τ interaction. The excellent emulsion spatial (~1 μm) and angular (~2 mrad) resolutions are ideal for detection of short-lived particles [60]. The use of passive material, combined with high accuracy tracking devices, allows for momentum measurement of charged particles via multiple Coulomb scattering (MCS), for electromagnetic shower and particle identification [61, 62]. Thus the target unit, the so called *brick*, acts as a standalone detector, that can be selectively removed from the target, developed and analyzed soon after the interaction took place (quasi-online experiment). The brick is made of 57 emulsion films (industrially produced by Fuji) interleaved with 56 lead plates, 1 mm thick. The transverse area is 128 × 102 mm^2, while the longitudinal size is 79 mm, corresponding to 10 X_0, for a total weight

of 8.3 kg. In total, 150000 of such target units were assembled for a total mass of 1.25 kton.

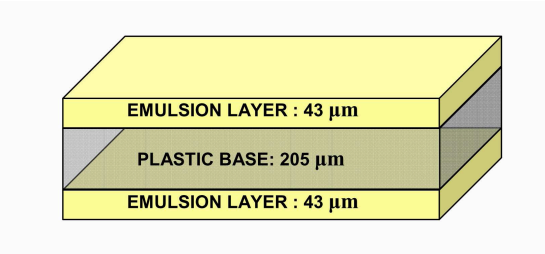

Figure 15: OPERA nuclear emulsion: two emulsion layers coat both sides of a triacetylcellulose transparent base.

Each emulsion film is made of two active layers 43 μm thick poured on a 205 μm plastic base (Fig. 15). The nuclear emulsions consist of AgBr crystals suspended in a gelatin binder. The passage of charged particles creates perturbations at atomic scale (latent image), amplified by a chemical-physical process called development. The resulting grains of silver atoms of about 0.6 μm diameter are visible with an optical microscope. About 30 grains every 100 μm are left by a minimum ionizing particle. The lead contains a low percentage of Calcium (~0.03%) to improve mechanical characteristics, without increasing surface radioactivity [63].
The brick is selected by the electronic on-line detectors, with an accuracy at the cm level. To validate the brick identification result and to facilitate the search for event tracks in the brick with higher accuracy, two interface emulsion films called Changeable Sheets (CS) are attached downstream of the brick in a separate plastic box [64] (Fig. 16). The CS doublet acts as a confirmation of the trigger provided by the Target Tracker. The brick is developed only if the prediction is confirmed, otherwise the CS is replaced and the brick is put back into the target.
The bricks were produced by a dedicated fabrication line, the Brick Assembly Machine (BAM), located underground near the OPERA detector to shield emulsions from cosmic ray background. The bricks are mounted into a wall structure: an ultra-light stainless-steel matrix of 52×64 trays. Each target section in SM1 and SM2 consists of 31 walls and can host up to 103000 bricks. The 150000 bricks produced for the experiment are arranged in 53 walls, 27 in SM1 and 26 in SM2, for a total mass of about 1.25 kton.
The bricks are moved in and out of the walls using an automated system called Brick Manipulator System (BMS). The BMS filled the target walls with the bricks produced by the BAM and extracts the bricks

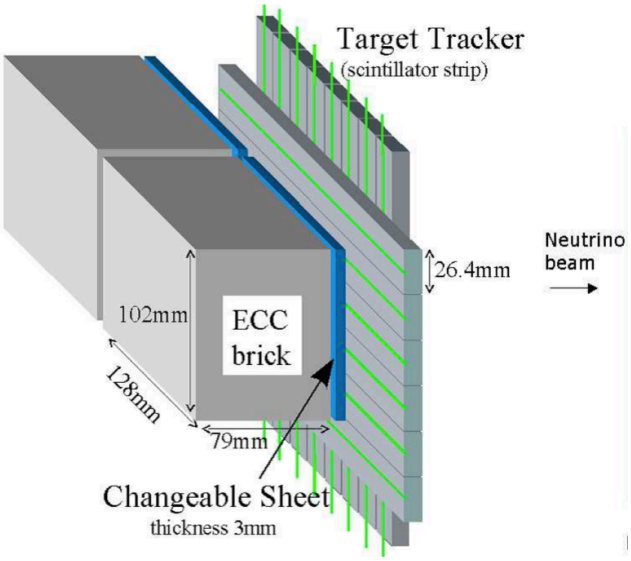

Figure 16: Schematic view of the brick with the Changeable Sheets (CS) in the target.

tagged by TT in real-time mode.
This modular and hybrid structure of the target allows to extract only the bricks actually hit by neutrinos, minimizing the ECC mass reduction during the run and achieving a quasi on-line analysis flow. In one day of data taking, about 20 neutrino interactions are recorded by OPERA and the related bricks are selected.

1.4.3 Automated scanning system

To analyze the large number of emulsions, two different systems, with comparable performances, were developed within the Collaboration: the S-UTS (Super-Ultra Track Selector) [70], in Japan, and the ESS (European Scanning System) from a joint effort of several european laboratories. The ESS [71, 72, 73], which can work at a speed of 20 $cm^2/h/layer$, consists of a Cartesian robot, holding the emulsion film on a horizontal stage movable in X-Y coordinates, with a CMOS camera, with resolution of 1280×1024 pixels, mounted on the optical axis (Z) of a microscope, along which it can be moved to change the focal plane with a step roughly equal to the focal depth of about 3 µm (Fig. 17).
The emulsion is held on a glass window of the stage by a vacuum pumping system; the illumination group, composed by a lamp and a condenser, focusing the light in the zone observed by the microscope objective, is placed under the scanning table. The control workstation

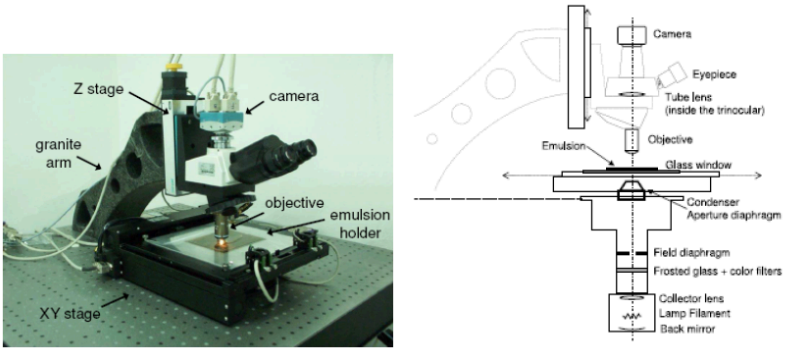

Figure 17: A photograph of the ESS microscope (left); a schematic view of the optical system of the microscope (right).

hosts a motion control unit that directs the stage to span the area to be scanned and drives the camera along the Z axis to produce optical tomographic image sequences (with the X-Y stage holding steady). Areas larger than a single field of view ($\sim 300 \times 400\ \mu m^2$) are scanned by repeating the data acquisition sequence on a grid of adjacent fields of view. The stage is moved to the desired position and the images are grabbed after it stops, with a stop-and-go algorithm.

The images, grabbed by the camera at the speed of 376 frames per second while the camera is moving in the Z direction, are sent to a vision processing board hosted in the control workstation to suppress the noise; this process enhances the image of developed grains, thus reducing the effect of residual optical aberrations for far-off-axis objects. Three dimensional sequences of aligned clusters (digitized images of the grains) are then reconstructed on the fly by the CPUs of the host workstation: a reconstructed cluster in an emulsion layer is called *micro-track* (Fig. 18). The position assigned to a micro-track is its intercept with the nearest plastic base surface. The linking of two matching micro-tracks of an emulsion plate (Fig. 18) produces the so called *base-track*. The full-volume wide reconstruction of particle tracks requires connecting base-tracks in several consecutive films. In order to define a global reference system a set of affine transformations relating track coordinates have to be computed to account for scanning data taken plate by plate in different reference frames, relative misalignments and deformations.

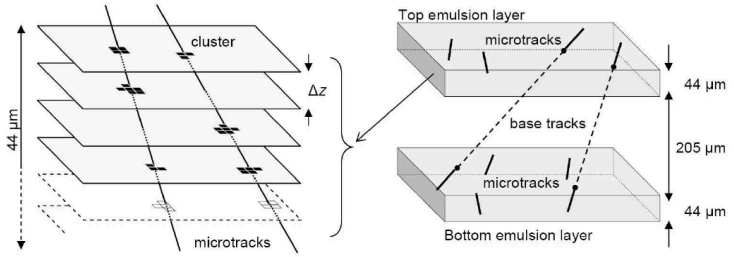

Figure 18: Micro-track reconstruction in one emulsion layer by combining clusters belonging to images at different levels; (right) micro-track connections across the plastic base to form base-tracks.

1.4.4 Tau signal

For the sake of completeness some considerations on the physics performances and background will be reported. This will be treated in detail in the following chapters.
The signal of the occurrence of $\nu_\mu \rightarrow \nu_\tau$ is the charged current interaction of ν_τ in the detector target ($\nu_\tau N \rightarrow \tau^- X$). The reaction is identified by the detection of the τ lepton. The τ channels investigated by OPERA are the electron, muon and hadron channels, as reported in Table 3.

Channel	**Branching ratio**
$\tau^- \rightarrow e^- \nu_\tau \overline{\nu}_e$	17.8 %
$\tau^- \rightarrow \mu^- \nu_\tau \overline{\nu}_\mu$	17.7 %
$\tau^- \rightarrow h^- \nu_\tau (n\pi^0)$	49.5 %
$\tau^- \rightarrow h^- h^- h^- \nu_\tau (n\pi^0)$	15.0 %

Table 3: Branching ratio for τ decay.

The τ decays inside the ECC are classified in two categories: long and short decays (Fig. 19). In long τ decays, decay occurs in the first or second downstream lead plate. τ candidates are selected on the basis of the detection of a reasonably large kink angle between the τ and the daughter tracks. Short decays correspond to the case where the τ decays in the same lead plate where the neutrino interaction occurred. The τ candidates are selected on the basis of the impact parameter (IP) of the τ daughter track with respect to the interaction vertex. It is therefore impossible to identify a short decay in case of quasi-elastic (QE) interactions, where only the τ is produced at primary vertex.

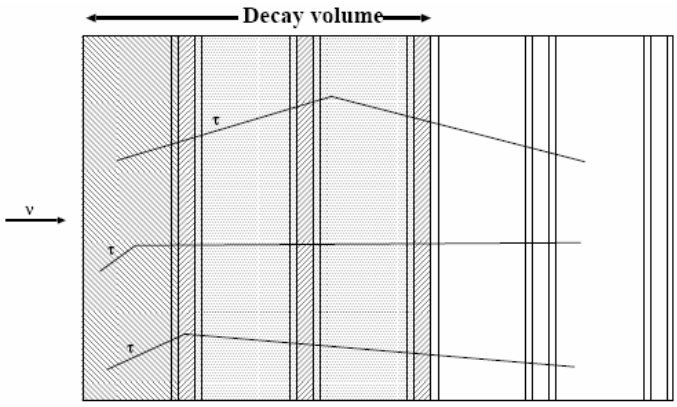

Figure 19: Different decay topologies; short decay (left-hatched region); long decay in base (right-hatched region) and long decay outside the base (shaded region).

1.4.5 Background

The main components of the physics background for the τ detection are:

- **Charmed particles decays**
  Charmed hadron production (D^+, D_s^+, Λ_c^+ and D^0) is the main background in the ν_τ search, since their flight length is similar to the τ. Selection criteria have thus similar efficiencies to detect the decay topology. Charm production in 1μ sample shows a muon originating from primary vertex and therefore does not mimic ν_τ interactions with $\tau \to \mu$ decay. On the contrary, when the muon is misidentified, charm production shows the same topology as ν_τ interactions.

- **Hadronic re-interactions**
  A source of background to the $\tau \to h$ and $\tau \to 3h$ channel is due to re-interactions of hadrons in lead from ν_μ NC and ν_μ CC events where the primary muon is not identified.

- **Large angle muon scattering**
  Muons produced in ν_μ CC events and undergoing a scattering in the lead plate following the vertex plate could mimic a muonic τ decay.

- **Prompt ν_τ from CNGS target**
  The CNGS beam has a small contamination of D_s mesons. A fraction of the D_s decays into the τ channel. The decay of the τ then produces a ν_τ. Taking into account the cross section, the

branching ratio, the features of the beam and the distance of the detector to the source, the expected contribution is of the order of $O(10^{-7})$ ν_τ CC interactions per ν_μ CC event and therefore negligible.

2 TAU SEARCH

The analysis of a neutrino interaction in the OPERA target consists of different phases: the electronic detector trigger, the event classification in either 1μ or 0μ channel, the brick identification procedure, the changeable sheet analysis, the event location in emulsion, the vertex reconstruction, the decay search and the kinematical selection. In this chapter all these steps are described together with their Monte Carlo simulation.
The efficiencies of all the steps of the analysis have been evaluated for the different τ decay modes, either with a short or a long topology, for deep-inelastic interactions (DIS) and quasi-elastics plus resonances (QE).
During the OPERA runs, two different selections have been defined:

- SELECTION A (2008-2009 data)
  In order to gain confidence on our data, for the first two runs no kinematical cut was applied. High probable and second probable bricks per event have been analysed.

- SELECTION B (2010÷2012 data)
  Once a good description of the data was achieved, a kinematical selection for 1μ events ($| p_\mu | < 15$ GeV/c) was applied in order to speed-up the analysis without reducing the τ signal. Only the high probable brick for 0μ events has been analyzed, being it more efficient for the τ search.

2.1 MONTE CARLO SIMULATION

The software framework used in the OPERA experiment is called OpRelease. It is written in C++ code and based on ROOT classes. It is managed by the Concurrent Versions System (CVS) and stored on the

OPERA CVS repository at CERN. The OpRelease software has been built within the CMT environment, the Configuration Management Tool, that handles system configuration, dependencies and compilation. It has been conceived as a tool for both data and MC analysis and it is structured in several sub-packages which take care of different steps in the simulation chain:

OpNegn is the neutrino event generator in the OPERA experiment. It is based on the NEGN neutrino generator that profits from the experience of the NOMAD experiment, from which it is derived, where a large sample of ν interactions with their final states was accumulated. The adaptations needed for the OPERA experiment include the description of the beamline, the neutrino energy and the CNGS target.

OpRData describes the data format.

OpGeom describes the geometry of the detector (size, positions and material features). A description of Borexino, the experiment located in the same hall C just upstream of OPERA, is also taken into account.

OpSim reproduces the particle propagation inside the detector with the concurrent creation of track hits in the various sub-detectors. OpSim is based on the ROOT Virtual Monte Carlo (VMC): a generalized Monte Carlo allows the user to choose the transport generator between GEANT 3.21 and Geant4, for the whole detector, or FLUKA, only for the bricks.

OpDigit simulates the detector response. It takes into account the attenuation of the signal amplitude due to the propagation on the cables and optical fibers and converts the energy deposit on RPC gas and on emulsion respectively in the detected electric signal on the end of the *strip* and on the recorded segment in the emulsion.

OpRec performs many tasks, such as: cross-talk removal, tagging of events on time with the beam, reconstruction of the tracks with electronic detectors, muon identification and event energy evaluation.

OpCarac classifies the events into several classes: events with a muon coming from outside the detector, events originated in the iron of the spectrometer, border events or contained events.

OpBrickFinding is the package predicting the brick where the neutrino interaction occurred. It produces a probability map and evaluate for each brick the probability to contain the event.

OpEmuIO simulates the scanning system and produces the micro-tracks. It applies the scanning system efficiencies and applies a Gaussian smearing on position and slope of the micro-tracks according to the measurement errors.

OpEmuRec is the package for the emulsion data analysis.

2.2 ELECTRONIC DETECTOR TRIGGER

The data acquisition trigger selects only events on time with the beam: a coincidence with the two 10.5 μs wide, 50 ms separated CNGS spills is required. The electronic detector trigger is then defined as the presence of hits in the X and Y projections in at least two TT planes or a TT plane with the sum of the photomultiplier signals exceeding 1500 ADC counts and the presence of at least 10 hits.
The trigger efficiency for all the τ decay channels is >98%.

2.3 EVENT CLASSIFICATION

Triggered events are then classified as being 1μ or 0μ, according to electronic detector response.
The event is classified as 1μ if one of the following conditions is satisfied:

- a three-dimensional track with a length $\times$ density value larger than 660 g/cm^2 is reconstructed
- the number of TT or RPC planes having at least one hit is larger than 20.

The complementary sample is defined as 0μ.
The momentum of the tracks is calculated from their curvature in the spectrometer magnetic field. The muon momentum (p_μ) is defined as the momentum of the longest 3D track.
The reliability of the electronic detector simulation was studied by comparing located data with a Monte Carlo sample including ν_μ simulated interactions. The muon momentum distribution for events classified as 1μ interactions in the target is shown in the left panel of Figure 20, while in the right panel the visible energy in the Target Tracker for 0μ

events is reported. The simulation is in good agreement with data. The event classification efficiency has been evaluated for all the τ decay channels. The results are reported in Table 4.

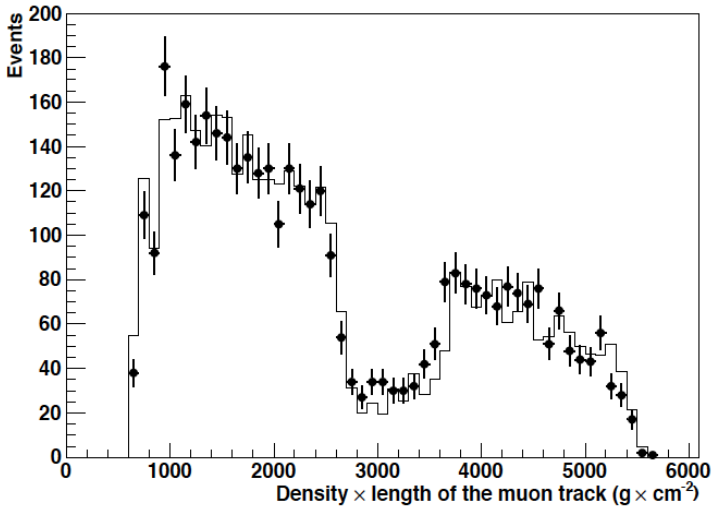

Figure 20: Length $\times$ density comparison for data (dots with error bars) and MC (solid line) for events classified as CC (i.e. length $\times$ density > 660 g $\times$ cm^{-2}).

	ϵ_{ED}(%)		
	LONG DIS	SHORT DIS	LONG QE
$\tau \to h$	78.8 ± 0.8	82.6 ± 0.8	87.2 ± 0.5
$\tau \to 3h$	69.9 ± 0.7	74.7 ± 0.7	78.4 ± 0.7
$\tau \to \mu$	82.5 ± 0.7	79.4 ± 1.0	84.1 ± 0.4
$\tau \to e$	89.8 ± 0.8	88.1 ± 0.9	85.2 ± 0.6

Table 4: Summary of the electronic detector classification efficiency for different τ decay modes, topologies (long and short) and type of events (DIS and QE).

2.4 EVENT CONTAINMENT

Subsequently the OpRec algorithm is applied and the OpCarac result is checked to know if the event is classified as contained in the target. Only events that are marked as *contained* (i.e. the interaction point lies within the target area) or *bordersoftnc* (i.e. NC-like neutrino interaction in the target area close to its border) by the package OpCarac [75] of the OPERA software are retained. The results are shown in Table 5.

$\epsilon_{OpCarac}$(%)			
	LONG DIS	SHORT DIS	LONG QE
$\tau \to h$	96.6 ± 0.5	95.2 ± 0.5	93.1 ± 0.3
$\tau \to 3h$	95.7 ± 0.4	95.5 ± 0.4	96.7 ± 0.3
$\tau \to \mu$	96.9 ± 0.4	98.3 ± 0.4	96.0 ± 0.3
$\tau \to e$	93.8 ± 0.7	92.5 ± 0.9	86.6 ± 1.0

Table 5: Summary of the event containment efficiency for different τ decay modes, topologies (long and short) and type of events (DIS and QE).

2.5 BRICK IDENTIFICATION

When a trigger of the electronic detector is compatible with a neutrino interaction in the detector, a reconstruction algorithm analyses the electronic detector data to build a probability map of the bricks, where probably the neutrino interaction occurred. The bricks are ranked according to the decreasing probability (P_0 for the highest probable brick, P_1 for the second probable brick, etc.). Moreover, for events with a muon in the final state (1μ), a prediction for the slope of the muon and its position in the Changeable Sheets (CS) is also given; for 0μ events, the averaged center of TT hits provides the impact point of the hadron shower on the CS.
In order to create the brick response in the Monte Carlo, the OpEmuIO algorithm is applied and for each event an array of $3\times3\times3$ bricks, around the brick where the interaction occurred, is created. Then the brick identification algorithm is applied. The results for the two described selections are shown in Tables 6 and 7, respectively.
The lowest efficiencies are obtained for QE events with a single track (QE $\tau \to h$ events). The highest efficiencies are for QE $\tau \to \mu$ and DIS $\tau \to \mu$ events, where the brick identification is facilitated by the presence the muon track penetrating the electronic detectors.
The values of Table 6 are larger by a factor of about 1.3 (up to 1.5 for some channels) than those reported in the 7. This factor provides the increase of efficiency given by the analysis of two bricks.

2.6 CHANGEABLE SHEET ANALYSIS

The emulsion scanning of the event starts from the interface emulsion films, the Changeable Sheets attached downstream of the brick, according to the slope and position reconstructed by the Target Tracker. The

ϵ_{BF}(%) - SELECTION A -			
	LONG DIS	SHORT DIS	LONG QE
$\tau \to h$	78.5 ± 1.0	77.8 ± 1.0	61.7 ± 0.8
$\tau \to 3h$	80.9 ± 0.8	81.4 ± 0.8	73.1 ± 0.8
$\tau \to \mu$	84.5 ± 1.0	83.8 ± 1.1	91.5 ± 0.4
$\tau \to e$	68.1 ± 1.4	71.8 ± 1.5	53.9 ± 1.5

Table 6: Brick selection efficiency for selection A.

ϵ_{BF}(%) - SELECTION B -			
	LONG DIS	SHORT DIS	LONG QE
$\tau \to h$	61.6 ± 1.0	60.7 ± 1.0	47.5 ± 0.8
$\tau \to 3h$	63.4 ± 1.0	64.1 ± 1.0	55.5 ± 0.8
$\tau \to \mu$	67.0 ± 1.3	68.6 ± 1.4	60.4 ± 0.7
$\tau \to e$	53.8 ± 1.5	54.8 ± 1.7	36.4 ± 1.6

Table 7: Brick selection efficiency for selection B.

scanning area is defined according to the event classification: in case of 1μ events a rectangular area of 4×3 cm^2 around the predictions provided by the electronic detector is scanned; in case 0μ the area is 8×6 cm^2.

The following step is the reconstruction of all the base-tracks in the selected area of both changeable sheets. After base-track reconstruction a first alignment between the two CS films is performed using the X-ray spots printed soon after the brick extraction and tracks crossing both CS films are searched for. A coincidence of base-tracks in the two different films is called *double base-track*. Moreover, to recover intrinsic inefficiencies affecting the microtracks reconstruction, coincidences of a micro-track and a base-track (3/4 *tracks*) belonging to different films are also taken into account. This can be done only if a micrometric alignment of the films, not available with the X-rays spots, is achieved. This micrometric alignment is obtained exploiting the low energy electrons originating from radioactive isotopes present in the emulsion, as shown in Figure 21 [64].

Once a track crossing both CS films is found (double base-track or 3/4 track), the match with tracks reconstructed by electronic detector is searched for according a χ^2 method based on the slope and position residual between electronic prediction and emulsion double base-

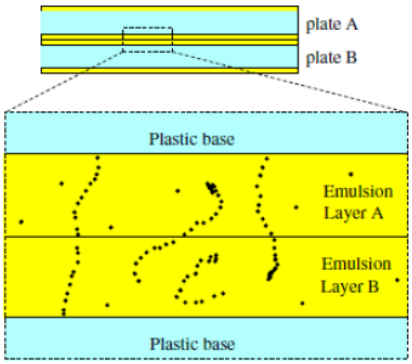

Figure 21: Schematic diagram of the alignment with low energy electrons.

tracks. The base-tracks belonging to muon originating from the neutrino interactions in the rock in front of detector (*rock muon*) or from secondary cosmic rays are rejected and the base-tracks belonging to the muon of the 1μ event are tagged (*muon candidate*). Finally for the event validation, one of these three conditions has to be satisfied:

- a pattern of at least two converging tracks is found;
- a muon candidate is found;
- a track compatible with an isolated three dimensional track reconstructed by the electronic detector is found.

The CS efficiency is reported in Table 8 for the different τ decay channels.

ϵ_{CS}(%)			
	LONG DIS	SHORT DIS	LONG QE
$\tau \to h$	88.7 ± 1.0	86.2 ± 1.1	24.4 ± 1.0
$\tau \to 3h$	95.6 ± 0.5	95.5 ± 0.5	84.2 ± 0.9
$\tau \to \mu$	80.6 ± 0.9	75.4 ± 1.2	49.0 ± 0.8
$\tau \to e$	83.7 ± 1.5	79.4 ± 1.8	37.3 ± 1.9

Table 8: Summary of the changeable sheet efficiency for different τ decay modes, topologies (long and short) and type of events (DIS and QE).

2.7 TRACK FOLLOW-UP

The procedure to localize the neutrino interaction point inside the brick is called *scan-back* procedure. CS candidates connected to bricks are followed up, plate-by-plate until their disappearance. An automatic scanning system searches for base-tracks compatible with the predicted tracks by scanning a single microscope view centered at the expected position. The scan-back track stops if the track is missing in three consecutive plates, the most downstream of which is defined as vertex plate (Figure 22).
The scan-back efficiency is defined as the percentage of cases where at least one scan-back track stops within five plates from the true primary vertex. The results are reported in Table 9.

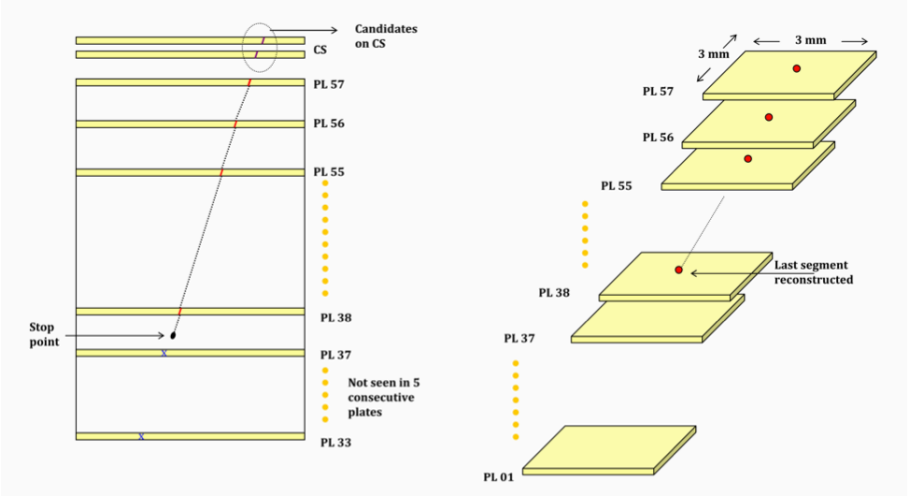

Figure 22: Schematic representation of the scan-back procedure. The track segments (in red) are reconstructed in the emulsion sheets (yellow). When the track disappears for three consecutive plates the interaction point is located.

2.8 VOLUME-SCAN AND LOCATION

Once the stopping plate has been identified, additional scanning is performed to confirm the interaction and study its topology.
A sketch of *volume-scan* is reported in Figure 23. It is 1cm wide in each transverse direction and 19.5 mm along the beam direction, corresponding to fifteen emulsion plates. It contains the vertex plate in

	ϵ_{SB}(%)		
	LONG DIS	SHORT DIS	LONG QE
$\tau \to h$	90.7 ± 0.8	91.7 ± 0.8	80.7 ± 1.4
$\tau \to 3h$	98.0 ± 0.3	97.3 ± 0.4	95.8 ± 0.5
$\tau \to \mu$	96.9 ± 0.5	96.5 ± 0.6	98.3 ± 0.2
$\tau \to e$	85.3 ± 1.5	87.0 ± 1.6	57.6 ± 1.8

Table 9: Summary of the scan-back efficiency for different τ decay modes, topologies (long and short) and type of events (DIS and QE).

the fifth upstream plate. The most upstream plates act as a veto for passing through tracks. The ten plates downstream of the vertex plate are meant for the particle tracking.

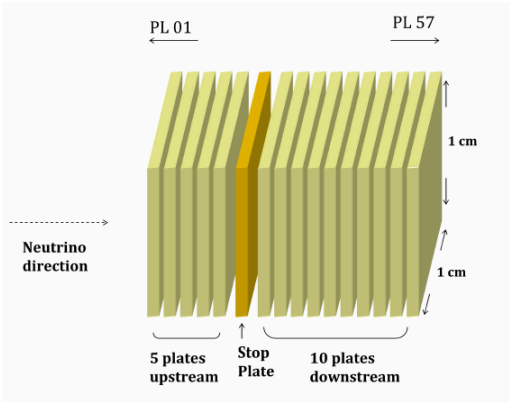

Figure 23: Schematic representation of a total scan volume. 1 cm^2 is scanned around the stopping point on 10 plates downstream and 5 upstream with respect to the lead plate in which the interaction supposed to be.

The scanning area is centered around the predicted position of the interaction vertex. The angular acceptance of the scanning is 600 mrad with respect to the beam direction.
As an example, in Figures 24 and 25 we show a CC and a NC event, respectively, fully reconstructed in the brick.
In order for an event to be classified as located, a geometrical cut is defined: the volume-scan must be sufficiently large to perform the decay search. This corresponds to having the primary vertex at least three emulsion films upstream of the border of ECC brick, i.e. within the range of films 1-54, out of the 57 films the brick is made of. The results of the location efficiency are reported in Table 10.
The relevant kinematical variables at the primary vertex for 1μ events

are reported in Figure 26, both for data and Monte Carlo simulation: the slopes of the tracks attached to the primary vertex, the ϕ angle between the muon and the hadron jet in the plane transverse to neutrino direction, the momentum of the tracks. A good agreement is found, thus validating the reliability of the simulation.

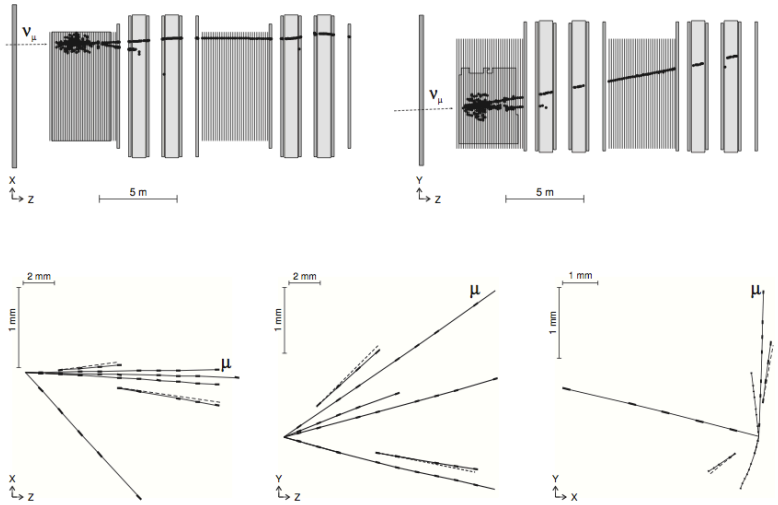

Figure 24: Top panels: online display of one CC event seen by the OPERA electronic detectors. Bottom panels: the emulsion reconstruction is shown in top view (bottom left), side view (bottom center), front view (bottom right).

	ϵ_{LOC}(%)		
	LONG DIS	SHORT DIS	LONG QE
$\tau \to h$	96.3 ± 0.6	96.5 ± 0.6	87.5 ± 1.3
$\tau \to 3h$	95.5 ± 0.5	96.8 ± 0.4	94.8 ± 0.5
$\tau \to \mu$	95.4 ± 0.6	94.8 ± 0.8	87.8 ± 0.7
$\tau \to e$	94.3 ± 1.0	95.7 ± 0.9	85.9 ± 1.9

Table 10: Summary of the location efficiency for different τ decay modes, topologies (long and short) and type of events (DIS and QE).

2.9 DECAY SEARCH

The decay search procedure is meant to search for short lived particle decays, such as τ and charmed particles. It consists of several steps,

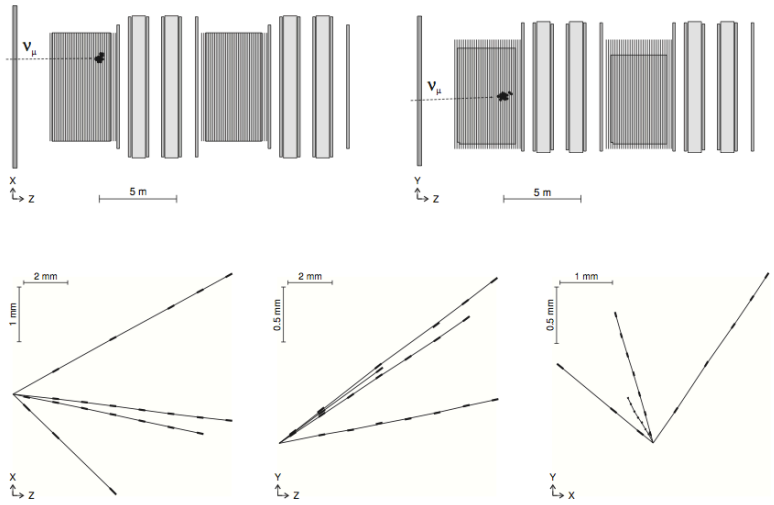

Figure 25: Top panels: online display of one NC event seen by the OPERA electronic detectors. Bottom panels: the emulsion reconstruction is shown in top view (bottom left), side view (bottom center), front view (bottom right).

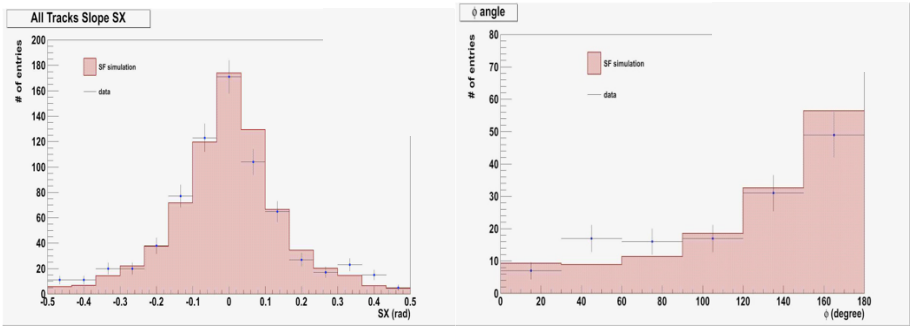

(a) Track slope **(b)** ϕ angle

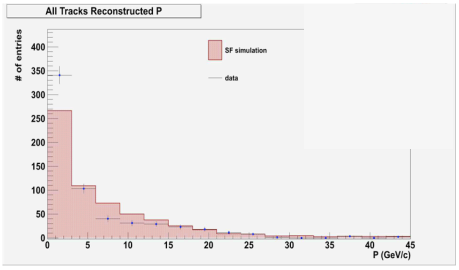

(c) Momentum

Figure 26: Comparison between data (black cross) and Monte Carlo simulation (red shaded area) for the relevant kinematical variables at the primary vertex.

described in the following. The results of the procedure for all the τ decay channels are then reported in Table 11.

2.9.1 Primary vertex definition

In order to improve the resolution in the determination of the position of the primary vertex, the track information in the film immediately downstream of the primary vertex is required. Track segments in the vertex film could be missing in the reconstruction because of tracking inefficiency. Moreover, electron-positron pairs coming from the conversion of γ produced in π^0 decays and pointing to the vertex can spoil its accuracy.
By visually inspecting the vertex film, the parameters of the track segments recognised by eye are measured and used to re-compute the vertex position. The visual inspection also allows the identification of e^+e^- pairs, that are removed in the determination of the primary vertex.
If a track is found to have an impact parameter larger than 10μm, it has to be further studied in order to investigate whether the reason for such an anomaly can be the scattering of the particle in the traversed lead thickness. An estimation of its momentum is thus performed with the multiple Coulomb scattering (MCS) algorithm [76]. A cut $p < 1 GeV/c$ defines the *low momentum particles* to be disconnected from the vertex for a more accurate determination of its position. Once the primary vertex has been defined, any track with an anomalous impact parameter that cannot be explained in terms of scattering has to be carefully investigated to check for the presence of a possible decay.
The impact parameter distribution of the tracks in 1μ neutrino interactions with respect to the reconstructed vertex position and the event track multiplicity distribution are shown in Figure 27, for data and Monte Carlo. More than 95% of the tracks have impact parameter smaller than 10μm. The tail of the distribution is due to low-energy particles.

2.9.2 Extra-track search

The decay of a short-lived particle can also be detected by searching for possible daughter tracks (*extra-tracks*) reconstructed in the total scan but not associated to the primary vertex.
An extra-track is selected if the following criteria are satisfied:

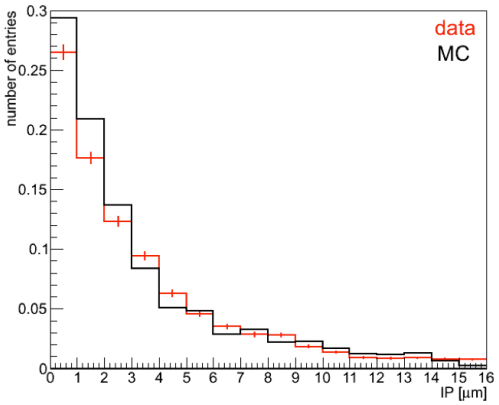

Figure 27: Impact parameter distribution of the primary tracks in 1μ events with respect to the reconstructed vertex, after the decay search procedure. The average value is 3.3μm. The entries are normalized to unity.

- the longitudinal distance between the vertex and the most upstream segment of the track (Δz) is smaller than 3.6 mm;
- the impact parameter with respect to the vertex is smaller than 300μm if Δz <1mm, or smaller than 500μm otherwise;
- the track has at least three segments in the reconstruction.

Extra-tracks are then inspected to filter out e^+e^- pairs from γ conversion, particles not originating in the measured volume (typically, low momentum particles reconstructed as shorter tracks due to multiple Coulomb scattering) and fake tracks due to the impurity of the reconstruction program.

2.9.3 Parent search

A dedicated *parent search* procedure is applied to extra-tracks starting downstream of the vertex film to detect long decays. It consists in searching for a track connecting the selected extra-track to the reconstructed vertex, with an impact parameter with respect to the vertex smaller than 10μm and a minimum distance from the daughter track smaller than 20μm. A cut on the *kink* angle, defined as the difference in slope between the parent and the daughter tracks, larger the 20 mrad is also defined (Figure 28). Any candidate parent track selected according to these criteria is validated by visual inspection.

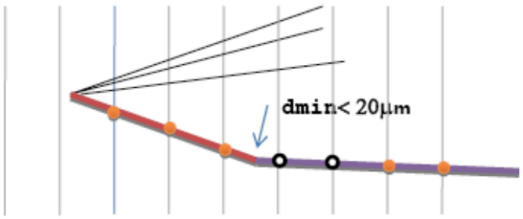

Figure 28: The parent search procedure consists in searching for segments connecting an extra track to the primary vertex.

2.9.4 In-track search

A search for possible *small* kinks along the tracks attached to the neutrino interaction, not automatically detected in the reconstruction of total-scan data, is performed in a fiducial volume of 4 films downstream of the vertex, relevant for short-lived particles. The procedure is applied to all tracks for 0μ events. As for interactions with a reconstructed μ in the electronic detectors, the method is applied only to the track matching the muon prediction.
Track by track, the largest angular difference is computed in the 4 most upstream films. If it exceeds the angular resolution of the track and the kink angle is larger than 0.015 rad, the momentum of the track is measured, as described is section 2.9.2.

	ϵ_{DS}(%)		
	LONG DIS	SHORT DIS	LONG QE
$\tau \to h$	55.8 ± 1.5	36.7 ± 1.5	55.9 ± 2.1
$\tau \to 3h$	57.5 ± 1.2	37.5 ± 1.1	18.8 ± 0.9
$\tau \to \mu$	52.2 ± 1.6	27.5 ± 1.7	52.6 ± 1.1
$\tau \to e$	45.4 ± 2.3	33.3 ± 2.3	28.9 ± 2.4

Table 11: Summary of the decay search efficiency for different τ decay modes, topologies (long and short) and type of events (DIS and QE).

2.10 CHARM PRODUCTION AS CONTROL SAMPLE

Charmed hadrons have lifetimes similar to those of the τ lepton (10^{-13}s) and share analogous decay topologies. The finding efficiency of the decay vertices is therefore also similar for both types of particles. Com-

paring the observed charm event sample in size and decay topologies with expectations from simulations constitutes a straightforward way to verify that τ decay selection criteria and their corresponding efficiencies are well understood.
By using the results recently published by the CHORUS experiment [77], it is possible to estimate the ratio between the neutrino induced charm-production cross-section and the inclusive neutrino charged current-cross section at the OPERA energies:

$$\frac{\sigma(\nu_\mu N \to \mu^- X)}{\sigma(\nu_\mu N \to \mu^- C X)} = (4.38 \pm 0.26)\%.$$

In particular, the neutral charm component is $\sigma^{D^0}/\sigma^{CC} = (1.91 \pm 0.13)\%$ and the charged charm component $\sigma^{C^+}/\sigma^{CC} = (2.47 \pm 0.22)\%$.
The decay search procedure described above has been applied to a Monte Carlo sample of ν_μCC interactions with charm production.
In addition to the selection criteria that have been described, a charm event has to satisfy the following conditions:

- in case of one prong decay, the kink angle (θ_{kink}) between the charmed meson and the daughter particle is larger than 20 mrad;
- in case of one prong decay, the momentum of the daughter particle is larger than 1 GeV/c.

The decay search efficiency was estimated to be 59±9% for long charm decays and 18±2% for short charm decays. The efficiency was used to calculate the number of expected charm events in the OPERA experiment for 2884 ν_μCC interactions analyzed in the 2008, 2009 and 2010 runs.
The main sources of background in the charm sample are the hadronic re-interactions and the non-charmed short lived particles decays, as K^0_s and Λ. Both contributions have been studied with a detailed Monte Carlo simulation. The background component is mainly due to hadronic re-interactions, amounting to 85% of the total background.
In the sample of 2884 ν_μCC interactions analyzed, a total of 50 charm candidate events were observed, while 41±7 charm and 14±3 background events were expected. The observed fractions of the different decay topologies are reported in Table 12. The number of observed charm events in the different decay topologies are statistically compatible with MC expectation.
The comparison between data and Monte Carlo simulation is shown in Figure 29 for the most relevant variables: the track multiplicity at primary vertex (Fig. 29a), the impact parameter of daughter tracks with respect to the primary vertex (Fig. 29b), the decay length of charmed

hadrons (Fig. 29c), the ϕ angle between the charmed hadron and the primary muon in the plane transverse to the beam direction (Fig. 29d). There is a good agreement between experimental and simulated data both in the number of expected charm events and in the quoted distributions. For all the listed variables a very good agreement is observed, with a value of the Kolmogorov test larger than 0.99.

	EXPECTED EVENTS			
TOPOLOGY	CHARM	BACKGROUND	TOTAL	OBSERVED
1 prong	20 ± 5	9 ± 3	29 ± 6	19
2 prong	15 ± 4	4 ± 1	19 ± 4	22
3 prong	5 ± 2	1.0 ± 0.3	6 ± 2	5
4 prong	0.8 ± 0.4	< 0.01	0.8 ± 0.4	4
TOTAL	41 ± 7	14 ± 3	55 ± 7	50

Table 12: Comparison between charm event topologies observed and expected from simulations including background.

2.11 KINEMATICAL SELECTION

If an event has been located and a decay topology has been detected by the procedure described above, a high resolution scanning is applied on the primary and daughter tracks in order to determine their energy. A kinematical selection is then applied to discriminate between signal and background. Several cuts have been defined on kinematical variables evaluated at primary and secondary vertices, depending on the tau decay channel.

2.11.1 $\tau \to h$

The hadronic single-prong decays of the τ lepton are selected among the events with no detected muon or electron daughter. Severe cuts are applied both at the decay and at the primary vertex in order to suppress the background.
A cut on the transverse momentum at the secondary vertex (p_T) is applied. p_T must fulfill the condition p_T >600 MeV/c if no γ's are attached to the decay vertex and p_T >300 MeV/c otherwise. The stronger

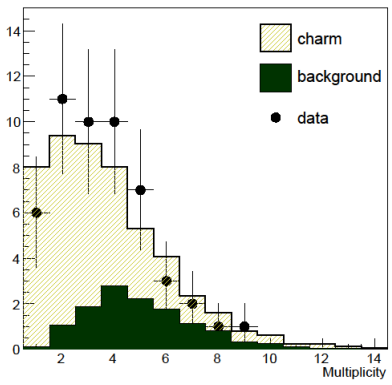

(a) Primary vertex multiplicity

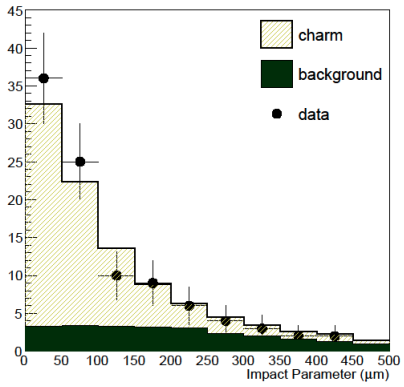

(b) Impact parameter of daughter tracks with respect to primary vertex

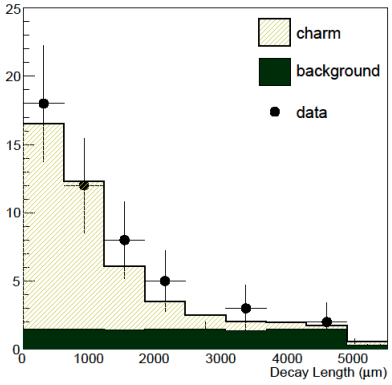

(c) Decay length of the charmed hadron candidate

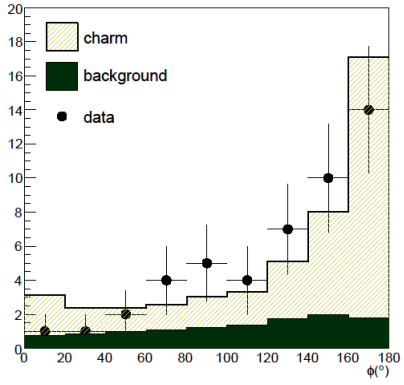

(d) Phi angle between the charmed hadron candidate and the primary muon

Figure 29: Comparison between data and Monte Carlo for the charm control sample. Data are shown as black dots, while the Monte Carlo distributions as histograms both for charm signal (light yellow) and background (dark green). A good agreement is observed for all the variables.

cut is justified by the relatively small $\langle p_T \rangle (<100$ MeV/c) in elastic or inelastic pion interactions, while the average p_T in hadronic τ decays is ~550 MeV/c. The daughter particle is required to have a momentum larger than 2 GeV/c in order to suppress the low energy hadrons which are produced in ν_μNC interactions.
The kinematical analysis at the primary vertex uses the p_T^{miss} and the ϕ_{mod} angle. The p_T^{miss} is defined as the missing transverse momentum at the primary vertex. The ϕ_{mod} angle is defined as the angle in the transverse plane between the parent track and the primary hadronic shower direction. The hadron with largest angle with respect to the parent is discarded unless it is classified as a hadron (Figure 30).
In NC interactions p_T^{miss} is expected to be larger due to the unobserved outgoing neutrino. Conversely, it is expected to be small in CC interactions. For τ candidates the measured p_T^{miss} is required to be lower than 1 GeV/c. The ϕ_{mod} angle is expected to peak at π, because the τ and the hadronic shower tend to be back-to-back in the transverse plane. Conversely, in NC interactions, the hadron faking the τ decay is produced inside the hadronic shower and ϕ_{mod} peaks near zero. For τ candidates the ϕ_{mod} angle is required to be larger than $\pi/2$.
The Δz variable is defined as the distance (z-axis) between the secondary vertex and the edge of the first lead plate immediately downstream of the primary vertex (Figure 31). According to this definition, short decays have $\Delta z < 0$. A cut on the Δz smaller than 2600μm and on the angle between the parent and the daughter track (θ_{kink}) larger than 20 mrad is also applied.
The distributions of the p_T and the θ_{kink} are reported in Figure 32.

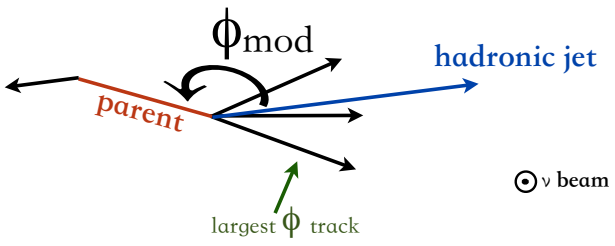

Figure 30: Definition of the ϕ_{mod} variable. The primary track, farest to the τ in the neutrino transverse plane, is discarded from the hadron jet unless it is classified as a hadron.

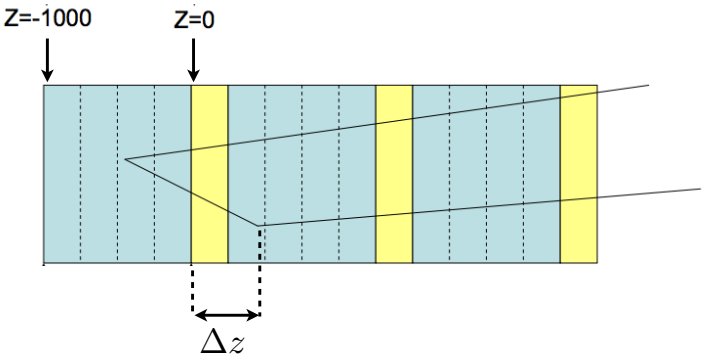

Figure 31: Definition of the Δz variable.

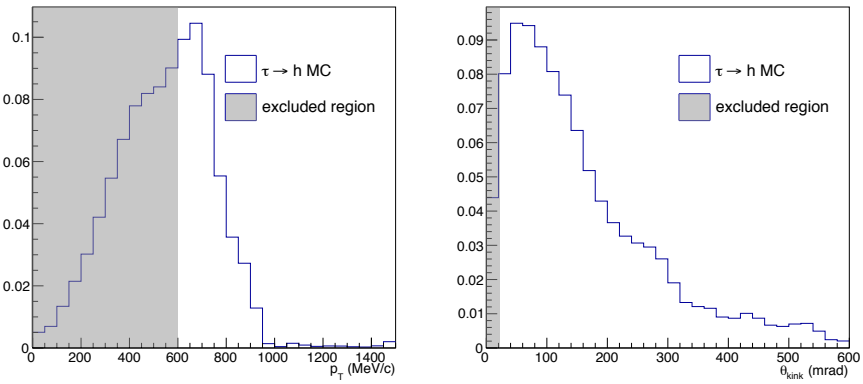

(a) Transverse momentum at secondary vertex

(b) Kink angle

Figure 32: Distribution of kinematical variables for DIS $\tau \to h$ decays. The grey area represents the excluded region corresponding to the selection cuts.

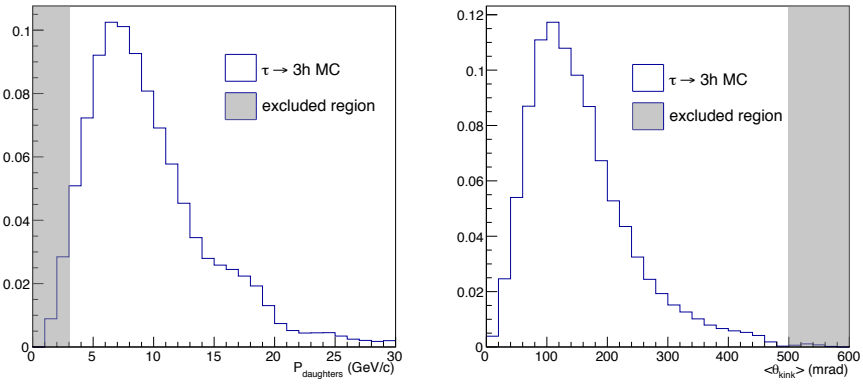

(a) Sum of daughters momenta **(b)** Average kink angle

Figure 33: Distribution of kinematical variables for DIS $\tau \to 3h$ decays. The grey area represents the excluded region corresponding to the selection cuts.

2.11.2 $\tau \to 3h$

As for the decay in one hadron, the τ decay in three hadrons has to satisfy the cut at p_T^{miss}smaller than 1 GeV/c and ϕ_{mod} angle larger than $\pi/2$. Δz is required to be smaller than 2600 μm and the average of the three daughters kink angles with respect to the parent track ($\langle\theta_{kink}\rangle$) should be smaller than 500 mrad.
To suppress the hadronic background, the scalar sum of the daughters momenta (p_{TOT})is required to be larger than 3 GeV/c.
The invariant mass and the minimum invariant mass [78] of the three daughters' system are also evaluated: both variables have to lie in the range 0.5-2 GeV/c^2.
The distributions of the p_{TOT} and the $\langle\theta_{kink}\rangle$ are reported in Figure 33.

2.11.3 $\tau \to \mu$

The muonic decays of the τ lepton are selected among the events where daughter is identified as a muon by electronic detectors.
It is required that the momentum of the muon lies in the range 1-15 GeV/c. The lower cut allows to reject events for which the μ identification is poor and to reduce possible background from low energy hadrons. The upper cut reduces ν_μ CC events by about 30% with a small loss of the signal. This selection reduces the background from scattering of a prompt muon in the lead.
The p_T at decay vertex must fulfill the condition p_T >250 MeV/c.

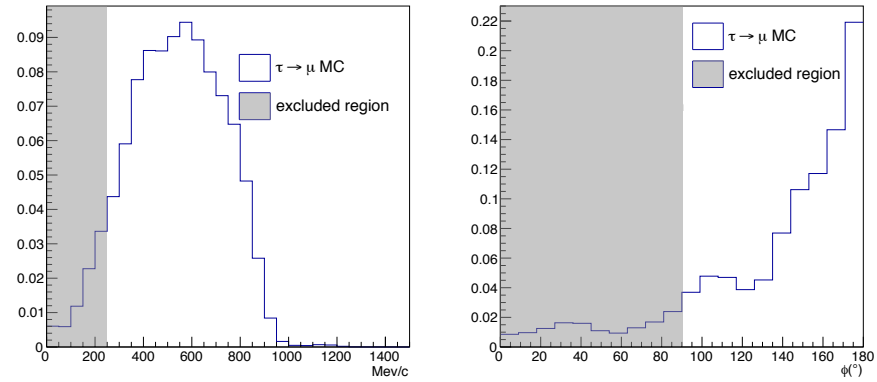

(a) Transverse momentum at secondary vertex

(b) ϕ_{mod} angle

Figure 34: Distribution of kinematical variables for DIS $\tau \to \mu$ decays. The grey area represents the excluded region corresponding to the selection cuts.

A cut on Δz smaller than 2600 μm and on the angle between the parent and the daughter track (θ_{kink}) larger than 20 mrad is also applied.
The distributions of the p_T and the ϕ_{mod} are reported in Figure 34.

2.11.4 $\tau \to e$

The τ decay in electron has to satisfy the cut at p_T larger than 100 MeV/c in order to suppress the contamination from ν_eCC.
To reduce the background from low energy electrons ($\gamma \to e^+e^-$) the τ daughter is required to have an energy higher than 1 GeV. This cut also allows to have a better electron identification. In addition, an upper cut (15 GeV) on the electron energy reduces the background from prompt electrons produced in ν_eCC interactions.
A cut on Δz smaller than 2600 μm and on the angle between the parent and the daughter track (θ_{kink}) larger than 20 mrad is also applied.

The kinematical efficiencies for all the channels are summarized in Table 13.

2.12 TRACK FOLLOW-DOWN

In order to further reduce the muon identification inefficiency, all tracks at the primary vertex of a candidate event are followed within the brick

	ϵ_{KIN}(%)		
	LONG DIS	SHORT DIS	LONG QE
$\tau \to h$	46.2 ± 2.4	44.5 ± 2.1	31.0 ± 2.7
$\tau \to 3h$	49.1 ± 1.8	48.6 ± 1.6	64.3 ± 2.5
$\tau \to \mu$	9.16 ± 2.8	77.7 ± 2.9	79.7 ± 1.5
$\tau \to e$	83.0 ± 2.4	82.0 ± 2.1	22.1 ± 2.7

Table 13: Summary of the kinematical efficiencies for different τ decay modes, topologies (long and short) and type of events (DIS and QE).

in which the event occurs and then in all the downstream bricks until the tracks stops or interacts. This procedure, called *track follow-down*, allows to recover muons not identified by electronic detectors through range-momentum correlation and the topology of their end-point.
If the stopping point occurs inside a brick, a volume of about $2\ cm^3$ is scanned and analysed in order to reconstruct the products of the particle decay or interaction.
The track is classified as hadron if an interaction vertex with one or more prongs is detected. If this is not the case, the connection between its range and momentum is evaluated. A discriminating variable is defined

$$D_{TFD} = \frac{L}{R_{lead}(p)} \frac{\rho_{lead}}{\rho_{average}} \tag{18}$$

where L is the track length, $R_{lead}(p)$ is the range in lead of a muon with a momentum p, $\rho_{average}$ is the average density along the path and ρ_{lead} is the lead density.
The distribution of the D_{TFD} variable for hadrons and muons is reported in Figure 35.
If $D_{TFD} > 0.8$ the track is classified as a muon, as a hadron otherwise. The efficiency of this cut is 63%.
Muons may be identified also if the electron from its decay is seen in the emulsions.
In a small fraction of cases, the track follow-down procedure can wrongly identify a primary hadron as a muon, thus affecting the selection of the τ signal.
The track follow-down efficiencies for all the channels are summarized in Table 14. Being applied only to tracks attached to the primary vertex, this procedure affects only DIS interactions.

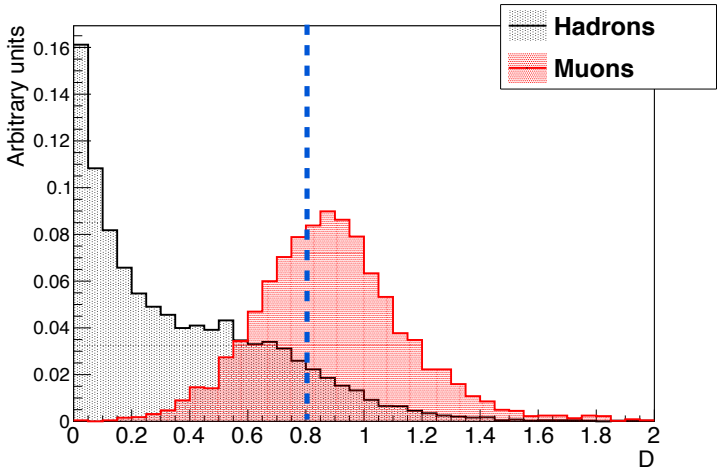

Figure 35: Distribution of the track follow-down discriminating variable D_{TFD}, for hadrons (grey area) and muons (pink area). The vertical line represents the cut defined.

	ϵ_{TFD}(%)		
	LONG DIS	SHORT DIS	LONG QE
$\tau \to h$	93 ± 1	93 ± 1	100
$\tau \to 3h$	94 ± 1	94 ± 1	100
$\tau \to \mu$	97 ± 1	97 ± 1	100
$\tau \to e$	93 ± 1	93 ± 1	100

Table 14: Summary of the track follow-down efficiencies for different τ decay modes, topologies (long and short) and type of events (DIS and QE).

2.13 DETECTION EFFICIENCY

For a given channel the overall detection efficiency for the selection i can be schematically written as:

$$\epsilon_{TOT} = \epsilon_{trigger} \times \epsilon_{ED} \times \epsilon_{OpCarac} \times \epsilon_{BF_i} \times \epsilon_{CS} \times \epsilon_{SB} \times \epsilon_{LOC} \times \epsilon_{DS} \times \epsilon_{KIN} \times \epsilon_{TFD},$$

where the only step depending on the adopted selection is the brick identification.
By multiplying all factors, the efficiencies for the two different selections have been evaluated. Results are reported in Tables 15 and 16.
Due to the less favourable signal to noise ratio, short decays for $\tau \to h$ decay channel are not used for in the τ search.

ϵ_{TOT}(%) - SELECTION A -			
	LONG DIS	SHORT DIS	LONG QE
$\tau \to h$	11.4 ± 0.8	(7.0 ± 0.8)	1.5 ± 0.2
$\tau \to 3h$	12.8 ± 0.6	8.9 ± 0.6	5.1 ± 0.2
$\tau \to \mu$	23.4 ± 0.8	9.4 ± 0.8	13.1 ± 0.2
$\tau \to e$	13.5 ± 0.5	9.8 ± 0.5	0.5 ± 0.1

Table 15: Summary of the τ detection efficiency for different τ decay modes, topologies (long and short) and type of events (DIS and QE). Hadronic short decay efficiencies (in bracket) are not taken into account.

ϵ_{TOT}(%) - SELECTION B -			
	LONG DIS	SHORT DIS	LONG QE
$\tau \to h$	8.9 ± 0.8	(5.5 ± 0.8)	1.2 ± 0.2
$\tau \to 3h$	10.1 ± 0.6	7.0 ± 0.6	3.9 ± 0.2
$\tau \to \mu$	18.6 ± 0.8	7.7 ± 0.8	8.6 ± 0.2
$\tau \to e$	10.6 ± 0.5	7.5 ± 0.5	0.3 ± 0.1

Table 16: Summary of the τ detection efficiency for different τ decay modes, topologies (long and short) and type of events (DIS and QE). Hadronic short decay efficiencies (in bracket) are not taken into account for the significance evaluation.

3 ν_τ CANDIDATES

3.1 SEARCH FOR ν_τ CANDIDATES IN DATA

The search for $\nu_\mu \rightarrow \nu_\tau$ oscillations in the OPERA experiments has been performed with different strategies.
In the first two years of run (2008-2009) all the neutrino interactions occurring in the detector have been analyzed. Despite a lower analysis speed, this conservative approach was adopted in order to get confidence on the detector performances before applying any kinematical cut. From the analysis of all the data sample, 505 0μ and 2268 1μ events went through all the analysis steps, including the decay search. One event in the 0μ sample passed all the selections to be a ν_τ candidate in the $\tau \rightarrow h$ decay channel.
Since a good agreement between data and Monte Carlo simulation was achieved, starting from the 2010 run, a cut on the muon momentum $p_\mu < 15$ GeV/c for 1μ events was applied. This cut does not affect the τ signal since it corresponds to the kinematical cut applied to $\tau \rightarrow \mu$ candidates (as described in Section 2.11.3).
In order to further speed up the analysis in view of 2012 Summer conferences, the priority was given to 0μ events and only the most probable brick was analysed for each event. The analysis of the second brick increases the efficiency by less than 50 % but doubles the analysis time. This is the reason why it was postponed.
From the analysis of this the data sample, 486 0μ (2010 and 2011 runs) and 818 1μ (2010 run) events went through all the analysis steps, including the decay search. One event in the 0μ sample passed all the selections to be a ν_τ candidate in the $\tau \rightarrow 3h$ decay channel.
After Summer 2012, the analysis was extended also to 1μ events of 2011 and 2012 and a third ν_τ candidate was found in the $\tau \rightarrow \mu$ decay channel.
The three candidates have been independently measured in a European and Japanese scanning laboratory. Measurements are consistent and their averages are considered in the following.

3.2 THE FIRST CANDIDATE: $\tau \to h$

The neutrino interaction that will be described in the following occurred on 22 August 2009 in a brick situated in the wall 11 of the first supermodule. Figures 36 and 37 show the electronic detector pictures of the event. No muon was identified by electronic detector reconstruction.
The scanning of the CS of the interaction brick was performed around the electronic detector prediction and five tracks were reconstructed. The result of the CS analysis is summarized in the display shown in Figure 38: the tracks found are shown as black arrows, where the application point is the position of their impact on the CS and the length is proportional to their slope. A converging pattern was found, satisfying the conditions for event validation, as described in the previous chapter. The corresponding brick was extracted and developed.

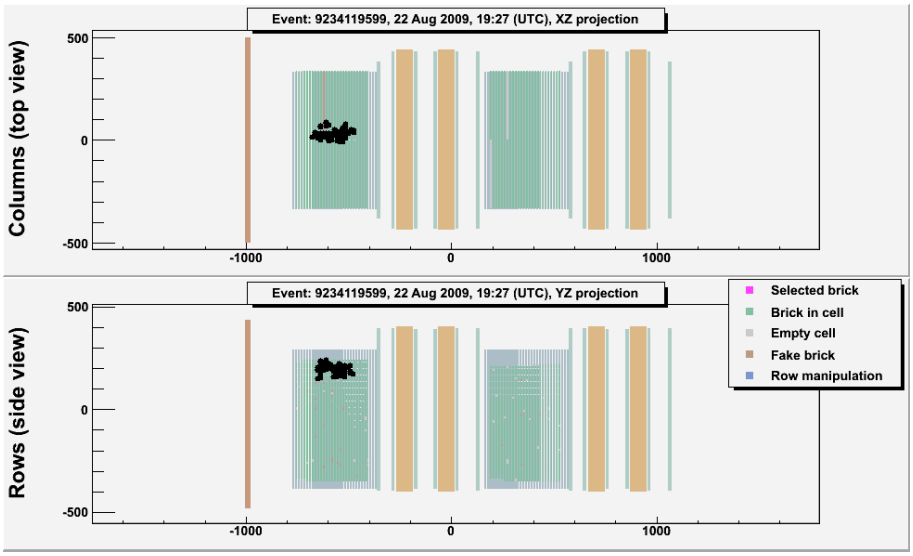

Figure 36: Electronic detector display of the first ν_τ candidate event

3.2.1 Topological event reconstruction

The CS tracks were followed in the brick with the scan-back procedure and a total-scan around their stopping point was performed. The neutrino interaction occurred in the lead plate between film 18 and 19, 6.5 X_0 far from the downstream edge of the brick.
The interaction has been fully reconstructed in the brick, looking for tracks within an angular acceptance of 1 rad. The complete picture of the event at the emulsion level is shown in Figures 39 and 40.

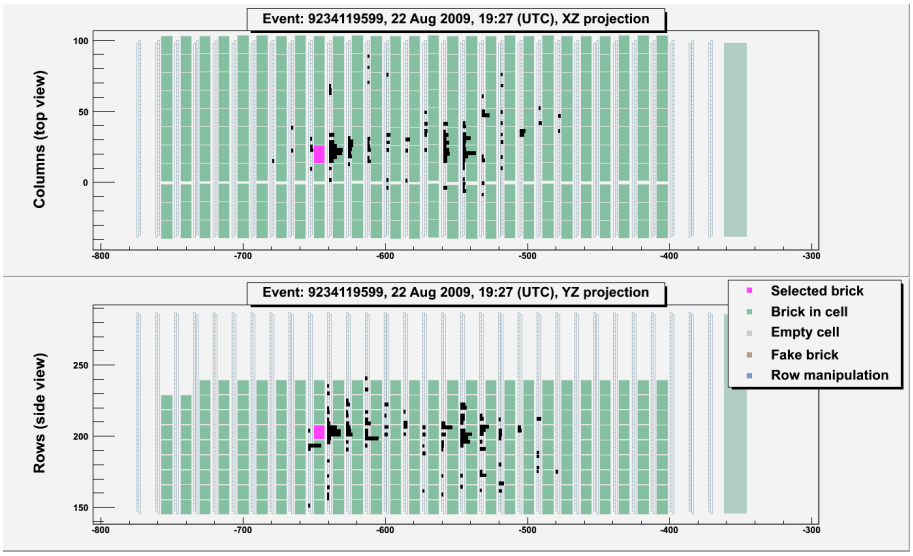

Figure 37: Electronic detector display of the first ν_τ candidate event: zoom on the interaction region. The brick containing the interaction is highlighted.

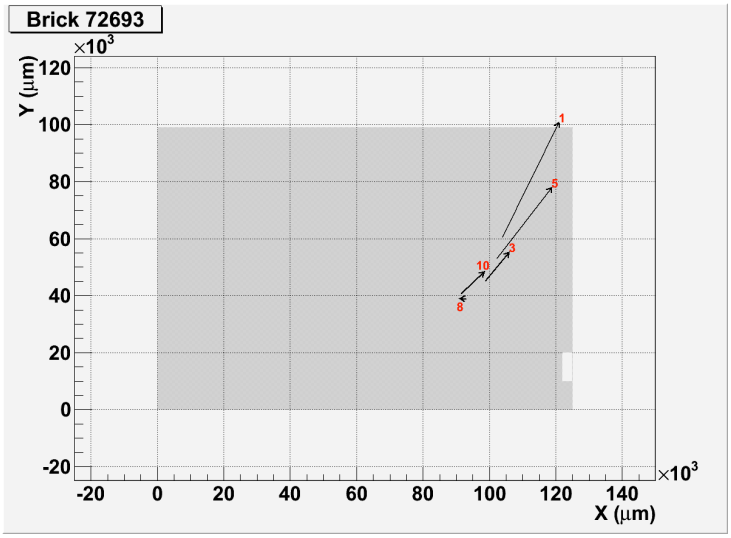

Figure 38: Display of the tracks found in the analysis of the CS related to the first ν_τ candidate interaction brick.

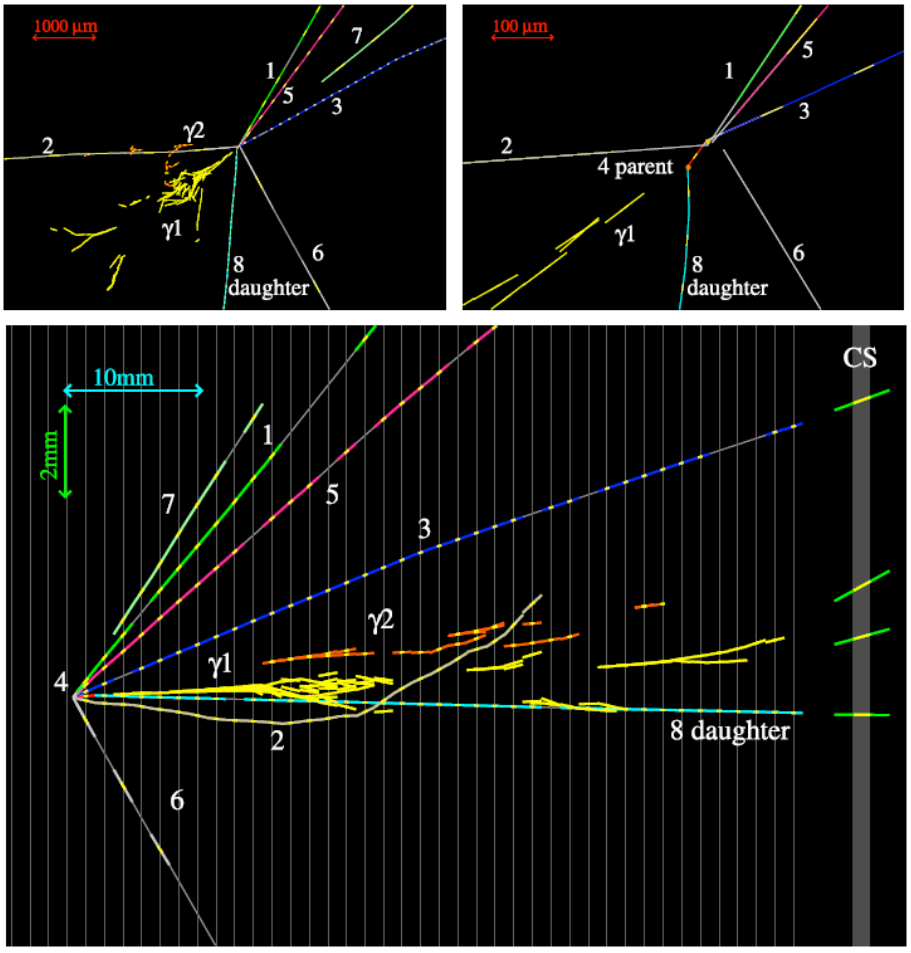

Figure 39: Display of the first ν_τ candidate event, as reconstructed in the emulsion films. Top left: view transverse to the neutrino direction. Top right: zoomed on the vertices for the same view. Bottom: longitudinal view.

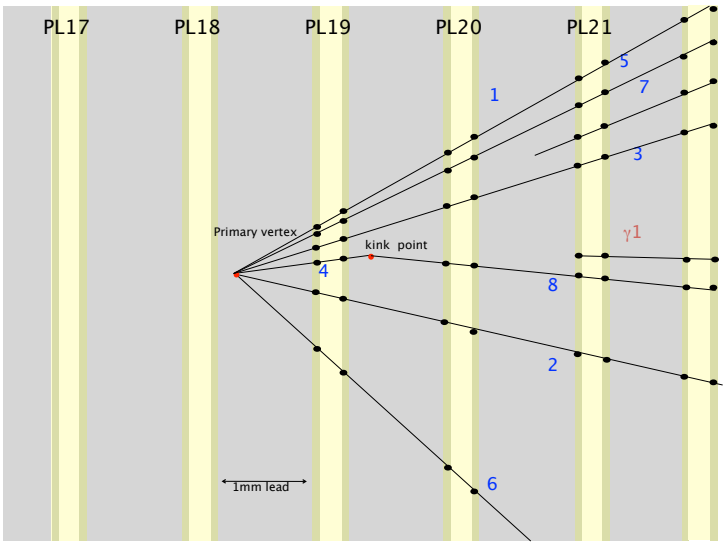

Figure 40: Schematic picture of the first ν_τ candidate event. Zoom on the primary and secondary vertices. Tracks 1, 2, 3, 4, 5, 6 and 7 come from the primary vertex; track 4 is the τ candidate decaying in the lead plate between film 19 and film 20, track 8 is the decay daughter. The starting point of the shower originating from γ_1 is also visible in the film 21.

The primary neutrino interaction consists of 7 tracks of which one exhibits a visible kink. Two electromagnetic showers caused by γ-rays have been located. In detail:

Track 1 found on CS and attached to the primary vertex. It exits from the primary interaction brick. Being not found in the brick immediately downstream, it undergoes the range-momentum correlation study. The variable associated to the track follow-down (see Section 2.12) has been evaluated: the measured value of D_{TFD} =0.1 allows to identify the track as a hadron;

Track 2 high ionizing particle, attached to primary vertex and stopping inside the brick. From its residual range (32.0±0.5) g·cm^{-2} and the value of pβ= $(0.32^{+0.31}_{-0.11})$ GeV/c measured on the upstream half of the track, the particle is identified as a proton, the kaon hypothesis being rejected with a C.L. of 97%;

Track 3 found on CS and attached to the primary vertex, it generates a two-prong interaction four bricks downstream of the primary vertex;

Track 4 exhibits a kink topology with θ_{kink} = 41±2 mrad after a path length of 1335±35 μm;

Track 5 found on CS and attached to the primary vertex. It has been followed in wall 12 (one wall downstream) and disappears in wall 13 after a total distance of 174 g·cm^{-2}. It is classified as a hadron, having D_{TFD} =0.27;

Track 6 stopping inside the brick and attached to primary vertex. It is classified as a hadron, having D_{TFD} =0.15;

Track 7 not directly attached to the primary vertex, pointing to it with an impact parameter of 43^{+45}_{-43} µm. Its origin is likely to be a prompt neutral particle and it stops in the interaction brick;

Track 8 the kink daughter, found on CS level and not directly attached to the primary vertex, pointing to it with an impact parameter of 55±4 µm. It generates a 2-prong interaction seven walls downstream its emission vertex;

Shower 1 originating from γ_1, starts 2.2 mm from the secondary vertex and it is compatible with pointing to it with a probability of 32%, the impact parameter being 7.5±4.3 µm. Its probability to be attached to the primary vertex is less than 10^{-3}, the impact parameter being 45.0±7.7 µm. Track 10 coming from the CS was associated to the last part of this electromagnetic shower;

Shower 2 originating from γ_2 is compatible with pointing to either vertex, with a significantly larger probability of 82% at the secondary vertex, the impact parameter being 22^{+25}_{-22} µm, compared to 10% probability and 85±38 µm IP at the primary vertex. Its distance from both vertices is about 13 mm.

None of the charged particles emitted at either vertex is compatible with being that of an electron. The application of track follow-down allowed to classify all the tracks as hadrons: the complete picture is shown in Figure 56.
A scanning with an angular acceptance up to tan(θ) =3 has also been performed and no additional track was found.

3.2.2 Kinematical analysis

The momentum of charged particles can be determined from the angular deviations produced by Multiple Coulomb Scattering (MCS) of tracks in the lead plates [76]. This method gives a momentum resolution better than 22% for charged particles with momenta lower than 6 GeV/c, passing through the entire brick and 10% if lower than 4 GeV/c. For higher momentum particles, the momentum is based on

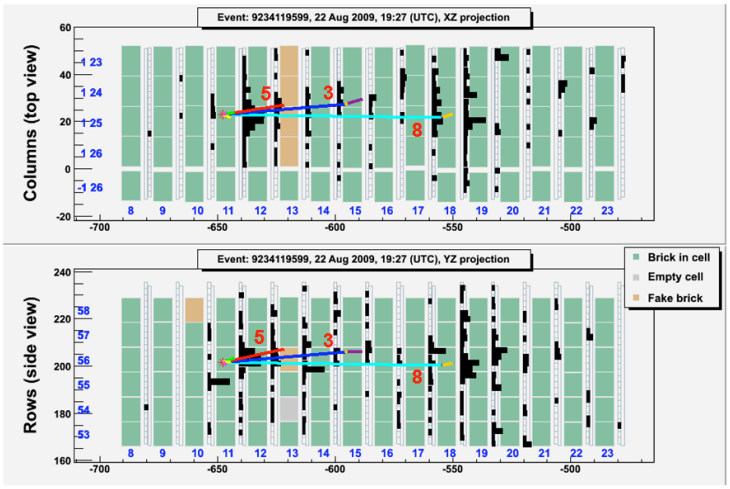

Figure 41: Electronic detector display of the first candidate event with all penetrating tracks superimposed, down to their stopping or re-interaction point.

the position deviations. The resolution is better than 33% on $1/p$ up to 12 GeV/c for particles passing through the entire brick.
The γ-ray energy is estimated by a Neural Network algorithm that uses the combination of the number of segments, the shape of the electromagnetic shower and the Multiple Coulomb Scattering of the tracks.
The measured values of the particles' momenta and of the showers' energy are reported in Table 17.
The transverse momentum at the secondary vertex (P_T) was computed by considering the most probable configuration where both showers (γ_1 and γ_2) are emitted at the secondary vertex. The measured value is P_t=470$^{+240}_{-120}$ MeV/c. The missing transverse momentum at the primary vertex is P_T^{miss} =570$^{+320}_{-170}$ MeV/c.
Since all the tracks at the primary have been identified as hadrons, no track is the discarded for the ϕ_{mod} evaluation. Its value is $(173\pm2)^\circ$.
The sum of the modulus of the momenta of all the particles in the event is $24.3^{+6.1}_{-3.2}$ GeV/c.
The invariant mass of γ_1 and γ_2 is $120\pm20(stat.)\pm35(syst.)$ MeV/c^2, supporting the hypothesis that they originate from a π^0 decay. Similarly the invariant mass of the charged decay product assumed to be a π^- and of the two γ-rays amounts to $640^{+125}_{-80}(stat.)^{+100}_{-90}(syst.)$ MeV/c^2, which is compatible with the $\rho(770)$ mass. The branching ratio of the decay mode $\tau^- \to \rho^-\nu_\tau$ is about 25%.
In Table 18 the value of the decay topological and kinematical quantities computed for this event are reported with the selection criteria defined for the $\tau \to h$ channel. All variables considered pass the se-

Charged track	Momentum (GeV/c)
Track 1	$0.78^{+0.13}_{-0.10}$
Track 2	0.60 ± 0.05
Track 3	$1.97^{+0.33}_{-0.25}$
Track 5	$1.30^{+0.22}_{-0.16}$
Track 6	$0.36^{+0.18}_{-0.09}$
Track 7	$0.49^{+0.29}_{-0.13}$
Track 8	12^{+6}_{-3}
Shower	**Energy (GeV)**
γ_1	$5.6 \pm 1.0(stat.) \pm 1.8(syst.)$
γ_2	$1.2 \pm 0.4(stat.) \pm 0.4(syst.)$

Table 17: Momentum of charged tracks and energy of the showers for the first ν_τ candidate.

lection cuts required to select a tau candidate, as shown in Figure 42.

Variable	Selection ($\tau \to h$)	Measurement
θ_{kink} (mrad)	> 20	41 ± 2
Δz (μm)	< 2600	435 ± 35
$P_{daughter}$ (GeV/c)	> 2	12^{+6}_{-3}
P_T (MeV/c)	> 300 (γ attached)	470^{+230}_{-120}
P_T^{miss} (MeV/c)	< 1000	570^{+320}_{-170}
$\phi_{mod}(^\circ)$	> 90	173 ± 2

Table 18: Selection criteria for ν_τ candidate events in the $\tau \to h$ decay channel and corresponding measured values for the first observed candidate.

3.3 THE SECOND CANDIDATE: $\tau \to 3h$

The neutrino interaction occurred on 23 April 2011 in a brick situated in the wall 4 of the first supermodule. Figures 43 and 44 show the electronic detector displays of the event. As for the first candidate, no muon track was reconstructed by electronic detectors.
The electronic detector prediction was used to define the area to be

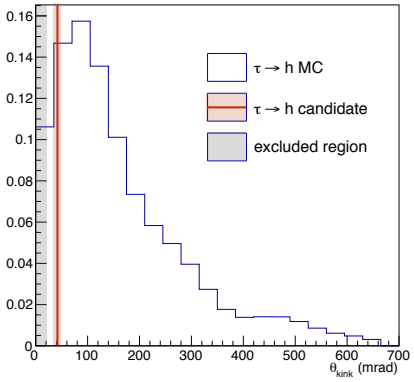

(a) Kink angle

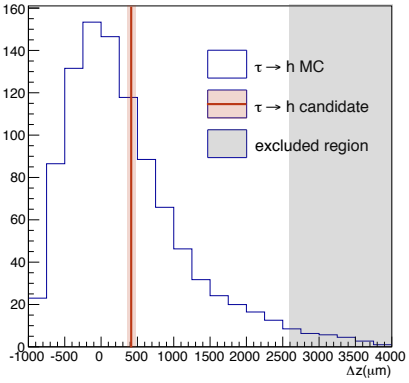

(b) Δz

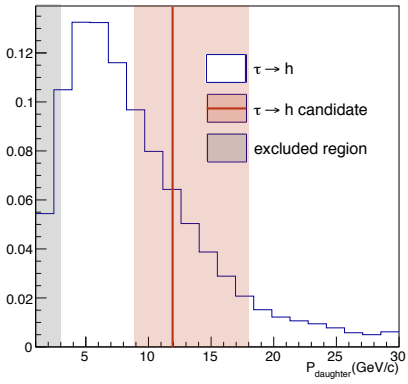

(c) Daughter momentum

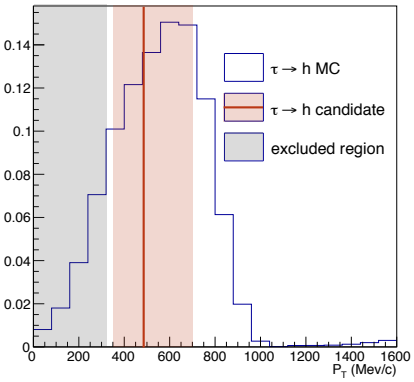

(d) Transverse momentum

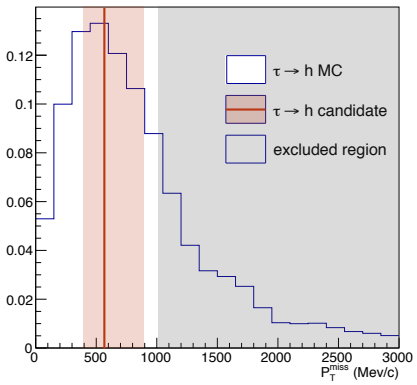

(e) Missing momentum

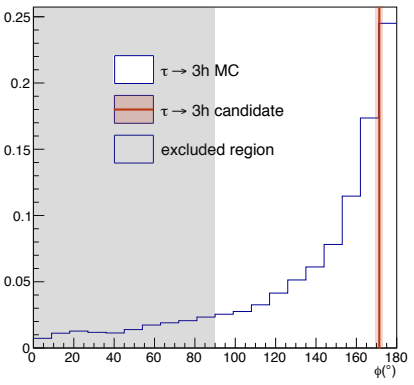

(f) ϕ_{mod}

Figure 42: Monte Carlo distribution of the kinematical variables for the $\tau \to h$ decay channel. Red bands show the measured value and its error, the grey area represents the excluded region corresponding to the selection cut.

scanned on the CS: three converging tracks were reconstructed, as shown in Figure 45. The corresponding brick was extracted and developed.

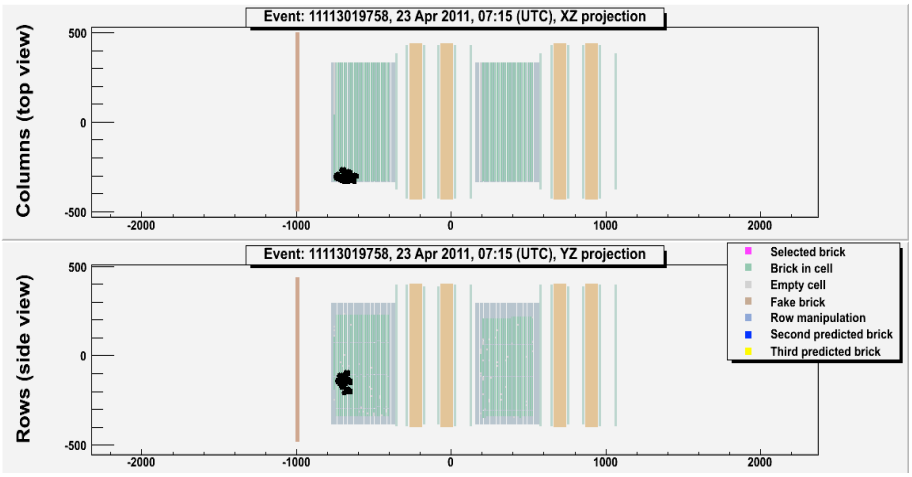

Figure 43: Electronic detector display of the second ν_τ candidate event

3.3.1 Topological event reconstruction

The scan-back procedure was applied to the tracks found on CS and the scanning of a volume around their stopping point was performed. The neutrino interaction occurred in the lead plate between film 22 and film 23, 6.1 X_0 far from the downstream edge of the brick.
The complete picture of the event at the emulsion level is shown in Figure 46.
The primary vertex consists of 2 tracks: the τ lepton candidate and an hadronic track. A nuclear fragment associated to the primary vertex has also been detected with an impact parameter of $15\mu m$. The τ lepton decay occurs in the plastic base, as can be seen in Figure 47. This reduce by more than one order of magnitude the probability of hadronic interactions. Moreover highly ionizing nuclear fragments can be seen with higher efficiency if the interaction vertex is in the plastic base.
The secondary vertex generated by the τ decay consists of three charged tracks.
The details about the reconstructed tracks are reported in the following:

Track 1 found on CS and attached to the primary vertex. It has been followed in the downstream wall where it is found to exit from

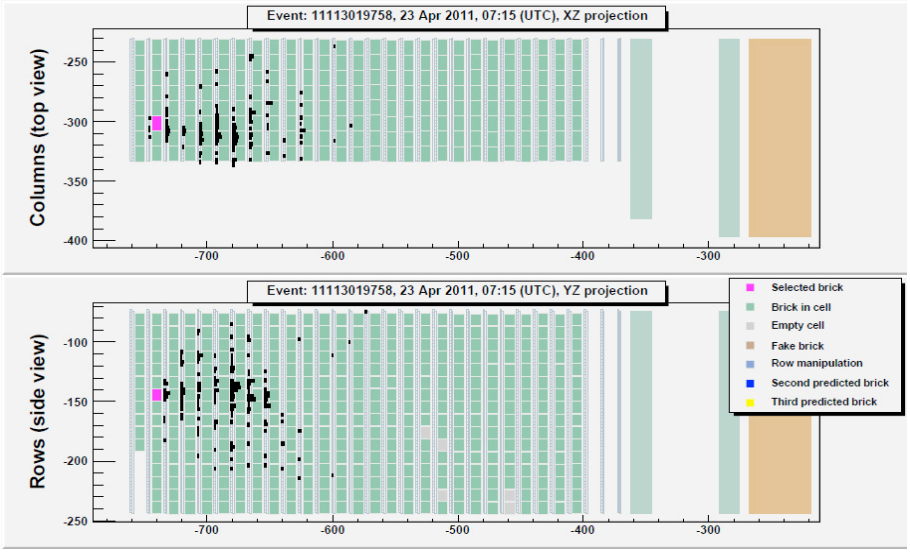

Figure 44: Electronic detector display of the second ν_τ candidate event: zoom on the interaction region. The brick containing the interaction is highlighted.

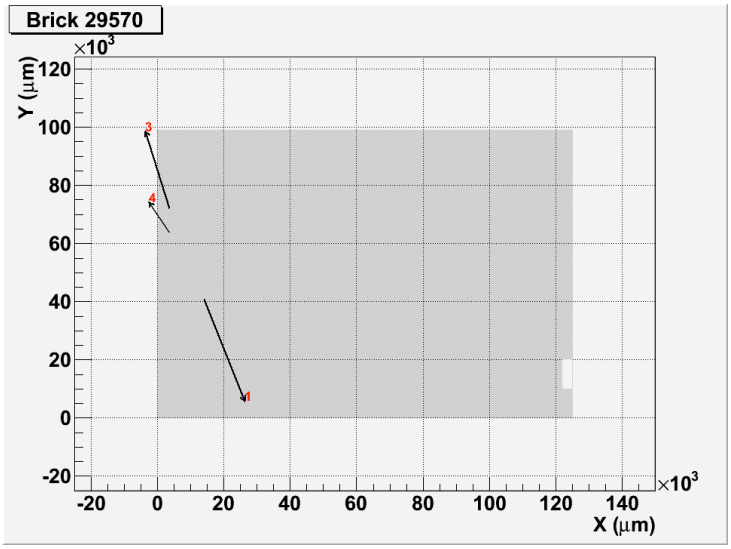

Figure 45: Display of the tracks found in the analysis of the CS related to the second ν_τ candidate interaction brick.

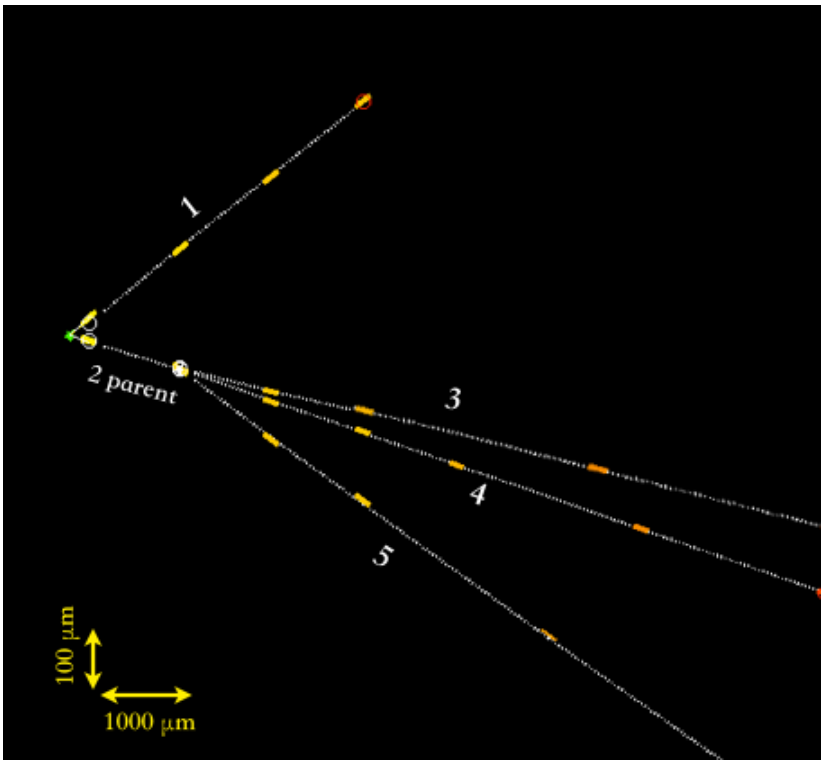

Figure 46: Display of the second ν_τ candidate event, as reconstructed in the emulsion films.

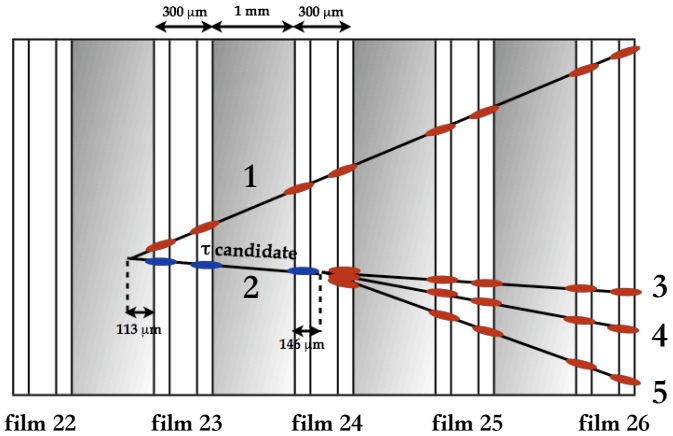

Figure 47: Schematic picture of the second ν_τ candidate event. Zoom on the primary and secondary vertices. Tracks 1, 2 come from the primary vertex; track 2 is the τ candidate decaying in the plastic base of film 24, tracks 3,4 and 5 are the decay daughters.

the brick side. Being not found in the adjacent brick, it undergoes the range-momentum correlation study. It is classified as a hadron, having D_{TFD} =0.05;

Track 2 τ candidate. It exhibits a decay topology in three prongs after a path length of 1559 ± 10 μm;

Track 3 τ decay daughter, with a kink angle of 46 mrad and an impact parameter of 70± 5 μm w.r.t. the primary vertex. Found on the CS it generates a two-prong interaction four bricks downstream of the primary;

Track 4 τ decay daughter, with a kink angle of 111 mrad and an impact parameter of 61± 5 μm w.r.t. the primary vertex. Found on the CS it stops two walls downstream, with D_{TFD} =0.25 and it is therefore identified as an hadron;

Track 5 τ decay daughter, with a kink angle of 115 mrad and an impact parameter of 170± 5 μm w.r.t. the primary vertex. It interacts in the same brick containing the neutrino vertex, after 11 lead plates i.e. about 1.3 cm downstream. The interaction occurs inside the emulsion allowing an extremely clear signature. The final state is composed of two charged tracks and four backscattered nuclear fragments.

The application of track follow-down allowed to classify all the tracks as hadrons.
A systematic search for γ conversions has been performed by doing a general search in the emulsions up to an angle of $\tan(\theta)$ =1 in the vertex brick for the 35 downstream plates yielding no candidates. A scanning with an angular acceptance up to $\tan(\theta)$ =3 has also been performed and no additional track was found attached to the primary vertex.

3.3.2 Kinematical analysis

The momenta of the particles have been measured and the results are reported in Table 19.
The average kink angle of the three daughters is $\langle \theta_{kink} \rangle$ = 87.4 ± 1.5 mrad while the sum of the momenta at secondary vertex is $P_{daughters}$ = 8.4 ± 1.7. The missing transverse momentum at the primary vertex is P_T^{miss} =310±110 MeV/c.
Since all the tracks at the primary have been identified as hadrons, no track is the discarded for the ϕ_{mod} evaluation. Its value is (167.8±1.1)°.
The invariant mass of the three daughters is M =0.80± 0.12 GeV/c^2

Charged track	Momentum (GeV/c)
Track 1	$2.8^{+0.7}_{-0.7}$
Track 3	$6.6^{+2.0}_{-1.4}$
Track 4	$1.3^{+0.2}_{-0.2}$
Track 5	$2.0^{+0.9}_{-0.6}$

Table 19: Momentum of charged tracks for the second ν_τ candidate.

and the minimum invariant mass M_{min} =0.93±0.13 GeV/c^2.
The sum of the modulus of the momenta of all the particles in the event is $12.7^{+2.3}_{-1.7}$ GeV/c.
In Table 20 the value of the decay topological and kinematical quantities computed for this event are reported with the selection criteria defined for the $\tau \to 3h$ channel. All variables considered pass the selection cuts required to select a tau candidate, as shown in Figure 48.

Variable	Selection ($\tau \to 3h$)	Measurement
$\langle\theta_{kink}\rangle$(mrad)	< 500	87.4 ± 1.5
Δz (μm)	< 2600	1446 ± 10
$P_{daughters}$ (GeV/c)	> 3	8.4 ± 1.7
P_T^{miss} (MeV/c)	< 1000	310 ± 110
$\phi_{mod}(^\circ)$	> 90	167.8 ± 1.1
M (GeV/c^2)	$[0.5 - 2]$	0.80 ± 0.12
M_{min} (GeV/c^2)	$[0.5 - 2]$	0.96 ± 0.13

Table 20: Selection criteria for ν_τ candidate events in the $\tau \to 3h$ decay channel and corresponding measured values for the second observed candidate.

3.4 THE THIRD CANDIDATE: $\tau \to \mu$

The neutrino interaction that will be described in the following occurred on 2 May 2012 in a brick situated in the wall 8 of the first supermodule. Figures 49 and 50 show the electronic detector pictures of the event. A muon track was reconstructed by electronic detectors.
The scanning of the CS of the interaction brick was performed around the electronic detector prediction and six tracks were reconstructed. The result of the CS analysis is summarized in the display shown in

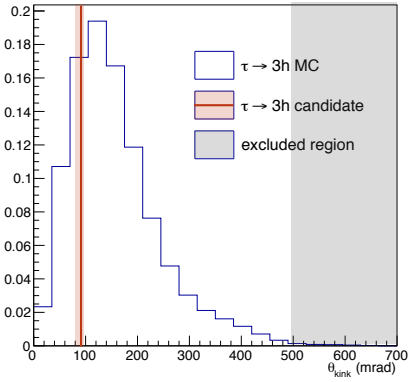

(a) Average Kink angle

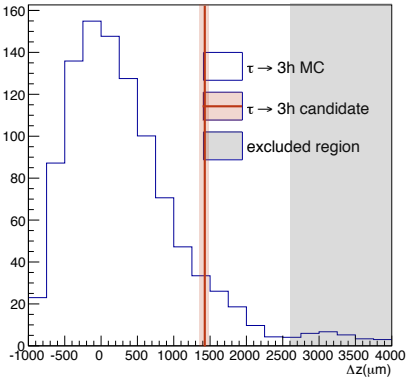

(b) Δz

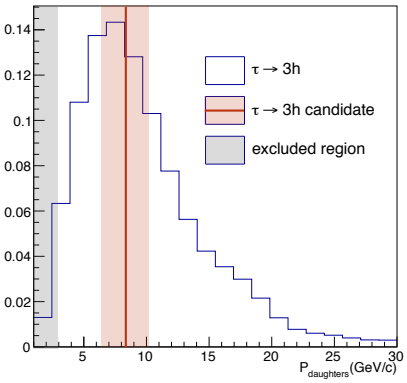

(c) Sum of daughter momenta

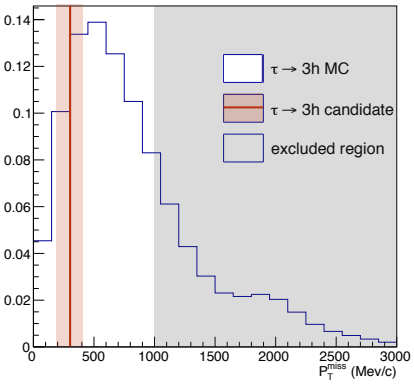

(d) Missing momentum

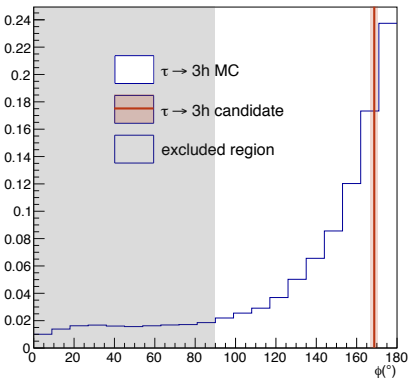

(e) ϕ_{mod} angle

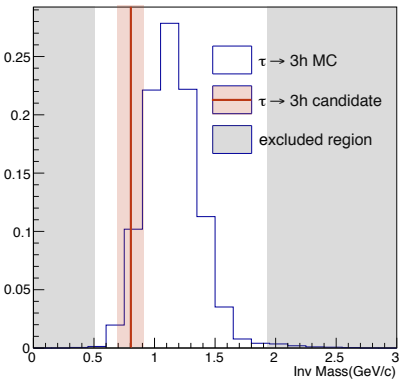

(f) Invariant mass

Figure 48: Monte Carlo distribution of the kinematical variables for the $\tau \to 3h$ decay channel. Red bands show the measured value and its error, the grey area represents the excluded region corresponding to the selection cut.

Figure 51: the muon track was found as well as a converging pattern, satisfying the conditions for event validation, as described in the previous chapter. The corresponding brick was extracted and developed.

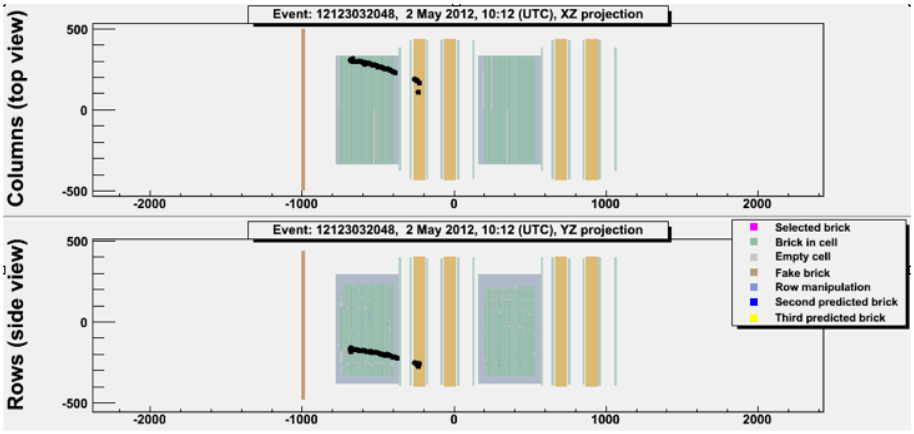

Figure 49: Electronic detector display of the third ν_τ candidate event

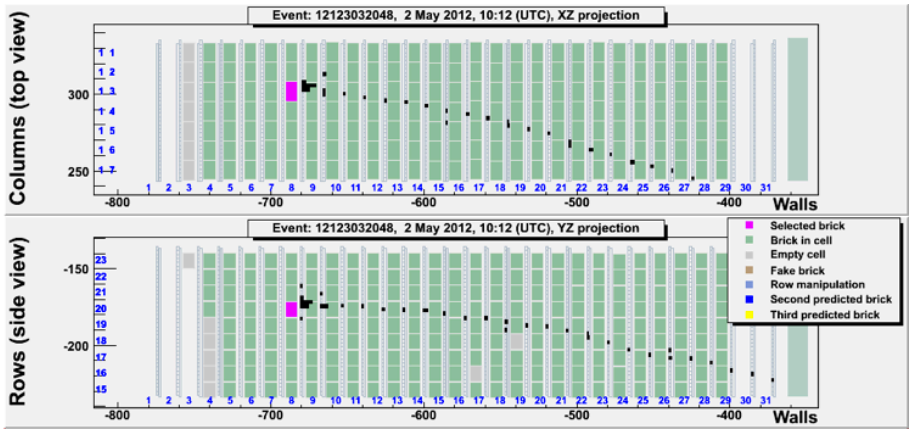

Figure 50: Electronic detector display of the third ν_τ candidate event: zoom on the interaction region. The brick containing the interaction is highlighted.

3.4.1 Muon momentum and charge measurement

The muon track stops in the first spectrometer, after having crossed 21 walls of the target and 6 iron slabs of the magnet (Figure 52).
The momentum has been estimated from the range of the particle in the detector. The measured value is $p_\mu = 2.8 \pm 0.2$. In order to perform an independent measurement, the brick immediately downstream of

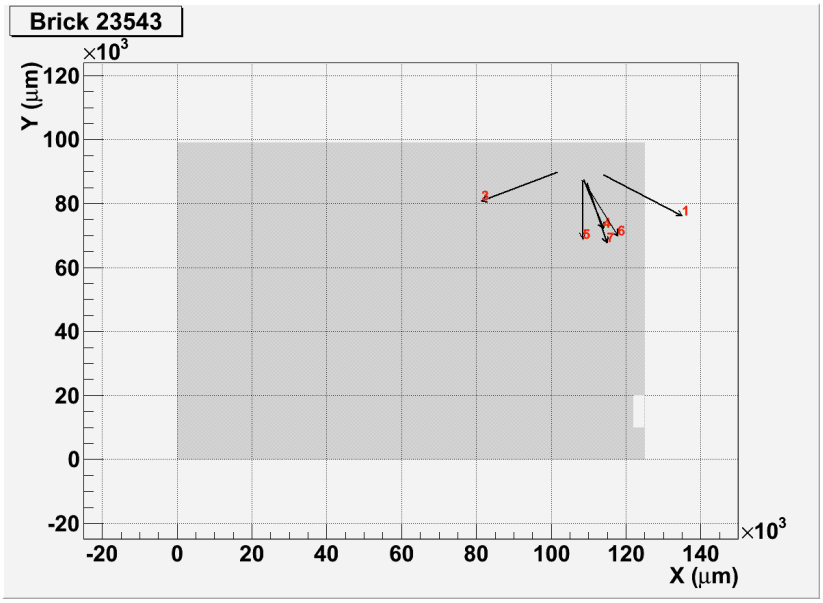

Figure 51: Display of the tracks found in the analysis of the CS related to the third ν_τ candidate interaction brick.

the one containing the neutrino interaction was extracted. The muon track was measured in all the emulsion films, allowing a momentum estimation with the Multiple Coulomb Scattering algorithm. The measured value $p_\mu^{MCS} = 3.1^{+0.9}_{-0.5}$ is compatible with the one estimated from the range.
The charge measurement is performed with the Target Tracker and RPC hits. A fit is performed (as shown in Figure 53) with a straight line in the not magnetized region (TT hits) and with a parabola in the magnetized region (RPC hits). The parabolic part is meant to approximate the circular trajectory. The fit gives a parabola with the concavity towards the bottom, corresponding to a radius of ~ 85 cm. Given the direction of the magnetic field this corresponds to a negative charge with a significance of 5.6σ.

3.4.2 Topological event reconstruction

CS tracks were followed in the brick with the scan-back procedure and the standard volume was analysed around their stopping point.
The neutrino interaction occurred in the lead plate between film 38 and film 39, 3.3 X_0 far from the downstream edge of the brick. The interaction has been fully reconstructed in the brick, looking for tracks within an angular acceptance of 1 rad.

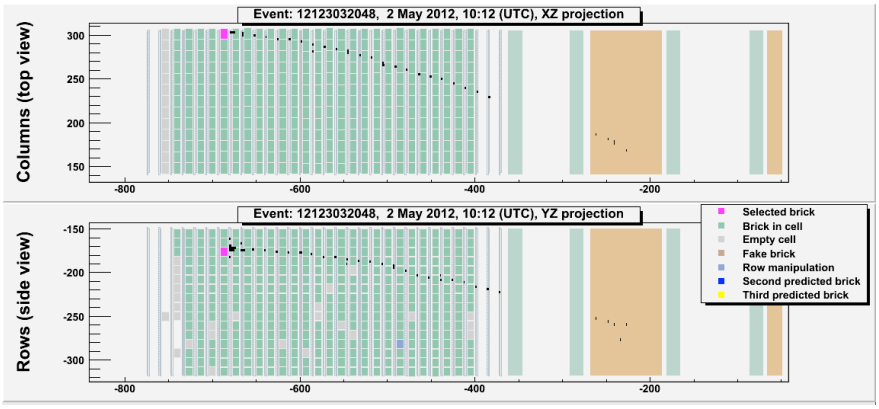

Figure 52: The muon track of the third ν_τ candidate crosses 21 walls of the target and stops in the first spectrometer.

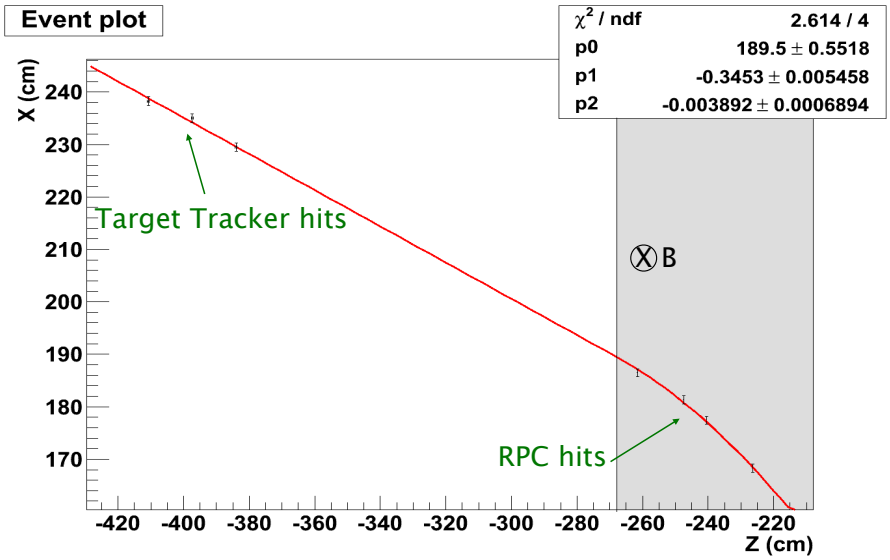

Figure 53: The Target Tracker and RPC hits are used to perform the muon charge measurement. A fit is performed with a straight line in the not magnetized region (TT hits) and with a parabola in the magnetized region (RPC hits).

The primary vertex consists of 2 tracks: the τ lepton candidate and an hadronic track. the τ lepton decays in plastic base of the first film immediately downstream of the primary vertex.
The complete picture of the event at the emulsion level is shown in Figures 54 and 55.

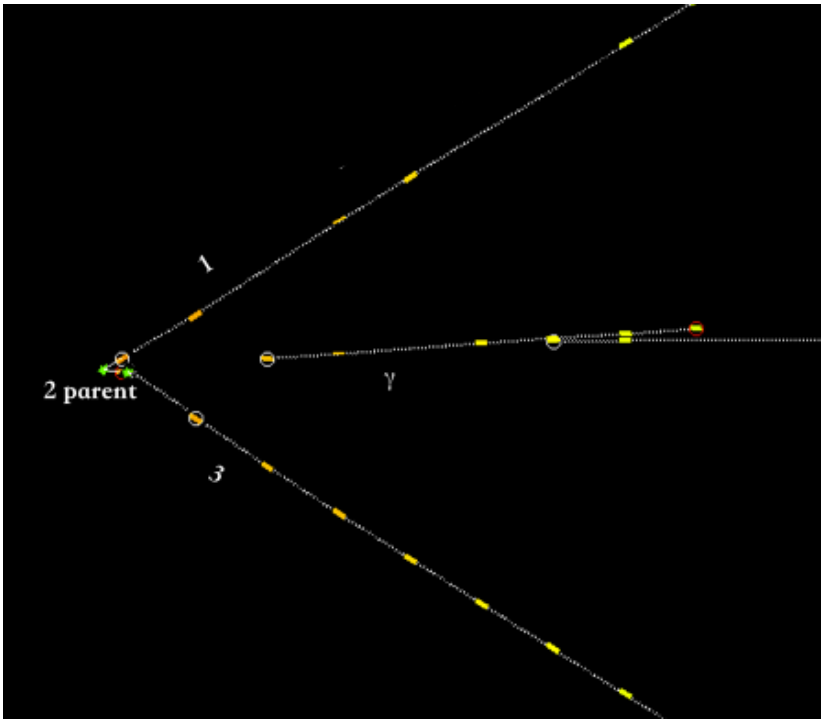

Figure 54: Display of the third ν_τ candidate event.

The primary vertex consists of 2 tracks: the τ lepton candidate and an hadronic track. The τ lepton decay occurs in the plastic base of the plate immediately downstream of the primary vertex. The decay particle is compatible with the muon track reconstructed in the electronic detectors.
The details about the reconstructed tracks are reported in the following:

Track 1 found on CS and attached to the primary vertex. It has been followed in the downstream wall where its interaction was reconstructed. It is classified as a hadron, having D_{TFD} =0.1;

Track 2 τ candidate. It exhibits a decay topology in one prong after a path length of 376±10 μm;

Track 3 τ decay daughter, with a kink angle of 245±5 mrad and an impact parameter of 77±5 μm w.r.t. the primary vertex. Found

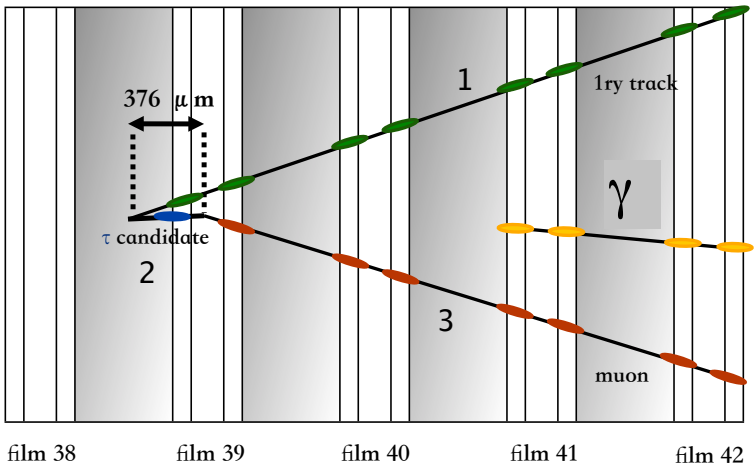

Figure 55: Schematic picture of the third ν_τ candidate event. Zoom on the primary and secondary vertices. Tracks 1 and 1 come from the primary vertex; track 2 is the τ candidate decaying in the plastic base of film 39, track 3 is the muon decay daughter. The starting point of the shower generated from γ is visible in film 41.

on the CS, it is in agreement with the muon track reconstructed in the electronic detectors;

Shower originating from γ, starts 2.1 mm from the primary vertex and it is compatible with pointing to it with an the impact parameter being 18 ± 13 μm. Its probability to be attached to the secondary vertex is less than 10^{-3}, the impact parameter being 69 ± 12 μm.

The application of track follow-down allowed to classify all the tracks as hadrons. The complete picture is shown in Figure 56.

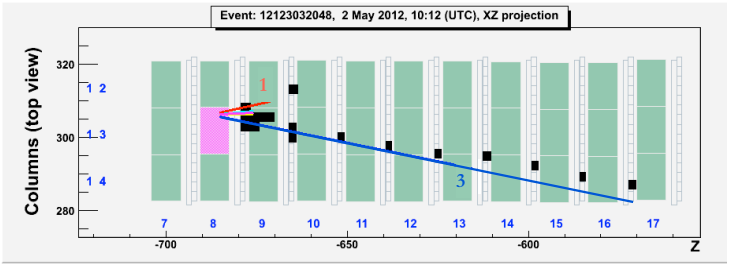

Figure 56: Electronic detector display of the third candidate event with all penetrating tracks superimposed. The re-interaction point of the track 1 is visible.

A scanning with an angular acceptance up to $\tan(\theta) = 3$ has also been performed and no additional track was found.

3.4.3 Kinematical analysis

The measured values of the particles' momenta and of the showers' energy are reported in Table 21.

Charged track	Momentum (GeV/c)
Track 1	0.9 ± 0.2
Track 3	2.8 ± 0.2
Shower	Energy (GeV)
γ	2.9 ± 0.3

Table 21: Momentum of charged tracks and energy of the shower for the first ν_τ candidate.

The transverse momentum at the secondary vertex (p_T) is 690 ± 50 MeV/c. The muon momentum has been estimated from its range in the detector $P_\mu = 2.8 \pm 0.2$ GeV/c.
The sum of the modulus of the momenta of all the particles in the event is 6.6±0.4 GeV/c.
In Table 22 the value of the decay topological and kinematical quantities computed for this event are reported with the selection criteria defined for the $\tau \to \mu$ channel. All variables considered pass the selection cuts required to select a tau candidate, as shown in Figure 57.

Variable	Selection ($\tau \to \mu$)	Measurement
$\langle \theta_{kink} \rangle$(mrad)	< 500	245 ± 5
Δz (μm)	< 2600	151 ± 10
P_μ (GeV/c)	$[1 - 15]$	2.8 ± 0.2
p_T (MeV/c)	> 250	690 ± 50

Table 22: Selection criteria for ν_τ candidate events in the $\tau \to \mu$ decay channel and corresponding measured values for the third observed candidate.

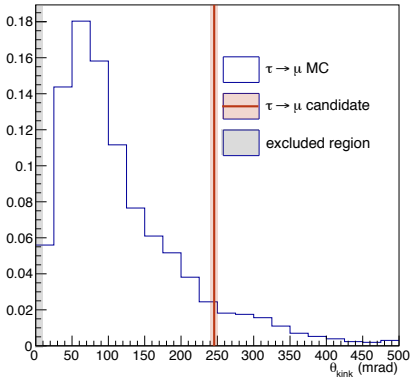

(a) Kink angle

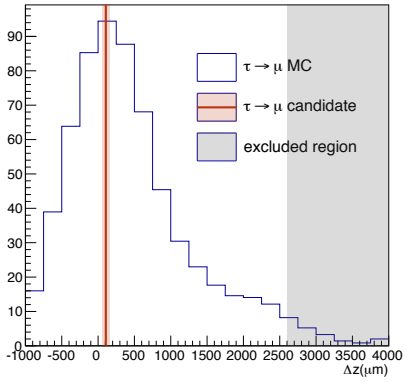

(b) Δz

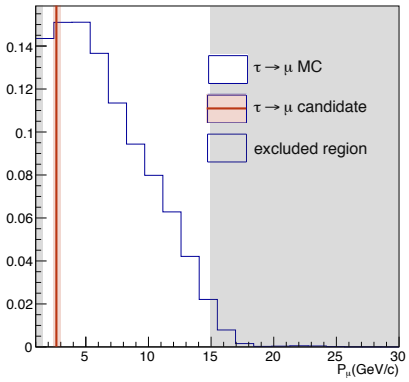

(c) Daughter momentum

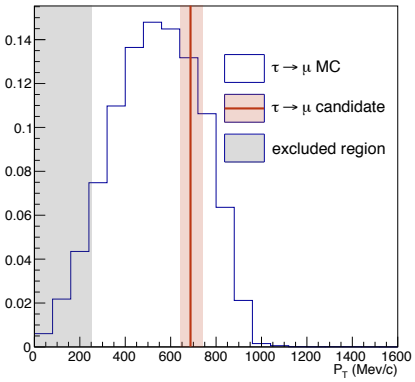

(d) Transverse momentum

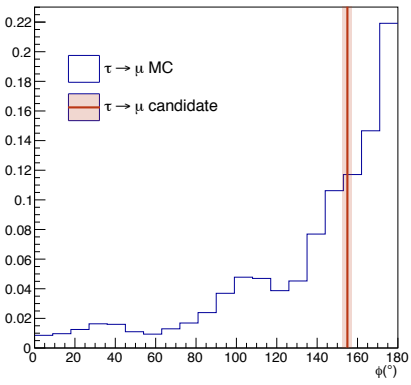

(e) ϕ_{mod}

Figure 57: Monte Carlo distribution of the kinematical variables for the $\tau \to \mu$ decay channel. Red bands show the measured value and its error, the grey area represents the excluded region corresponding to the selection cut.

4 PHYSICS PERFORMANCES

4.1 SIGNAL EXPECTATION

The number of expected τ can be expressed as:

$$\begin{aligned} N^{\tau}_{exp} &= 10^{9} M N_A L \langle \epsilon \rangle \int \Phi(E) \sigma_{\tau}(E) P_{\nu_\mu \to \nu_\tau}(E) dE, \\ &= ML \langle \epsilon \rangle N^{0}_{\tau}. \end{aligned} \tag{19}$$

where

- M is the mass of the detector (in units of kton)
- L is the value of integrated p.o.t. (in units of 10^{19})
- N_A is the Avogadro number
- $\Phi(E)$ is the ν_μ flux (in units of $cm^{-2} \times (10^{19} p.o.t).^{-1}$)
- and $\langle \epsilon \rangle$ the average location efficiency for ν_τ interactions

$$\langle \epsilon \rangle = \frac{\int \Phi(E) \sigma_{\tau} P_{\nu_\mu \to \nu_\tau} \epsilon(E) dE}{\int \Phi(E) \sigma_{\tau} P_{\nu_\mu \to \nu_\tau} dE} \tag{20}$$

Consequently, N^{0}_{τ} is the number of ν_τ interactions per kton and per 10^{19} p.o.t.
We can define $N^{0}_{\nu_\mu CC}$ ($N^{0}_{\nu_\mu NC}$) as the number of $\nu_{\mu CC}$ ($\nu_{\mu NC}$) interactions per kton and per 10^{19} p.o.t.

$$N^{0}_{\nu_\mu CC} = \int \Phi(E) \sigma_{\nu_{\mu CC}}(E) dE \quad \left(N^{0}_{\nu_\mu NC} = \int \Phi(E) \sigma_{\nu_{\mu NC}}(E) dE \right). \tag{21}$$

The number of events localized in the 0μ channel ($N^{0\mu}_{obs}$) can be expressed as the sum of NC events classified as 0μ ($N^{0\mu}_{obs}(NC)$) and CC events classified as 0μ ($N^{0\mu}_{obs}(CC)$):

$$\begin{aligned} N^{0\mu}_{obs} &= N^{0\mu}_{obs}(CC) + N^{0\mu}_{obs}(NC) \\ &= ML \int \Phi(E) \left(\sigma_{\nu_{\mu CC}} \epsilon^{0\mu}_{CC} + \sigma_{\nu_{\mu NC}} \epsilon^{0\mu}_{NC} \right) dE \\ &= ML \left(\langle \epsilon^{0\mu}_{CC} \rangle N^{0}_{\nu_{\mu CC}} + \langle \epsilon^{0\mu}_{NC} \rangle N^{0}_{\nu_{\mu NC}} \right) \\ &= MLN^{0}_{\nu_{\mu CC}} \left(\langle \epsilon^{0\mu}_{CC} \rangle + \alpha \langle \epsilon^{0\mu}_{NC} \rangle \right) \end{aligned} \tag{22}$$

where $\alpha = N^0_{\nu_{\mu NC}}/N^0_{\nu_{\mu CC}} \sim 0.32$.
It is then possible to write the normalization factor as

$$\begin{aligned} ML &= \frac{N^{0\mu}_{obs}}{N^0_{\nu_{\mu CC}}\left(\langle\epsilon^{0\mu}_{CC}\rangle + \alpha\langle\epsilon^{0\mu}_{NC}\rangle\right)} \\ &= \frac{\beta_0}{N^0_{\nu_{\mu CC}}} N^{0\mu}_{obs}, \end{aligned} \tag{23}$$

where $\beta_0 = 1/\left(\langle\epsilon^{0\mu}_{CC}\rangle + \alpha\langle\epsilon^{0\mu}_{NC}\rangle\right) = 7.5 \pm 1.1$ is evaluated from Monte Carlo simulations.
$\langle\epsilon^{0\mu}_{CC}\rangle$ and $\langle\epsilon^{0\mu}_{NC}\rangle$ are, respectively, the average location efficiencies of $\nu_{\mu CC}$ and $\nu_{\mu CC}$ events classified as 0μ.
The number of expected τ in the 0μ sample can be written as

$$\begin{aligned} N^{\tau}_{exp} &= \frac{N^{0\mu}_{obs}}{N^0_{\nu_{\mu CC}}\left(\langle\epsilon^{0\mu}_{CC}\rangle + \alpha\langle\epsilon^{0\mu}_{NC}\rangle\right)}\langle\epsilon\rangle N^0_{\tau} \\ &= \beta_0 N^{0\mu}_{obs}\langle\epsilon\rangle\frac{N^0_{\tau}}{N^0_{\nu_{\mu CC}}}. \end{aligned} \tag{24}$$

The number of expected τ in the decay channel $\tau \to i (i = h, 3h, e)$ is than:

$$N^{\tau\to i(0\mu)}_{exp} = \beta_0 N^{0\mu}_{obs}\langle\epsilon_{\tau\to i}\rangle\frac{N^0_{\tau}}{N^0_{\nu_{\mu CC}}} Br(\tau \to i), \tag{25}$$

where $\langle\epsilon_{\tau\to i}\rangle$ is the average efficiency for the particular decay channel.

Similarly, the number of expected τ in the decay channel $\tau \to \mu$ is:

$$N^{\tau\to\mu}_{exp} = \beta_1 N^{1\mu}_{obs}\langle\epsilon_{\tau\to\mu}\rangle\frac{N^0_{\tau}}{N^0_{\nu_{\mu CC}}} Br(\tau \to \mu), \tag{26}$$

where $\beta_1 = 1/\left(\langle\epsilon^{1\mu}_{CC}\rangle + \alpha\langle\epsilon^{1\mu}_{NC}\rangle\right) = 1.3 \pm 0.2$ is evaluated from Monte Carlo simulations.
$\langle\epsilon^{1\mu}_{CC}\rangle$ and $\langle\epsilon^{1\mu}_{NC}\rangle$ are, respectively, the average location efficiencies of $\nu_{\mu CC}$ and $\nu_{\mu NC}$ events classified as 1μ.
The average location efficiency are reported Tables 15 and 16 for the two different selections.
The expected number of events for the fraction of the runs analyzed so far is 2.22, divided in the different decay channels as reported in Table 23. For the total collected beam intensity of 17.97×10^{19} p.o.t., 4.30 signal event are expected. Full mixing and $\Delta m^2_{23} = 2.5\times10^{-3}\,eV^2$ are assumed.

	SIGNAL EXPECTED EVENTS
$\tau \to h$	0.66
$\tau \to 3h$	0.51
$\tau \to \mu$	0.56
$\tau \to e$	0.49
TOTAL	2.22

Table 23: Expected number of observed signal events in the different decay channels, for the data sample analyzed so far.

4.2 BACKGROUND EVALUATION

The background evaluation has been performed by means of a full Monte Carlo simulation. The main sources of background have been studied, depending on the decay channel.

4.2.1 Charm production and decay

The charm production is the main components of background in the ν_τ search, since the mass and the flight length of charmed hadrons are similar to the τ, so selection criteria have similar efficiencies to detect the decay topology. Charmed hadron production may constitute a background to ν_τ signal if the primary muon is not identified (Figure 58). In order to evaluate the background contamination from charm,

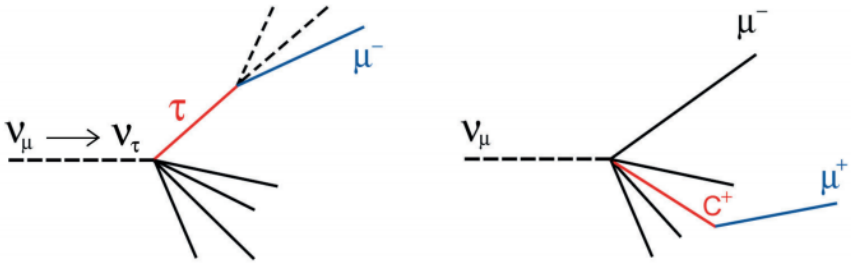

Figure 58: Decay topology of τ and charm.

ν_μCC interactions with charm production were simulated with the full Monte Carlo simulation. All the steps of the location chain were applied: from the electronic detector trigger to the decay search and the kinematical selection, as described in Chapter 2.

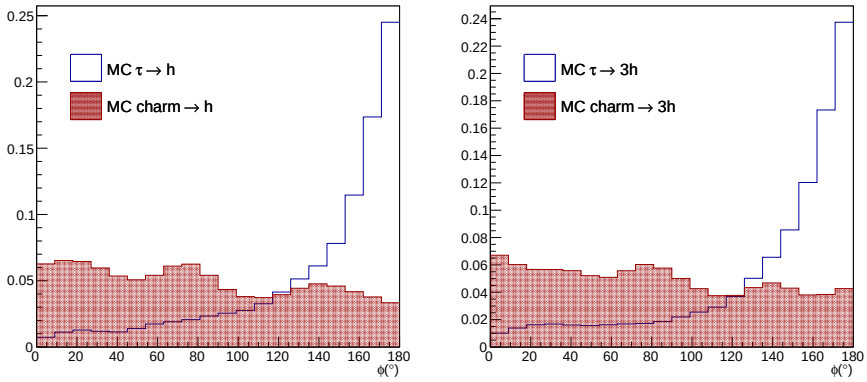

(a) $\tau \to h$ **(b)** $\tau \to 3h$

Figure 59: ϕ_{mod} angle distribution for signal (white area) and charm background (red shaded area). The straight line represents the selection cut.

The background in the $\tau \to h$ and $\tau \to 3h$ decay channels is made up of charm events where the primary muon is not identified and that are, consequently, classified as 0μ by the electronic detectors. The selection criteria defined for 0μ events are therefore applied. The muon identification, amounting to 97% after the application of the track follow-down, suppresses the background.
The background in this channels is mainly due to the decay of charged charmed particles D^+, D_S^+ and Λ_C^+ in the (e, h, μ) channels. The background coming from the $C^+ \to \mu^+$ decay channel is negligible given the daughter muon identification from electronic detectors which provides a further reduction of a factor 10.
Since the muon at primary vertex is not identified, the decay of τ and charm in either one or three hadronic prongs share similar behavior. The most discriminant kinematical variable between these two categories is the ϕ_{mod} angle, (see Section 2.11.1). In the charm case, the not-identified primary muon track is often the particle with largest angle with respect to the charm in the neutrino transverse plane. If this track is not identified as hadron, it is excluded from the hadron jet for the ϕ_{mod} evaluation. In the signal case, instead, the track farest to the τ in the neutrino transverse plane is often identified as hadron (see Section 2.12) and then not discarded from the hadron jet. The ϕ_{mod} angle distribution for the τ signal and charm background in either $1h$ and $3h$ decay channels are reported in Figure 59. The cut at $\phi_{mod} > 90°$ selects 81% of the signal and 37% of the charm background.

The overall location efficiencies for charm decays with one or three hadrons in the final state are:

$$\begin{aligned} \epsilon_{C\to h}^{TOT} &= (7.3 \pm 0.1) \times 10^{-4} \\ \epsilon_{C\to 3h}^{TOT} &= (12.5 \pm 0.1) \times 10^{-4} \end{aligned} \tag{27}$$

The background in the $\tau \to \mu$ is made up by charm events decaying in only one muon. The charm background in this channel is largely suppressed by the following additional requirements:

μ-matching Only one muon track is reconstructed by the electronic detectors and it is in agreement within 60 mrad with the slopes of the decay daughter.

μ-charge The daughter track is measured with a negative charge. The τ daughter has always negative charge. On the contrary, charged charmed particles have a positive charge, so their one-prong decay products have positive charge as well.

The efficiency of the selection for this channel is

$$\epsilon_{C\to\mu}^{TOT} = (7.3 \pm 0.1) \times 10^{-4}. \tag{28}$$

Overall charm background

The number of expected background charm events in the $\tau \to i (i = h, 3h, e)$ decay channel is

$$N_{exp}^{C\to i(0\mu)} = f_{C^+} Br(C \to i) \beta_0 N_{obs}^{0\mu} \langle \epsilon_{C\to i} \rangle \langle \frac{\sigma_{charm}}{\sigma_{\nu_\mu CC}} \rangle \tag{29}$$

The number of expected background charm events in the $\tau \to \mu$ decay channel is

$$N_{exp}^{C\to\mu(1\mu)} = f_{C^+} Br(C \to \mu) \beta_1 N_{obs}^{1\mu} \langle \epsilon_{C\to\mu} \rangle \langle \frac{\sigma_{charm}}{\sigma_{\nu_\mu CC}} \rangle \tag{30}$$

where f_{C^+} is the fraction of charged charms, amounting to 56% and $Br(C \to i)$ are the charged charm branching ratios in the different decay topologies (Table 24).
The background in the $C \to \mu$ decay channel is suppressed by the small branching ratio of charm in a single muon.

4.2.2 Hadron re-interactions

The second source of background to the hadronic decay channels is due to re-interactions in the lead of hadrons produced in ν_μNC and

	DECAY MODE	Br (%)
$C^+ \to 1$-prong	$C^+ \to \mu^+$	5.3 ± 2.7
$(65 \pm 6)\%$	$C^+ \to e^+$	5.1 ± 2.6
	$C^+ \to h^+$	53.5 ± 9.2
$C^+ \to 3$-prong	$C^+ \to \mu^+ + 2h$	2.2 ± 1.8
$(35 \pm 6)\%$	$C^+ \to e^+ + 2h$	2.0 ± 1.8
	$C^+ \to 3h$	30.8 ± 5.4

Table 24: Branching ratios of charged charmed particles in leptonic and hadronic decay modes.

ν_μCC interactions where the primary muon is not identified.
The dominant background from hadron re-interactions has been evaluated with a FLUKA based Monte Carlo code [79]. About 3×10^6 events were simulated where $1 \div 15$ GeV π^- are impinging on 1 mm of lead. The probability for a background interaction to occur over 2 mm of lead downstream and to satisfy the τ selection criteria is 6.3×10^{-5} per 0μ located event in $\tau \to h$ decay channel and 1.3×10^{-5} per 0μ located event in $\tau \to 3h$ decay channel.
OPERA-like bricks exposed to 2, 4 and 10 GeV/c π^- beams have been analyzed to validate the description of hadronic interactions by FLUKA simulation. A total hadronic track length of 59.6 m has been analyzed, corresponding to 318 interactions in the brick, out of which 88 are single-prong and 46 are three-prongs.
A good agreement is found between experimental and simulated data both in normalization and shape. Figure 60 shows the hadronic interaction length for different π^- energies, while in Figure 61 the number of produced tracks at the interaction vertex and the kink angle of single-prongs interactions are reported.
The hadron interactions background can be further reduced by increasing the detection efficiency of highly ionizing particles, low energy protons and nuclear fragments, emitted in the cascade of intra-nuclear interactions initiated by the primary particles and in the nuclear evaporation process. In order to detect a significant fraction of nuclear fragments emitted at large angle, an image analysis tool was developed. High resolution microscope tomographic images in 24 layers of 2.5 mm $\times$ 2.1 mm size are analyzed in the upstream and downstream films of an interaction vertex, with an angular acceptance up to $\tan(\theta) = 3$. This technique was applied to all the hadronic interactions reconstructed in the test beam bricks. In 2 GeV (4 GeV, 10 GeV) π^-exposure, at least one highly ionising particle was associated to

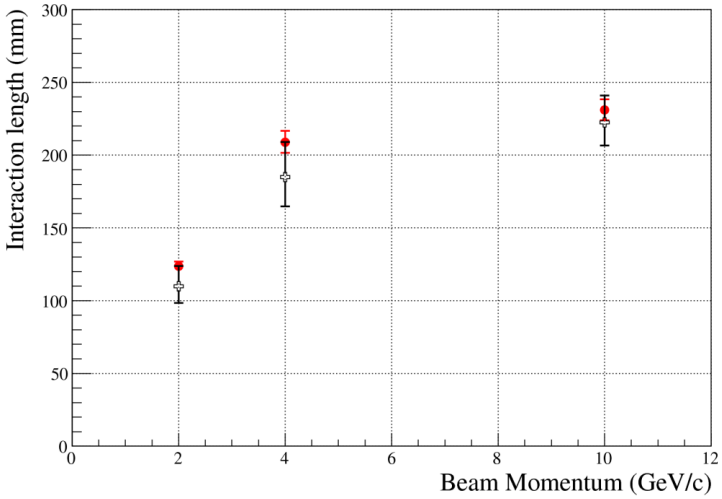

Figure 60: Hadronic interaction length as a function of the beam energy for experimental data (white crosses) and simulated data (red dots).

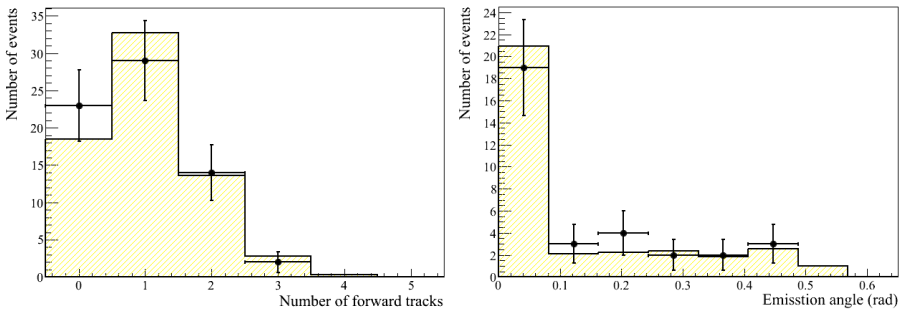

(a) Number of forward tracks **(b)** Kink angle in 1-prong interactions

Figure 61: Topological variables of the tracks emitted in 4 GeV/c (a) and 2 GeV/c (b) π^- interactions in an OPERA-like brick for experimental data (dots with error bars) and simulated data (histogram).

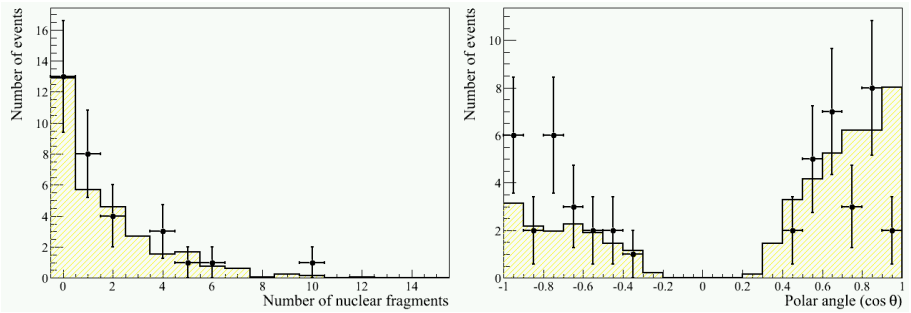

(a) Number of fragments

(b) Distribution of the cosine of the polar angle. Forward tracks correspond to $\cos\theta = 1$.

Figure 62: Topological variables of highly ionising particles emitted in 4 GeV/c π^- interactions in an OPERA-like brick for experimental data (dots with error bars) and simulated data (histogram).

$31.3^{+9.1}_{-6.9}\%$ ($58.1^{+8.1}_{-9.1}\%$, $63.6^{+5.0}_{-5.7}\%$) of the events while $23.4^{+1.5}_{-1.3}\%$ ($58.4^{+2.5}_{-2.5}\%$, $64.3^{+2.2}_{-2.3}\%$) are expected from simulations. Figure 62 shows a good agreement between experimental and simulated data in number of detected fragments and in the polar angle distribution of the highly ionising particles.
The technique allows detecting more highly ionising particles associated to secondary vertices, providing an additional background reduction of about 40%. No such particles were found to be associated to the decay vertex of all the three ν_τ candidate events.
Assuming decay search efficiencies similar to those of the τ, the probability for an hadronic interaction be detected as background is 1.6×10^{-5} per 0μ located event in $\tau \to h$ decay channel and 0.3×10^{-5} per 0μ located event in $\tau \to 3h$ decay channel.

4.2.3 Muon scattering

Muons produced in ν_μCC events and undergoing a large angle scattering in the two lead/emulsion plates following the vertex plate could mimic a muonic τ decay.
The evaluation of the corresponding background have been performed with a FLUKA based Monte Carlo simulation.
The probability for a muon scattering to occur over 2 mm of lead and to satisfy the selection criteria for the reconstruction of the $\tau \to \mu$ decay topology and its kinematics is 1.5×10^{-6} per CC event. The probability to have a scattering in the emulsion or in the plastic base, given the lower density and smaller thickness, is 2.5×10^{-8} per CC event.

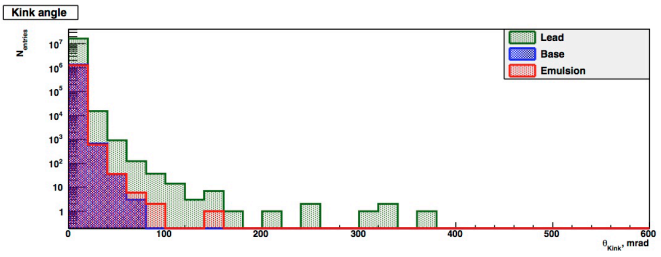

(a) Kink angle

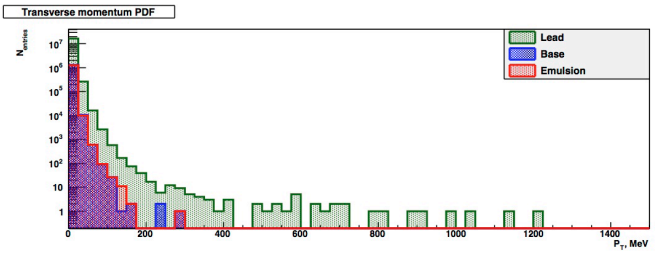

(b) Transverse momentum

Figure 63: Monte Carlo distribution of kinematical variables for muon scattering in lead (green), plastic base (blu) and emulsion (red).

A test beam exposure has been planned in order to confirm the above results.
With a conservative approach, we will use, as the background from muon scattering, the upper limit of 10^{-5} per located 1μ event reported in [80].
An additional reduction of 40% has been considered in order to take into account the decay search inefficiencies.

4.2.4 Background expectation

All the background sources in the different τ decay channels are summarized in Table 25. For the data sample analyzed so far, a total number of 0.23 events is expected. The background in the 1μ sample has been evaluated assuming that all the first brick have been analysed.
The background expectation becomes 0.35 if we consider the total collected beam intensity of 17.97×10^{19} p.o.t..

4.3 STATISTICAL SIGNIFICANCE

Given the background expectation in the different channels, it is possible to evaluate the significance of the observation by a *counting-olny* analysis.

	BACKGROUND EXPECTED EVENTS			
	Charm	Hadron	Muon	Total
$\tau \to h$	0.029	0.016	-	0.045
$\tau \to 3h$	0.087	0.003	-	0.090
$\tau \to \mu$	0.0084	-	0.018	0.026
$\tau \to e$	0.065	-	-	0.065
TOTAL	0.19	0.019	0.018	0.226

Table 25: Expected numbers of background events from different sources and for the different decay channels, for the data sample analyzed so far.

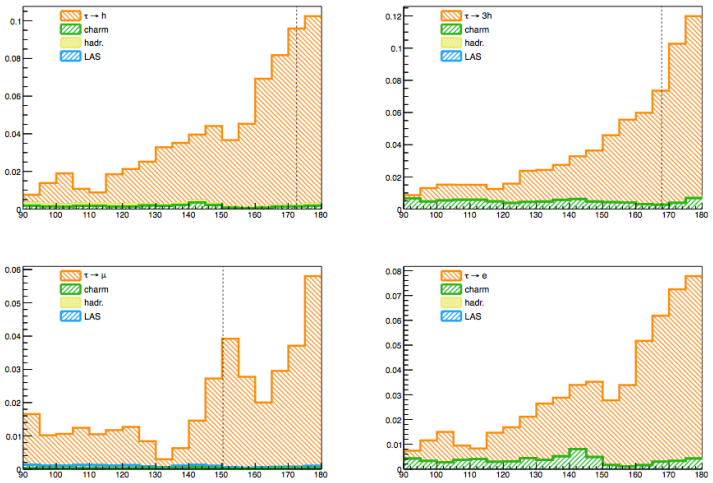

Figure 64: Signal and background PDFs for ϕ_{mod} in the different τ decay channels. Black lines represent the values assumed for these variables by the candidates.

The probability for the three events not to be due to a background fluctuations and thus the statistical significance is 3.2σ.
The statistical significance of the observation has also been evaluated by likelihood ratio method [8].
A probability density function (PDF) has been created, based on the ϕ_{mod} variable, the z coordinate of the decay point (Δz) and the vectorial sum of transverse momenta of secondary tracks with respect to the parent direction (p_T) for signal (f_S) and background (f_B). By definition PDFs are unit-normalized. They are shown in Figures 64, 65 and 66.
If s is the expected number of signal events and b the expected number of background events, a global PDF($f_{S+B}(s,b)$) is built by combining

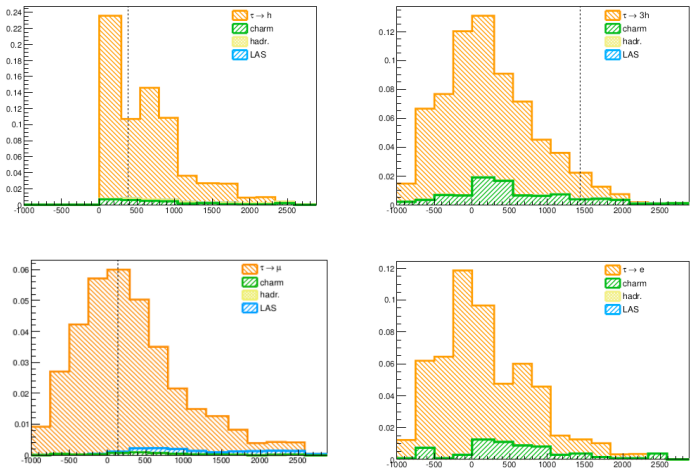

Figure 65: Signal and background PDFs for Δz in the different τ decay channels. Black lines represent the values assumed for these variables by the candidates.

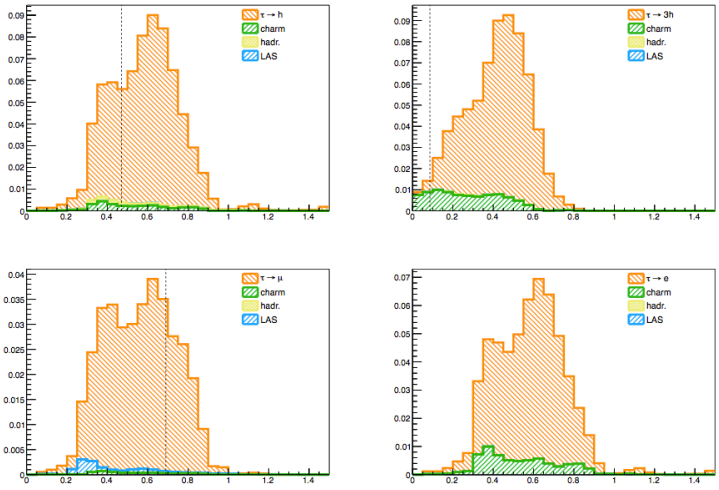

Figure 66: Signal and background PDFs for p_T in the different τ decay channels. Black lines represent the values assumed for these variables by the candidates.

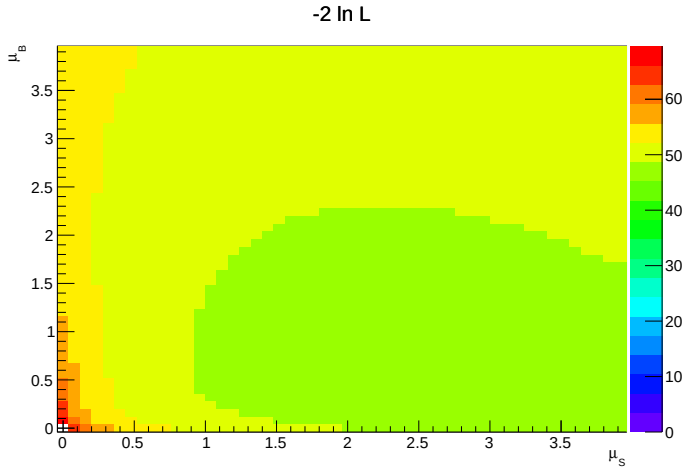

Figure 67: The (s, b) space is sampled and the three events are evaluated on the corresponding PDF.

the signal and background PDFs, f_S and f_B, with the coefficients s and b in the following way:

$$f^{S+B}(s, b, x) = \frac{s f_S(x) + b f_B(x)}{s + b} \tag{31}$$

such that they are always unit normalised.
The likelihood function is defined as

$$\mathcal{L}(s, b) = \frac{(s+b)^n e^{-(s+b)}}{n!} \prod_{c=1}^{4} \prod_{i=0}^{n_c} \prod_{\nu=1}^{n_\nu} f_{\nu,c}^{S+B}(s, b, x_\nu) \tag{32}$$

n is the total number of candidates, n_c is the number of candidates for channel c and ν denotes a variable. 1-dimensional PDFs are multiplied, thus neglecting possible correlations.
The resulting quantity $-2 \ln \mathcal{L}(s, b)$ is shown in Figure 67 as a function of s and b. The minimum is observed at $s = 2.4$, $b = 0.6$ and amounts to 47.1. The minimum of $-2 \ln \mathcal{L}(s, b)$ evaluated for $s = 0$ (null hypothesis) occurs at $b = 3$ and amounts to 53.9.
The likelihood ratio (LR) is defined

$$LR = -2 \ln \frac{\mathcal{L}(0, b)}{\mathcal{L}(s, b)} \tag{33}$$

$$LR = -2 \ln \mathcal{L}(0, b) + 2 \ln \mathcal{L}(s, b) \tag{34}$$

$$LR = \chi^2(0, b) - \chi^2(s, b) = \Delta\chi^2 \tag{35}$$

The observed value is

$$LR_{obs} = 6.8. \tag{36}$$

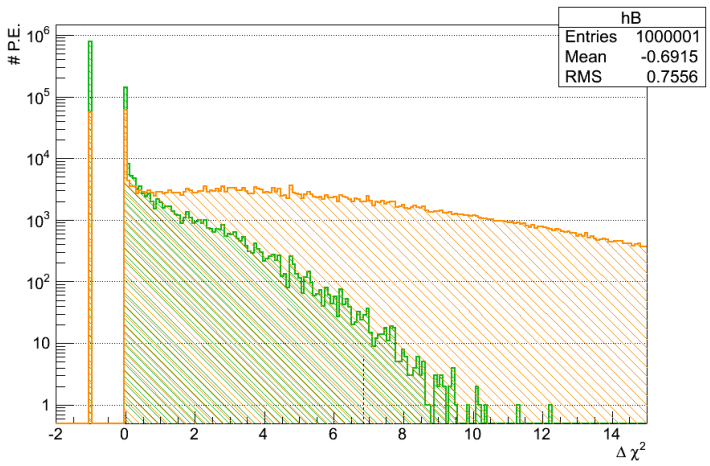

Figure 68: Distribution of LR for background pseudo-experiments sample.

To assess the significance of this test variable pseudo-experiments have been generated, sampling background-like events from the input Monte Carlo PDFs. The number of cases where a LR larger than the one observed in the data has been evaluated.
The distribution of LR for background pseudo-experiments is shown in Figure 68.
On 10^6 pseudo experiments 262 have a LR above the observed one corresponding to a p–value of 2.62×10^{-4} which corresponds to 3.5 one-sided σ for the exclusion of the null hypothesis.

CONCLUSIONS

The OPERA experiment searches for $\nu_\mu \rightarrow \nu_\tau$ oscillations in appearance mode. The detector consists of almost 150000 unit cells, called *bricks*, arranged in walls and interspaced with electronic detectors, for a total mass of about 1.25 kton. The Emulsion Cloud Chamber technique uses lead as neutrino target and emulsion films as high precision trackers, capable of observing the τ decay with a space granularity better than 1 μm. The electronic detectors provide the time stamp of neutrino interactions, identifying the brick where the interaction took place and measuring the muon charge and momentum.
In five years of run, from 2008 to 2012, the CNGS beam has provided a neutrino flux equivalent to 18×10^{19} protons on target and the OPERA experiment has collected more than 15000 neutrino interactions.
The analysis chain of neutrino interactions in the OPERA target has been fully simulated and the efficiencies for all the τ decay channels obtained. The kinematical selection of the events in the different decay channels has been studied and new variables have been defined in order to enhance the τ signal.
The comparison between data and Monte Carlo shows a good agreement, thus validating the simulation used to describe the event analysis.
A detailed analysis of all the background sources has been performed. In particular, the background from charmed hadron production and decay has been studied. Charmed hadrons produced in ν_μ CC interactions have masses and lifetimes similar to those of the τ. They can therefore mimic ν_τ interactions if the primary muon is not identified. In order to reduce this source of background the kinematical selection has been improved and a technique aiming at the reduction of the muon mis-identification has been developed.
The search for ν_τ interactions in the statistics so far analysed lead to the observation of three candidates, compatible with the expectation of 2.23 signal events. The three candidates come from the 2009, 2011 and 2012 runs and show different decay modes: $\tau \rightarrow h$, $\tau \rightarrow 3h$ and $\tau \rightarrow \mu$, respectively. They have been fully analysed and the results of the topological reconstruction as well as the kinematical analysis have been reported.
The statistical significance of the observation of three candidates has been evaluated with a simple counting method based on the background yield in the different channels. The result gives a significance

of 3.2σ. A method based on the likelihood ratio was also attempted. This analysis provides a significance of 3.5σ.

BIBLIOGRAPHY

[1] Wolfgang Pauli, *Open letter to radioactive ladies and gentlemen* (1930). Physics Today, 31:27, 1978.

[2] Maurice Goldhaber, L. Grodzins, and A.W. Sunyar, *Helicity of neutrinos*. Physical Review, 109 (1958) 1015-1017.

[3] Enrico Fermi, Zeitschrift fur Physik, 88 (1934) 161.

[4] S. L. Glashow, Nucl. Phys., 22 (1961) 579.

[5] S. Weinberg, Phys. Rev. Lett. 19 (1967) 1264.

[6] A. Salam, *Proceedings of the 8th Nobel Symposium on Elementary particle theory, relativistic groups and analyticity*, (1968), ed. Swartholm, Almquist and Wiksells, p.367-377.

[7] C. Rubbia, *Experimental Observation Of The Intermediate Vector Bosons* W^+, W^-, *And* Z^0, Rev. Mod. Phys. **57** (1985) 699.

[8] C. L. Cowan Jr., F. Reines, F.B. Harrison, H.W. Kruse, and A. D. McGuire. *Detection of the free neutrino: A confirmation*. Science, 124 (1956) 103-104.

[9] R. Davis Jr., D. H. S., and K. Hoffman C., *Search for neutrinos from the sun*, Phys. Rev. Lett. 20 (1968) 1205-1209.

[10] Y. Fukuda et al., *Measurement of a small atmoshperic* ν_μ/ν_e *ratio*. Phys. Lett. B 433 (1998) 9-18.

[11] Borexino Collaboration, *Observation of geoneutrinos*, Phys. Lett. B 687 (2010) 299-304.

[12] M.H. Ahn et al., *Measurement of neutrino oscillation by the k2k experiment*, Phys. Rev. D 74 (2006) 072003.

[13] K. S. Hirata et al., *Observation in the kamiokande-ii detector of the neutrino burst from supernova sn1987a*, Phys. Rev. D 38(2) (1988) 448-458.

[14] G. Danby et al., *Observation of high-energy neutrino reactions and the existence of two kinds of neutrinos*, Phys. Rev. Lett. 9 (1962) 36-44.

[15] Thomas Patzak for the DONUT Collaboration, *First direct observation of the tau neutrino*, Europhysics news 32(2) (2001) 56-57.

[16] ALEPH Collaboration, *Determination of the number of light neutrino species*, Phys. Lett. B 231 (1989) 519-529.

[17] C. Kraus et al., *Final results from phase II of the Mainz neutrino mass search in tritium beta decay*, Eur. Phys. J. C40 (2005) 447-468.

[18] K. Assamagan et al., *Upper limit of the muon-neutrino mass and charged-pion mass from momentum analysis of a surface muon beam*, Phys. Rev. D 53 (1996) 6065-6077.

[19] ALEPH Collaboration, R. Barate et al., *An Upper limit on the tau-neutrino mass from three-prong and five-prong tau decays*, Eur. Phys. J. C2 (1998) 395-406.

[20] S. Hannestad, A. Mirizzi, G. G. Raelt, and Y. Y. Wong, *Neutrino and axion hot dark matter bounds after WMAP-7* JCAP 1008 (2010) 001.

[21] S.N. Ahmed et al., *Measurement of the total active ^8B solar neutrino Flux at the Sudbury Neutrino Observatory with enhanced neutral current sensitivity*, Phys. Rev. Lett. 92 (2004) 181301.

[22] Y. Ashie et al. *A measurement of atmospheric neutrino oscillation parameters by Super-Kamiokande i*, Phys. Rev. D 71 (2005) 112005.

[23] K. Abe et al., *Indication of electron neutrino appearance from an accelerator-produced off-axis muon neutrino beam*, Phys. Rev. Lett. 107 (2011) 041801.

[24] S. Abe et al. *Precision measurement of neutrino oscillation parameters*, Phys. Rev. Lett. 100 (2008) 221803.

[25] F.P. An et al., *Observation of electron-antineutrino disappearance at Daya Bay*, arXiv:1203.1669v2 [hep-ex].

[26] Kim Soo-Bong et al., *Observation of reactor electron antineutrino disappearance in the Reno experiment*. arXiv:1204.0626v2 [hep-ex].

[27] G.L. Fogli, E. Lisi, A. Marrone, A. Palazzo, and A.M. Rotunno. *Evidence of $\theta_{13}>0$ from global neutrino data analysis*, arXiv:1106.6028v2[hep-ph].

[28] Jr. Davis, Raymond, Don S. Harmer, and Kenneth C. Hoffman, *Search for neutrinos from the sun*. Phys. Rev. Lett. 20 (1968) 1205-1209.

[29] J. N. Abdurashitov et al., *Measurement of the solar neutrino capture rate by the Russian-American gallium solar neutrino experiment during*

one half of the 22-year cycle of solar activity. J. Exp. Theor. Phys. 95 (2002) 181-193.

[30] W. Hampel et al., *GALLEX solar neutrino observations: Results for GALLEX IV*. Phys. Lett. B447 (1999) 127-133.

[31] Q. R. Ahmad et al., *Direct evidence for neutrino flavor transformation from neutral-current interactions in the Sudbury Neutrino Observatory*, Phys. Rev. Lett. 89 (2002) 011301.

[32] B. Aharmim et al., [SNO Collab.], Phys. Rev. C 72 (2005) 055502.

[33] B. Aharmim et al., [SNO Collab.], *Measurement of the $\overline{\nu_e}$ and total ^{8}B solar neutrino fluxes with the Sudbury Neutrino Observatory phase-III data set*, Phys. Rev. C 87 (2013) 015502.

[34] T. Araki et al. *Measurement of neutrino oscillation with KamLAND: Evidence of spectral distortion*. Phys. Rev. Lett. 94 (2005) 081801.

[35] S. Abe et al., *Precision measurement of neutrino oscillation parameters with Kamland*. Phys. Rev. Lett. 100 (2008) 221803.

[36] Y. Fukuda et al., *Evidence for oscillation of atmospheric neutrinos*, Phys. Rev. Lett. 81 (1988) 1562-1567.

[37] M. Ambrosio et al., [MACRO collaboration] Eur. Phys. J. C 36 (2004) 323.

[38] W.W.M. Allison et al.,[SOUDAN-2 collaboration] Phys. Rev. D 72 (2005) 052005.

[39] M. H. Ahn et al., *Measurement of Neutrino Oscillation by the K2K Experiment*, Phys. Rev. D 74 (2006) 072003.

[40] A. Habig., *MINOS neutrino oscillation results*, Nucl.Phys.Proc.Suppl., 218 (2011) 320-325.

[41] M. Apollonio et al. (CHOOZ Collaboration), *Search for neutrino oscillations on a long baseline at the CHOOZ nuclear power station*, Eur. Phys. J. C27 (2003) 331.

[42] Double-CHOOZ Collaboration, *Double Chooz, A Search for the Neutrino Mixing Angle theta-13*, 2006, ArXiv:hep-ex/0606025.

[43] Kim, Soo-Bong et al., [RENO Collaboration], *RENO for neutrino mixing angle Theta(13)*, Prog. Part. Nucl. Phys. 64 (2010) 346-347.

[44] Daya Bay Collaboration, *A Precision Measurement of the Neutrino Mixing Angle θ13 Using Reactor Antineutrinos at Daya Bay*, 2006, ArXiv:hep-ex/0701029.

[45] K. Abe et al., [T2K Collaboration], *The T2K Experiment*, Nucl. Instrum. Meth. A 659 (2011) 106-135.

[46] NOVA Collaboration, *The NOvA Experiment, A Long-Baseline Neutrino Experiment at the Intensity Frontier*, PoS HQL2012 (2012) 024.

[47] G. Mention et al., *A Unified analysis of the reactor neutrino program towards the measurement of the theta(13) mixing angle*, JPhys. Conf. Ser. 110 (2008) 082013.

[48] K. Abe et al. (T2K Collaboration), *Indication of Electron Neutrino Appearance from an Accelerator-Produced Off-Axis Muon Neutrino Beam*, Phys. Rev. Lett. 107 (2011) 041801.

[49] P. Adamson et al., [MINOS Collaboration], *Measurements of atmospheric neutrinos and antineutrinos in the MINOS Far Detector*, Phys.Rev. D 86 (2012) 052007.

[50] P. Adamson et al. *Improved search for muon-neutrino to electron-neutrino oscillations in MINOS*, Phys. Rev. Lett. 107 (2011) 181802.

[51] Y. Abe et al. *Indication for the disappearance of reactor electron antineutrinos in the Double Chooz experiment*, Phys. Rev. Lett. 108 (2012) 131801.

[52] F.P. An et al. *Observation of electron-antineutrino disappearance at Daya Bay*, Phys. Rev. Lett. 108 (2012) 171803.

[53] J.K. Ahn et al. *Observation of Reactor Electron Antineutrino Disappearance in the RENO Experiment*, Phys. Rev. Lett. 108 (2012) 191802.

[54] G.L. Fogli et al., *Global analysis of neutrino masses, mixings and phases: entering the era of leptonic CP violation searches*, Phys. Rev. D 86 (2012) 013012.

[55] OPERA Collaboration, M. Guler et al., *An appearance experiment to search for $\nu_\mu \to \nu_\tau$ oscillation in the CNGS beam: experimental proposal*, CERNSPSC- 97-24, LNGS-LOI-8-97.

[56] OPERA Collaboration, M. Guler et al., *Status report of the OPERA experiment*, CERN/SPSC 2001-025, LNGS-EXP 30/2001 add. 1/01.

[57] OPERA Collaboration, R. Acquafredda et al., *The OPERA experiment in the CERN to Gran Sasso neutrino beam*, JINST 4 (2009) P04018.

[58] OPERA Collaboration, R. Acquafredda et al., *First events from the CNGS neutrino beam detected in the OPERA experiment*, New J. Phys. 8 (2006) 303.

[59] CNGS project: http://proj-cngs.web.cern.ch/proj-cngs/;
K. Elsner (Ed.), *The CERN Neutrino beam to Gran Sasso* (Conceptual Technical Design), CERN 98-02, INFN/AE-98/05;
R. Bailey et al., *The CERN Neutrino beam to Gran Sasso (CNGS)* (Addendum to report CERN 98-02, INFN/AE-98/05), CERN-SL/99-034(DI), INFN/AE-99/05.

[60] L. Arrabito et al., *Track reconstruction in the emulsion-lead target of the OPERA experiment using the ESS microscope*, JINST 2 (2007) P05004.

[61] M. De Serio et al., *Momentum measurement by the angular method in the Emulsion Cloud Chamber*, Nucl. Instr. Meth. A512 (2003) 539-545.

[62] L. Arrabito et al., *Electron/pion separation with an Emulsion Cloud Chamber by using a Neural Network*, JINST 2 (2007), P02001.

[63] A. Anokhina et al. [OPERA Collaboration], *Study of the effects induced by lead on the emulsion films of the OPERA experiment*, JINST 3 (2008), P07002.

[64] A. Anokhina et al. [OPERA Collaboration], *Emulsion sheet doublets as interface trackers forthe OPERA experiment*, JINST 3 (2008) P07005.

[65] T. Adam et al., *The OPERA experiment Target Tracker*, Nucl. Instr. Meth. A577 (2007) 523.

[66] N. Agafonova et al., [OPERA Collaboration], *Study of neutrino interactions with the electronic detectors of the OPERA experiment*, New J. Phys. 13 (2011) 053051.

[67] M. Ambrosio et al., , IEEE Trans. Nucl. Sci. 51 (2004) 975.

[68] R. Zimmermann et al., , Nucl. Instrum. Meth. A 555 (2005) 435.

[69] A. Bergnoli et al., , Nuclear Physics B (Proc. Suppl.) (2006) 158,
A. Bergnoli et al., , IEEE Trans. Nucl. Sci. 52 (2005).

[70] K. Morishima and T. Nakano, *Development of a new automatic nuclear emulsion scanning system, S-UTS, with continuous 3D tomographic image read-out*, JINST 5 (2010) PP04011.

[71] N. Armenise et al., *High-speed particle tracking in nuclear emulsion by last generation automatic microscopes*, Nucl. Instrum. Meth. A 551 (2005) 261.

[72] L. Arrabito et al., *Hardware performance of a scanning system for high speed analysis of nuclear emulsions*, Nucl. Instrum. Meth. A 568 (2006) 578.

[73] L. Arrabito et al., *Track reconstruction in the emulsion-lead target of the OPERA experiment using the ESS microscope*, JINST 2 (2007) P05004.

[74] N. Agafonova et al. [OPERA Collaboration], *Study of neutrino interactions with the electronic detectors of the OPERA experiment*, New J. Phys. 13 (2011) 053051.

[75] A. Bertolin and N.T. Tran. *OpCarac: an algorithm for the classification of the neutrino interactions recorded by the OPERA experiment*. Technical report, OPERA note 100, 25/05/2009.

[76] N. Agafonova et al. [OPERA Collaboration], *Momentum measurement by the Multiple Coulomb Scattering method in the OPERA lead emulsion target*, New J. Phys. 14 (2012) 013026.

[77] A. Kayis-Topaksu et al, CHORUS Collaboration, *Measurement of charm production in neutrino charged-current interactions*, New J. Phys. 13 (2011) 093002.

[78] E. L. Berger at al, *The minimum invariant mass: a technique for heavy quark searches at collider energy*, Phys. Lett. B 140 (1984) 259.

[79] FLUKA, http://www.fluka.org/fluka.php;
G. Battistoni, et al. , *Proceedings of the Hadronic Shower Simulation Workshop 2006*, Fermilab 6-8 September 2006, M. Albrow, R. Raja eds., AIP Conference Proceeding 896 (2007) 31-49.

[80] S.A. Akimenko et al.,*Multiple coulomb scattering of 7.3 and 11.7 GeV/c muons on a Cu target* NIM A423 (1986) 518. [8] G. Cowan et al., Eur. Phys. J. C71 (2011) 1554.